To the Graduate Council:

I am submitting herewith a dissertation written by Johnny Page Forester entitled "An Investigation of Radiative Lifetimes and Oscillator Strengths for Allowed Intra L-Shell Transitions in Multiply-Charged Chlorine Ions." I recommend that it be accepted in partial fulfillment of the requirements for the degree of Doctor of Philosophy, with a major in Physics.

David J. Pegg

David J. Pegg, Major Professor

We have read this dissertation
and recommend its acceptance:

J. A. Seiler

F. J. Rieding

G. D. O'Kelley

Wm M Bugg

Accepted for the Council:

L Evans Roth

Vice Chancellor
Graduate Studies and Research

Thesis
786
.F674
cop. 2

AN INVESTIGATION OF RADIATIVE LIFETIMES AND OSCILLATOR STRENGTHS FOR ALLOWED INTRA L-SHELL TRANSITIONS IN MULTIPLY-CHARGED CHLORINE IONS

A Dissertation

Presented for the

Doctor of Philosophy

Degree

The University of Tennessee, Knoxville

Johnny Page Forester

March 1978

1356905

DEDICATION

This dissertation is dedicated to my wife Anita and my two sons Johnny and Matthew. Had it not been for their patience and support this work would not have been completed. Had it not been for them it would not have been worthwhile.

ACKNOWLEDGEMENTS

The author is grateful to all of the members of the University of Tennessee - Oak Ridge National Laboratory atomic physics group that aided in the accumulation of the data presented herein. Their names in alphabetical order are: G. D. Alton, S. B. Elston, P. M. Griffin, H. C. Hayden, D. J. Pegg, S. Schumann, I. A. Sellin, M. Sutter, R. S. Thoe, C. R. Vane, and J. J. Wright.

Appreciation is especially expressed to Paul M. Griffin for his invaluable instruction in the principles and operation of the spectrometer as well as for the many hours he spent in helping to calibrate the apparatus. A great deal of appreciation is also expressed to David J. Pegg for his leadership throughout the project. His guidance in analyzing the data was extremely beneficial and his expertise in technical writing served to vastly improve the quality of this dissertation.

ABSTRACT

The beam-foil time-of-flight method has been used to investigate radiative lifetimes and transition rates involving $\Delta n=0$ electric-dipole transitions within the L-shell of multiply charged chlorine (Cl IX - Cl XV). The high energy beam ions produced by the Oak Ridge National Laboratory tandem accelerator were directed through $5\ \mu g/cm^2$ carbon excitor foils. The foil-excited EUV beam radiation was dispersed and detected with a 2.2 m grazing incidence spectrometer. Lifetimes have been converted to oscillator strengths (f-values) for transitions for which there exists only one channel of deexcitation. F-values and lifetimes were compared with recent theoretical predictions in tables and by making f versus Z^{-1} plots for individual transitions. Spectral scans were made with ion beam energies of 38 and 18 MeV. Three previously unreported lines falling at 215.5 Å, 271.2 Å, and 331.9 Å appear to be associated with the $(1s^2 2s2p^5)\,^1P_1^o - (1s^2 2p^6)\,^1S_0$ transition in Cl X and the $(1s^2 2s2p^3)\,^1D_2^o - (1s^2 2p^4)\,^1D_2$ and $(1s^2 2s2p^3)\,^1P_1^o - (1s^2 2p^4)\,^1D_2$ transition in Cl XII.

TABLE OF CONTENTS

CHAPTER		PAGE
1.	INTRODUCTION	1
2.	THEORY	6
3.	EXPERIMENTAL METHOD	12
4.	RESULTS	36
	Spectra	36
	Lifetimes	51
5.	DISCUSSION OF RESULTS	99
LIST OF REFERENCES		129
APPENDIX		131
VITA		135

LIST OF TABLES

TABLE		PAGE
3.1.	Typical Values of Some Parameters Encountered in this Experiment	18
3.2.	Parameters of the Spectrometer Necessary to Calculate the Window	31
4.1.	Spectrum of Foil-Excited Cl Ions at 38 MeV Incident Beam Energy	37
4.2.	Spectrum of Foil-Excited Cl Ions at 18 MeV Incident Beam Energy	46
4.3.	Ion Beam Parameters Encountered	52
4.4.	Lifetimes of Low-Lying Excited States in Multiply-Charged Chlorine Ions	54
5.1.	Transition Rates and f-values for $\Delta n=0$ Transitions within the L-shell of Multiply-Charged Chlorine Ions	100

LIST OF FIGURES

FIGURE		PAGE
3.1.	Schematic of apparatus used in the present study.	13
3.2.	Equilibrium charge state distributions of chlorine ions emerging from a carbon foil.	14
3.3.	Schematic of grazing incidence spectrometer	23
3.4.	Some hollow cathode source lines used to wavelength-calibrate the grazing incidence spectrometer.	26
3.5.	Schematic of electronic arrangement used in the present experiment.	27
3.6.	Schematic showing the relationship of the beam axis, the entrance slit and grating mask system of the monochromator	30
3.7.	Intensity decay curve for a short-lived transition.	33
4.1.	Spectrum of foil-excited chlorine ions ($195 \leq \lambda \leq 220$ Å) taken at an incident beam energy of 38 MeV.	43
4.2.	Spectrum of foil-excited chlorine ions ($220 \leq \lambda \leq 280$ Å) taken at an incident beam energy of 38 MeV.	44
4.3.	Spectrum of foil-excited chlorine ions ($285 \leq \lambda \leq 305$ Å) taken at an incident beam energy of 38 MeV.	45
4.4.	Spectrum of foil-excited chlorine ions ($160 \leq \lambda \leq 210$ Å) taken at an incident beam energy of 18 MeV.	49
4.5.	Partial energy level diagram of Li-like chlorine for $\Delta n=0$ transitions within the L-shell	59
4.6.	Intensity decay curve for the $(2s)^2S_{1/2} - (2p)^2P^o_{3/2}$ transition in Cl XV taken with an incident beam energy of 45.5 MeV.	60
4.7.	Intensity decay curve for the $(2s)^2S_{1/2} - (2p)^2P^o_{1/2}$ transition in Cl XV taken with an incident beam energy of 45.5 MeV.	61
4.8.	Partial energy level diagram for Cl XIV showing allowed $\Delta n=0$ transitions within the L-shell.	63

FIGURE PAGE

4.9. Intensity decay curve for the $(2s2p)^1P^o_1 - (2p^2)^1D_2$ transition in Cl XIV taken with an incident beam energy of 45.5 MeV. 64

4.10. Intensity decay curve for the $(2s^2)^1S_0 - (2s2p)^1P^o_1$ transition in Cl XIV taken with an incident beam energy of 45.5 MeV. 66

4.11. Intensity decay curve for the $(2s2p)^3P^o_2 - (2p^2)^3P_2$ transition in Cl XIV taken with an incident beam energy of 45.5 MeV. 67

4.12. Partial energy level diagram of Cl XIII showing $\Delta n=0$ transitions within the L-shell of doublet and quartet systems 69

4.13. Intensity decay curve for the $(2s2p^2)^2D_{5/2,3/2} - (2p^3)^2P_{3/2}$ transition in Cl XIII taken with an incident beam energy of 38 MeV 70

4.14. Intensity decay curve for the $(2s^22p)^2P^o_{1/2} - (2s2p^2)^2D_{3/2}$ transition in Cl XIII taken with an incident beam energy of 38 MeV 73

4.15. Partial energy level diagram of the triplet system of Cl XII showing $\Delta n=0$ transitions within the L-shell 75

4.16. Partial energy level diagram of the singlet system of Cl XII showing $\Delta n=0$ transitions within the L-shell 76

4.17. Intensity decay curve for the $(2s^22p^2)^3P_1 - (2s2p^3)^3P^o_{1,0}$ transition in Cl XII taken with an incident beam energy of 38 MeV 79

4.18. Intensity decay curve for the $(2s^22p^2)^3P_1 - (2s2p^3)^3D^o_{2,1}$ transition in Cl XII taken with an incident beam energy of 38 MeV 80

4.19. Intensity decay curve for the $(2s^22p^2)^1D_2 - (2s2p^3)^1D^o_2$ transition in Cl XII taken with an incident beam energy of 38 MeV 83

4.20. Partial energy level diagram of Cl XI showing $\Delta n=0$ transitions within the L-shell of doublet and quartet systems 84

FIGURE PAGE

4.21. Intensity decay curve for the $(2s2p^4)^2D_{5/2} - (2p^5)^2P^o_{3/2}$ transition in Cl XI taken with an incident beam energy of 18 MeV 86

4.22. Intensity decay curve for the $(2s^22p^3)^3P^o_{3/2} - (2s2p^4)^2S_{1/2}$ transition in Cl XI taken with an incident beam energy of 18 MeV 88

4.23. Intensity decay curve for the $(2s^22p^3)^2D^o_{5/2,3/2} - (2s2p^4)^2D_{5/2,3/2}$ transition in Cl XI taken with an incident beam energy of 18 MeV 90

4.24. Partial energy level diagram of Cl X showing $\Delta n=0$ transitions within the L-shell. 92

4.25. Intensity decay curve for the $(2s2p^5)^1P^o_1 - (2p^6)^1S_0$ transition in Cl X taken with an incident beam energy of 18 MeV. 93

4.26. Intensity decay curve for the $(2s^22p^4)^3P_{2,1} - (2s2p^5)^3P^o_{2,1}$ transition in Cl X taken with an incident beam energy of 18 MeV. 95

4.27. Partial energy level diagram of Cl IX showing $\Delta n=0$ transitions in the L-shell. 96

4.28. Intensity decay curve for the $(2s^22p^5)^2P^o_{3/2} - (2s2p^6)^2S_{1/2}$ transition in Cl IX taken with an incident beam energy of 8 MeV 97

5.1. Isoelectronic sequence plot showing the multiplet f-value of the $(2s)^2S - (2p)^2P^o$ transition versus inverse nuclear charge. 105

5.2. Isoelectronic sequence plot showing the line f-values of the Li-like transitions as measured in the present work . . 106

5.3. Isoelectronic sequence plot showing the multiplet f-value of the $(2s^2)^1S - (2s2p)^1P^o$ transition versus inverse nuclear charge. 107

5.4. Isoelectronic sequence plot showing the multiplet f-value of the $(2s2p)^1P^o - (2p^2)^1S$ transition versus inverse nuclear charge. 109

FIGURE PAGE

5.5. Isoelectronic sequence plot showing the multiplet f-value of the $(2s2p)^3P^o - (2p^2)^3P$ transition versus inverse nuclear charge. 110

5.6. Isoelectronic sequence plot showing the multiplet f-value of the $(2s2p)^1P^o - (2p^2)^1D$ transition versus inverse nuclear charge. 111

5.7. Isoelectronic sequence plot showing the multiplet f-value of the $(2s^22p)^2P^o - (2s2p^2)^2S$ transition versus inverse nuclear charge. 112

5.8. Isoelectronic sequence plot showing the multiplet f-value of the $(2s^22p)^2P^o - (2s2p^2)^2P$ transition versus inverse nuclear charge. 114

5.9. Isoelectronic sequence plot showing the multiplet f-value of the $(2s^22p)^2P^o - (2s2p^2)^2D$ transition versus inverse nuclear charge. 115

5.10. Isoelectronic sequence plot showing the multiplet f-value of the $(2s2p^2)^4P - (2p^3)^4S^o$ transition versus inverse nuclear charge. 116

5.11. Isoelectronic sequence plot showing the multiplet f-value of the $(2s^22p^2)^3P - (2s2p^3)^3S^o$ transition versus inverse nuclear charge. 118

5.12. Isoelectronic sequence plot showing the multiplet f-value of the $(2s^22p^2)^3P - (2s2p^3)^3P^o$ transition versus inverse nuclear charge. 119

5.13. Isoelectronic sequence plot showing the multiplet f-value of the $(2s^22p^2)^3P - (2s2p^3)^3D^o$ transition versus inverse nuclear charge. 120

5.14. Isoelectronic sequence plot showing the multiplet f-value of the $(2s^22p^2)^1D - (2s2p^3)^1D^o$ transition versus inverse nuclear charge. 122

5.15. Isoelectronic sequence plot showing the multiplet f-value of the $(2s^22p^3)^2P^o - (2s2p^4)^2S$ transition versus inverse nuclear charge. 123

FIGURE PAGE

5.16. Isoelectronic sequence plot showing the multiplet f-value of the $(2s^2 2p^3)\,^4S^o$ - $(2s2p^4)\,^4P$ transition versus inverse nuclear charge. 124

5.17. Isoelectronic sequence plot showing the multiplet f-value of the $(2s2p^5)\,^1P^o$ - $(2p^6)\,^1S$ transition versus inverse nuclear charge. 126

5.18. Isoelectronic sequence plot showing the multiplet f-value of the $(2s^2 2p^4)\,^3P$ - $(2s2p^5)\,^3P^o$ transition versus inverse nuclear charge. 127

5.19. Isoelectronic sequence plot showing the multiplet f-value of the $(2s^2 2p^5)\,^2P^o$ - $(2s2p^6)\,^2S$ transition versus inverse nuclear charge. 128

CHAPTER 1

INTRODUCTION

The beam-foil time-of-flight technique was used in the present work to study spectra and radiative lifetimes of excited electronic levels in multiply-charged chlorine ions with from three to nine bound electrons. The experimental method consists of passing a constant velocity ion beam through a thin carbon foil which serves to further strip and excite the ions. These foil-excited ions subsequently decay in flight emitting photons. A monochromator is used to disperse the radiation emitted by the foil-excited beam ions. The intensity of a wavelength-selected line is then studied as a function of the relative distance between the excitor foil and the viewing region of the spectrometer. The selected line "signatures" the decay of an excited state via a particular transition channel. Decay lengths obtained from such decay curves are converted to lifetimes by simply dividing by the constant post-foil beam velocity.

The beam-foil time-resolved spectroscopic technique began early in the 1960's and since that time it has proven to be a versatile tool in the investigation of dynamic properties of atoms and positive ions. The method involves a mating of two previously established branches of research, nuclear physics with its associated accelerator technology and pulse-handling systems and classical spectroscopy with its sophisticated wavelength-selecting equipment. It was fortunate for the beam-foil method that during the period of its early development the direction of nuclear research was turning toward more energetic heavy ion beams that were produced by more powerful accelerators. This freed some of the smaller machines for non-nuclear research such as beam-foil spectroscopy.

From the very beginning of quantitative spectroscopy in the mid-nineteenth century, new and better light sources have been sought. More recently spectroscopists have looked for sources, such as the beam-foil source, that have the ability to produce spectra of highly ionized species. As early as 1919 the use of an accelerated ion beam (excited in this case by a gas target) as a light source was reported[1] but the beam-foil technique was not itself established until 1963 when Kay, at the University of Manchester, published a paper[2] describing the accumulation of an emission spectrum of highly-stripped ions following the passage of a fast nitrogen ion beam through a thin solid medium (foil). Soon after this Bashkin and his collegues at the University of Arizona published the results[3] of experiments in which excited state lifetime measurements were performed using the new "beam-foil" technique (a simple time-of-flight process). It became clear that the beam-foil technique constituted a versatile method for measuring the lifetimes of excited states in varying degrees of ionization. No other method is presently available to perform accurate time-resolved decay studies on multiply-charged ions. Since these early days the beam-foil method has developed to encompass several other types of measurements besides the aforementioned spectroscopic and lifetime studies. For example, quantum interference effects

---

[1] W. Wein, Annals der Physik 60, 597 (1919)

[2] L. Kay, Physics Letters 5, 36 (1963).

[3] S. Bashkin, Nuclear Instruments and Methods 28, 88 (1964); S. Bashkin and A. B. Meinel, Astrophysical Journal 139, 413 (1964); S. Bashkin, L. Heroux, and J. Shaw, Physics Letters 13, 229 (1964).

("beats") have been observed in several systems and are used to study spectroscopically-unresolvable intervals such as those associated with fine and hyperfine interactions. Polarization measurements on emitted foil-excited radiation have also been made. Beam-foil experiments have not been restricted to the investigation of photon emission. In the early 1970's the University of Tennessee-Oak Ridge (UT-ORNL) group made the first spectroscopic studies of discrete energy electrons emitted subsequent to the radiationless mode of deexcitation called autoionization.[4] Presently the status of beam-foil lifetime work is somewhat analogous to that previously mentioned for nuclear research in the early 1960's. The investigation of decay properties of highly-stripped heavy ions necessitates the use of increasingly energetic ion beams and thus larger and more powerful accelerators (usually tandem Van de Graaff and linear accelerators). In the present investigation, chlorine has been multiply ionized by the passage of a beam of energy $\sim$1 MeV per nucleon through a thin carbon foil target. At these beam energies chlorine up to fourteen times ionized was produced in the post-foil source.

Current theoretical studies of the structure of many-electron systems frequently involve the treatment of electron correlation contributions and relativistic corrections to the simple non-relativistic independent particle model. This is particularly true for allowed (electric dipole) transitions which do not involve a change in principal quantum number i.e. $\Delta n = 0$ transitions. For such in-shell processes

---

[4] B. Donnally, W. W. Smith, D. J. Pegg, M. Brown and I. A. Sellin, Physical Review A4, 122 (1971).

correlation effects are important (especially for low Z systems) due to the interpenetrability of electrons with the same principal quantum number. Relativistic corrections become significant (especially for high Z systems) due to the fact that $\Delta n=0$ transition energies represent small differences between large binding energies. In the present work $\Delta n=0$ L-shell transitions of the general type $2s^2 2p^k - 2s2p^{k+1}$ and $2p^{k+1} - 2p^{k+2}$ have been studied for chlorine ions with from three to nine bound electrons i.e. Li-like to F-like chlorine. Electric dipole transition probabilities scale linearly with Z along an isoelectronic sequence for these in-shell processes whereas out-of-shell ($\Delta n\neq 0$) transition rates scale as Z^4. For a heavy element such as chlorine (Z=17) lifetimes of levels deexciting via $\Delta n\neq 0$ transitions are far too short to be measured by the beam-foil time-of-flight method. This is not the case however for the $\Delta n=0$ transitions studied in the present work where lifetime measurements were in the 10^{-11} to 10^{-9} sec range.

Experimentally determined transition rates or oscillator strengths (f-values) for radiative transitions are particularly sensitive indicators of the appropriateness of wavefunctions used as the descriptions of the initial and final states of a transition. In the present work transition probabilities and f-values were derived from the lifetime measurements for those levels for which there exists only one channel of deexcitation (i.e. unity branching ratio). These results are valuable in the establishment of systematic trends for a particular transition along an isoelectronic sequence. Once such trends are established it will be a simple matter to interpolate for ions of specific practical interest.

Experimentally determined f-values for highly-ionized heavy ions are particularly useful in the interpretation of spectral observations from high temperature astrophysical and laboratory plasma sources. For example, these line strength parameters have been used to gain information on physical conditions such as electron temperatures and densities in the solar atmosphere. A problem of high current interest is the role played by highly-stripped heavy ions which form low concentration impurities in controlled thermonuclear plasmas. Discrete line emissions from such impurity ions apparently contribute strongly to the unwanted cooling of the plasma.

Since emission spectra from hot plasma sources and the beam-foil source are somewhat similar it is tempting to derive an effective "temperature" for the latter source. Of course this is not a real temperature since there does not exist a Maxwellian velocity distribution for the unidirectional beam-foil source. However relative velocities between electrons and ions in both types of sources can be made comparable. Nagel[5] has suggested a simple reciprocity relationship in which the average electron velocity in a plasma is equated to the projectile ion beam velocity (neglecting both plasma ion motion and target electron motion). Using this approach for a chlorine ion beam of 45 MeV energy (the highest beam energy used in the present work) one obtains an effective beam-foil source "temperature" of 3.6×10^6 °K which is comparable to thermal conditions in hot plasma sources such as the solar corona.

---

[5]D. J. Nagel, "Beam-Foil Spectroscopy" (I. A. Sellin and D. J. Pegg, eds.), Vol II, p. 961. Plenum Press, New York, 1976.

CHAPTER 2

THEORY

One of the most fundamental quantities of atomic structure is the probability per unit time for a spontaneous electric dipole (E1) transition between two states involving the emission of a single photon (Einstein A-coefficient). This quantity is defined as:

$$A_{ij} = \frac{64\pi^4}{3hc^3} \nu_{ij}^3 |\langle j | \vec{D} | i \rangle|^2, \qquad (2\text{-}1)$$

where $|i\rangle$ and $|j\rangle$ are the initial and final states respectively, ν_{ij} is the frequency of the emitted radiation, and $\vec{D}$ is the electric-dipole operator. One method of measuring these rates involves a determination of the radiative lifetime (τ_i) of the upper state of the transition which is related to the sum of all the transition probabilities A_{if} for deexcitation by the equation:

$$\tau_i = \frac{1}{\sum_f A_{if}} \quad . \qquad (2\text{-}2)$$

The sum is over all the final states $|f\rangle$ allowed by the E1 selection rules. If the branching ratio for the $|i\rangle \rightarrow |j\rangle$ transition is unity (or is the dominant decay channel) then the sum in equation (2-2) reduces to a single term and the inverse of the lifetime produces the transition probability. This is the case for the principal resonance transitions studied in this experiment, i.e. those transitions between the first excited state and the ground state. If more than one deexcitation channel is possible, complementary information on relative branching (i.e. the branching ratio) is necessary to derive a particular A-value from a lifetime measurement.

It is however the absorption oscillator strengths (f-values) which are most frequently used in the comparison of experimental results and theory. For example, the f-value equation found most useful by theorists is given by:

$$f_{ji} = (2/3)\ (\Delta E/g_j)\ S\ , \qquad (2\text{-}3)$$

where ΔE is the transition energy (in atomic units), $|i\rangle$ and $|j\rangle$ are the initial and final states respectively, and g_j is the statistical weight of the lower state. The line strength S (in the length form) is defined by:

$$S = |\langle j\ |\ \vec{D}\ |\ i\rangle|^2\ , \qquad (2\text{-}4)$$

where again $|i\rangle$ and $|j\rangle$ are the initial and final states of the transition and $\vec{D}$ is the electric-dipole operator. In many cases the "best" approximate wavefunction used to obtain S is not the best choice for the calculation of ΔE. However, ΔE can be measured very accurately for most transitions by high-resolution spectroscopic techniques. When no higher resolution wavelength measurements are available, the beam-foil technique can be used to obtain the transition energy as well as the transition probability. If measured transition energies are used in the derivation of the f-value, the experiment can directly test the calculation of the line-strength factor. This quantity is particularly sensitive to the correctness of the wavefunctions employed in the calculations.

The f-value equation most convenient for use by experimentalists is:

$$f_{ji} = (1.4992 \times 10^{-16})\lambda_{ij}^2 (g_i/g_j)\ A_{ij}\ , \qquad (2\text{-}5)$$

where $|i\rangle$ and $|j\rangle$ are the upper and lower states of the transition

respectively, g_i and g_j are the statistical weights of the upper and lower states, λ_{ij} is the wavelength of the transition (in Å) and A_{ij} is the electric dipole transition probability (s^{-1}). Again for transitions with only one decay channel A_{ij} may be replaced with the measured quantity τ_i^{-1}.

A convenient method of graphically comparing experimental and theoretical results for a particular transition along a whole isoelectronic sequence is by use of a f versus Z^{-1} plot. This is appropriate because in the non-relativistic approximation the f-value can be expanded in terms of a series of inverse powers of the nuclear charge, Z, (see Appendix) i.e.,

$$f = f_o + f_1 Z^{-1} + f_2 Z^{-2} + \cdots \qquad (2\text{-}6)$$

In the limit of infinite Z the f-value approaches asymptotically the hydrogenic lead term f_o. For the case of the $\Delta n=0$ transitions studied in the present work the lead term vanishes in the non-relativistic approximation (due to the degeneracy of levels of same n in the hydrogenic limit). Thus f goes to zero proportional to $1/Z$ as $Z \to \infty$. However relativistic effects, which are negligible for small values of the nuclear charge but which become appreciable for highly-charged heavy ions, will cause the f-values to increase again before they ever reach zero.

Relativistic effects are of two main types. The velocity-dependent electron mass increase, which results in a shrinkage of electron orbits, has little effect on f-values for $Z \leq 50$. Configurational effects, which are associated with the breakdown of the LS coupling scheme due to the increasing magnitude of the magnetic (e.g. spin-

orbit) interactions relative to the residual interelectronic electrostatic repulsion term, are frequently non-negligible for $\Delta n=0$ transitions in ions of much lower Z i.e. $Z \gtrsim 25\text{-}30$. Since the f-value is proportional to both ΔE and S, changes in either quantity due to relativity must be considered. The line strength factor, S, is not appreciably affected by either mass increase or configurational breakdown corrections for $Z \lesssim 50$. The transition energy, ΔE, however is substantially affected even for moderately high Z systems by the breakdown of LS coupling and the need to resort to an intermediate-coupling scheme.

For lower Z systems the principal atomic structure problem is related to electron correlation effects. This is particularly true for $\Delta n=0$ transitions due to the interpenetrability of the wavefunctions of electrons with the same principal quantum number. The theoretical approach to the electron correlation problem involves either the use of multiconfigurational models (configuration interaction) or techniques such as the Non-Closed-Shell-Many-Electron-Theory (NCMET) of Sinanoglu and coworkers[6] which employs pair-correlation. As the nuclear charge Z increases along a sequence, the correlation effects associated with the interelectronic repulsion interactions become a less significant fraction of the total binding energy of the state due to the even greater increase of the electron-nuclear interaction. The element of the present study, i.e. chlorine, is of moderately high Z (Z=17) and is in the intermediate region between low Z systems where correlation effects

---

[6] O. Sinanoglu, Nuclear Instruments and Methods 110, 193 (1973); O. Sinanoglu and W. Luken, Journal of Chemical Physics 64, 4197 (1976).

are important and high Z systems where relativistic corrections associated with the magnetic interactions are significant. Correlation effects are not expected to be very important for chlorine ions with only a few electrons (say three or four), but may be non-negligible (due to accumulative effects) for ions with a larger number of electrons (say eight or nine). In most cases it is observed that the Z-expansion calculations involving only very limited correlation agree with the more sophisticated NCMET results for moderate-to-high Z members of a sequence even though there exist considerable differences between the two approaches for low Z ions.

It is to be expected that non-relativistic f-value regularities along isoelectronic sequences will show up in graphs of f versus Z^{-1} since Z^{-1} appears as a natural independent variable in the expansion. In addition, plotting the f-value data versus Z^{-1} has the advantage of compressing the entire isoelectronic sequence into the region between zero and the neutral atom value of Z^{-1}. One must however be careful in interpolating or extrapolating f-values from these plots due to certain potential difficulties. The first problem may arise in the readjustment of atomic terms with increasing Z along a sequence. Energy levels for very high Z systems are grouped according to the principal quantum numbers which is frequently not the case for neutral or near neutral systems. Such a regrouping can lead to the crossing of different terms over narrow regions of Z (usually at low stages of ionization). In these circumstances configuration-mixing effects may cause f-values to exhibit anomalous values. Another problem which can sometimes lead to

anomalous f-values is due to cancellations within the transition integrand that occur as the radial wave function nodes shift toward the origin with increasing Z. As mentioned previously, f-values tend to increase relative to the non-relativistic predictions for high Z members of a sequence due to relativistic effects. Again anomalous f-values may be expected over narrow regions of Z in this relativistic regime if the levels of one term approach those of another term as magnetic interactions become larger with increasing Z.

CHAPTER 3

EXPERIMENTAL METHOD

The beam-foil time-of-flight method for determining atomic lifetimes is simple in both conception and execution. A schematic of the apparatus that was used in the present investigation of radiative lifetimes of excited electronic states in multiply-charged chlorine ions is shown in Figure 3.1.

A well collimated and monoenergetic ion beam from an accelerator is passed through a thin foil, the two-fold purpose of which is to further strip the ions of electrons and excite the remaining electrons in a well-defined region of space (the foil is typically a few hundred atomic layers thick). The distribution of charge states following transmission through the foil is dependent upon the incident beam energy. Figure 3.2 shows the energy dependence of the post-foil charge state distribution for chlorine ions. The ion beam has a known incident energy since it undergoes momentum selection (using a calibrated magnetic analyzer) prior to deflection into the excitation chamber. The post-foil velocity of the beam determines the distance a beam particle moves between excitation (at the foil) and deexcitation ("signatured" by the emission of a photon) further downstream from the foil. The relative distance between excitation and deexcitation is varied in practice by changing the distance between the foil and the viewing region of some spectrally-isolating device such as a spectrometer. This time-of-flight technique is used to study the decay in intensity of isolated spectral lines which "signature" the radiative deexcitation of excited states of

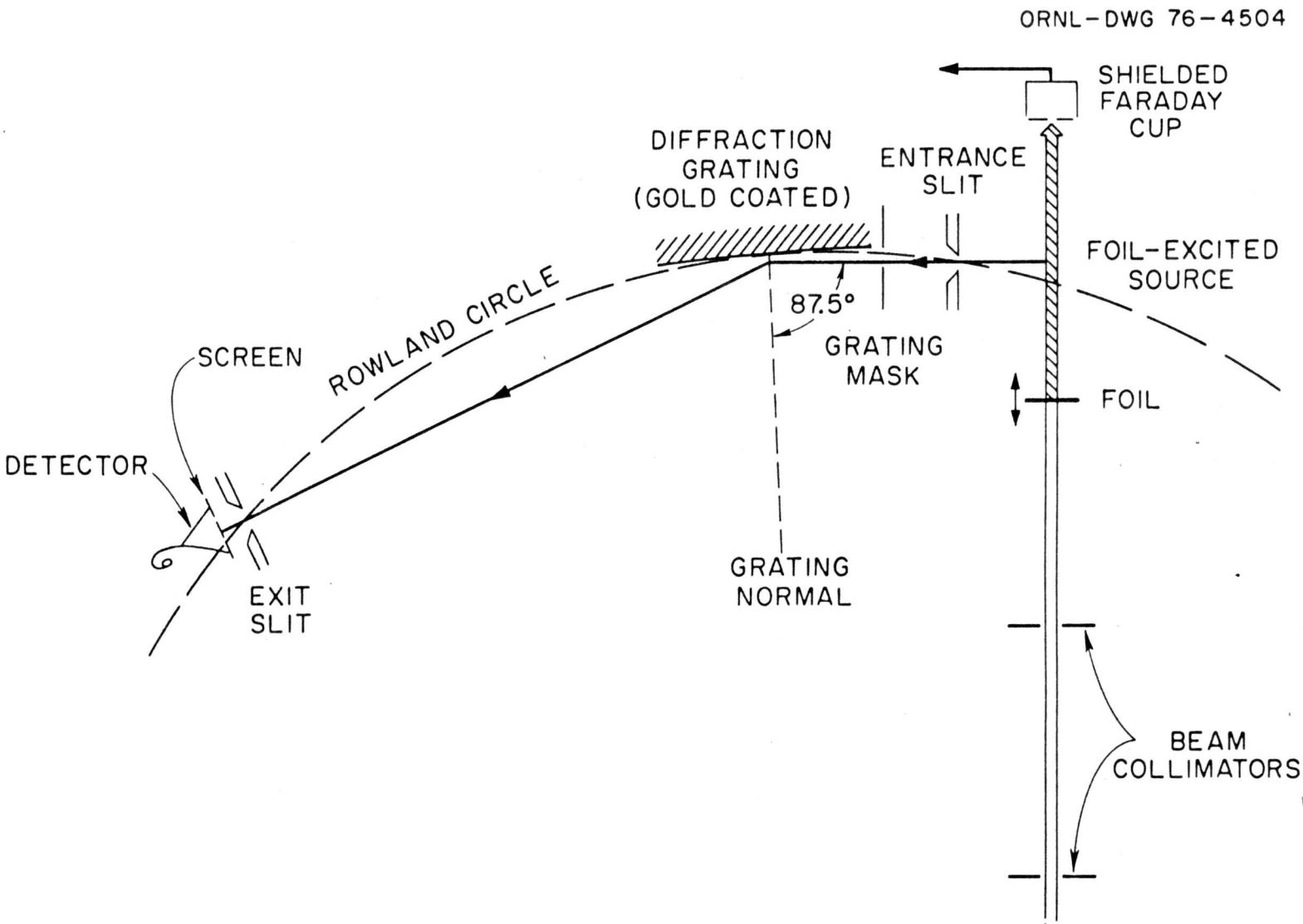


Figure 3.1. Schematic of apparatus used in the present study.

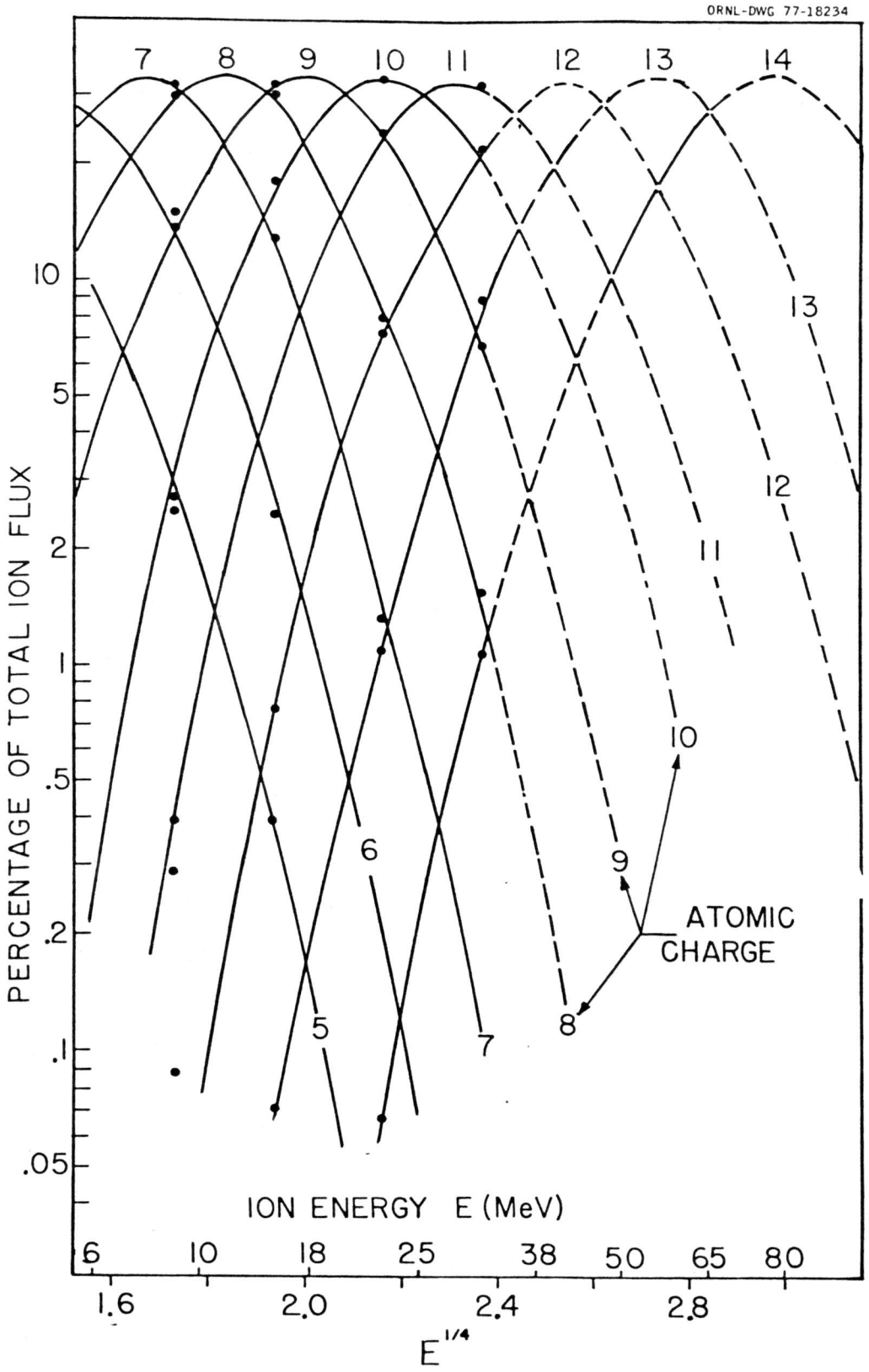


Figure 3.2 Equilibrium charge state distributions of chlorine ions emerging from a carbon foil.

foil-excited ions. The lifetime or mean life of the upper excited state is obtained by measuring the e-folding decay length of the line intensity and then scaling this spatial measurement into temporal coordinates by using the constant post-foil beam velocity.

One of the most desirable features of the beam-foil source is that following the passage through the foil the foil-excited ions decay in-flight downstream from the foil in a high vacuum (extremely low pressure) environment. The residual gas pressure, which is typically on the order of $\sim 10^{10}$ atoms/cm^3, corresponds to a mean free path of $\sim 10^4$ m for a beam ion with $\beta = v/c = 0.05$. A foil-excited ion is thus able to undergo spontaneous radiative decay being essentially free of any external perturbations. In most other radiation sources the excitation as well as the subsequent relaxation occurs in a moderately high density medium which increases the probability of externally-induced perturbations of the natural decay process. For example interionic fields, radiative recombination of beam ions and stray electrons, collisional non-radiative deexcitation, resonance radiation trapping, and the stimulated emission of radiation are all processes which could lead to an incorrect radiative lifetime determination.

For most beam-foil measurements it is not important to completely understand the physical processes that take place when the beam ions interact with the atoms of the foil. These ion-solid collision processes are however very interesting in themselves and several investigations have been reported.[7] The foil excitation process is non-selective in

---

[7]For example, E. Veje, Physical Review A14, 2077 (1976).

the sense that all excited states within an ionization stage are populated at the same time. Thus many different radiative transitions occur at different rates in the beam-foil source at any particular instant of time. A wavelength-selecting device is therefore essential to isolate a particular deexcitation channel of the state being studied. The photons emitted in a radiative deexcitation process "signature" the decay of the upper state of the transition. Several experimental arrangements may be used for this isolation and detecting purpose with the choice depending primarily on the wavelength of the radiation to be observed, the spectral resolution needed to isolate the line associated with the transition, and the intensity of the line being studied. Almost all measurements made today employ photoelectric detection. In the soft X-ray and extreme ultraviolet (EUV) spectral regions a channel electron multiplier is a preferred detector due to its extremely low noise and moderately good quantum efficiency.

In the present measurements on highly-stripped chlorine ions, thin carbon foils of nominal thicknesses $\sim 5 \mu g/cm^2$ were used to strip and excite energetic chlorine ion beam ions produced by the ORNL (High Voltage Engineering model EN) tandem accelerator. After acceleration the ion beam was magnetically analyzed (a process which determines the beam energy) and then deflected into the beam-foil apparatus. The incident beam energies were chosen to optimize the production of the desired charge states. The ion beam was collimated by placing two tantalum discs with apertures of diameter 0.476 cm spaced 20.955 cm apart between the target chamber and the last focusing and steering device (a magnetic

quadrupole-doublet lens) of the accelerator. This degree of collimation produces a beam entering the excitation chamber with a maximum divergence of 22.7 mr. Chlorine, being an electronegative element, provided an intense negative ion beam for injection into the tandem accelerator. Typical beam currents, as measured by the Faraday cup, ranged from 100 to 400 namp (it should be noted that each ion in the beam carried a charge of +qe and there exists a distribution of different ionization states in the post-foil source which is dependent upon the incident beam energy). The emitted foil-excited extreme-ultraviolet (EUV) radiation was dispersed and isolated with a 2.2 m (Mc Pherson model 247) grazing incidence monochromator. The wavelength-selected photons were converted to electronic pulses by a low-noise channel electron multiplier (CEM) detector. Some useful parameters associated with the present experiment situation are summarized in Table 3.1.

It is always necessary to normalize the intensity of the spectroscopically-analyzed radiation to some quantity which is proportional to the number of particles traversing the foil per second to insure that any fluctuations in beam intensity for example do not give rise to anomolous variations in the integrated signal. The normalization procedure can be accomplished in one of two ways. One method is to use a second detector, located at a fixed distance downstream from the excitor foil, which monitors the integrated (or spectrally-isolated) radiation emitted from the foil-excited beam. In order to monitor time-dependent changes in the foil's efficiency for production of a particular excitation-ionization state one needs to isolate a particular spectral line from a known charge state, but this is difficult in the extreme

TABLE 3.1

TYPICAL VALUES OF SOME PARAMETERS
ENCOUNTERED IN THIS EXPERIMENT

Beam energies	8.0 -45.5 MeV
Ion Velocities	$\beta = v/c = 0.022\text{-}0.053$
Lifetimes Measured	20 - 500 psec
Charge States Encountered	Cl XV - Cl IX
Excitor Foil Material	Carbon (amorphous)
Foil Aerial Density	$5\ \mu g/cm^2$
Ion Beam Currents	150 - 400 namp
Beam Particle Densities	300 - 1000 $/cm^3$
Particle Densities of Residual Gas Atoms in Excitation Chamber	10^{10} atoms/cm^3
Energy Range of Emitted Radiation Studied	460 Å(27 eV) - 160 Å(77eV)

ultraviolet (EUV) or soft X-ray region of the electromagnetic spectrum. The second technique, and the one used in the present investigation, is to normalize the intensity of the radiation signal to the amount of beam charge collected in a shielded Faraday cup placed downstream from the foil. The Faraday cup has a conducting ring at its entrance which is negatively biased by a few hundred volts in order to suppress any stray electrons that might be ejected from the inside of the cup when struck by the beam. It also repels stray electrons that are ejected from the foil itself toward the Faraday cup. A beam current integrator connected to the Faraday cup gives an output pulse when a pre-set amount of integrated beam charge has been collected in the cup. It is this signal that is used to normalize the spectroscopically analyzed photon intensity signal from the foil-excited beam. When using this method of normalization, care must be taken that the same number of beam particles are collected for each position of the foil at which data is taken. Due to multiple-scattering processes in the foil it is conceivable that the ions can pass through the viewing region and yet still not be collected by the cup. Multiple-scattering effects, which are most important for low velocity and high Z projectiles and targets, are not particularly significant in the present investigation which employs high velocity beams and low Z (carbon) foil targets.

For most experiments utilizing the beam-foil time-of-flight techniques of measuring lifetimes, carbon is chosen as the material for the target foil because it is an inexpensive, readily available, strong and durable material and its relatively low atomic number ($Z = 6$) lessens

the amount of potential Rutherford scattering of beam particles. A primary factor in the determination of a suitable foil thickness, especially for the higher charge state measurements, is that equilibrium ionization and excitation state distributions be established before the beam particles exit the foil. However it is advantageous to use as thin a foil as possible, consistent with the establishment of equilibrium conditions, since a thick foil scatters and straggles the beam more severely than a thin foil, its useful "lifetime" (the time before the foil breaks) is frequently less, and a greater fraction of the beam energy is lost in the thicker foil. In the present investigation it was decided to use foils of aerial density $\sim 5\ \mu g/cm^2$ since it appeared that they were the thinnest foil for which excitation-ionization equilibrium was attained at the beam energies employed. The foil targets lasted a long time under bombardment with the high energy beams used in this work. The amount of energy lost by a beam ion in a foil depends on both the foil thickness and the velocity of the ion. At the ion velocities used in this work the energy loss ranged from ~19 to ~25 keV per ion corresponding to a fractional energy shift of ~1.2% to ~0.3%. A correction was made for this energy loss when calculating the post-foil velocity to be used in the lifetime determinations. The uncertainty in the post-foil beam velocity so produced was negligible when compared to other sources of errors encountered in the measurements. Another potential problem which has been encountered in beam-foil measurements in the past is that there can exist an apparent time-dependent thickening of the foil with exposure to the beam, an effect which seems to saturate after a certain amount of exposure time. Care

was taken to expose the foil to the beam for a period of time (at least 30 minutes in the present work) before any lifetime data were taken. The foil wheel containing up to eight targets, mounted on a rotatable shaft that extended from the high vacuum region of the target chamber through a vacuum feed-through to the outside of the chamber where it could be rotated. Outside the target chamber this same shaft is a threaded screw of 24 threads per inch and was employed in the present work. An attached screw-drive system allows it to be translated parallel to the beam axis with the displacement measured by a dial indicator graduated in units of 0.001 cm. This system affords the ability to move the foil in precise discrete steps as small as 0.0005 cm and thus enable time-of-flight measurements to be made. The typical step size employed in the present study varied from a minimum of 0.002 cm (near the foil-zero position) to as large as 0.5 cm (for longer-lived decays and when the foil was relatively far from the foil-zero position). The foil drive mechanism was always moved in the direction of increasing distance from the entrance slit so that the mechanical force was always opposed in direction to the force of atmospheric pressure. The relative distance between the foil (i.e. the point of initial excitation) and the viewing region of the spectrometer can be varied in two ways. One can move the spectrometer relative to a fixed foil or move the foil relative to the spectrometer. Since the spectrometer is usually quite bulky, most beam-foil arrangements involve moving the excitor foil relative to a fixed spectrometer. The foil is translated parallel to the beam axis allowing the fixed spectrometer to view a

varying delay time following excitation. In the present experiment the foil position was changed manually when the accumulation of data for that particular foil setting was complete. The step size in the translation of the foil upstream of the viewing region was determined by the decay constants of the components of the decay curve. Data were accumulated at large enough distances from the foil to determine that no longer-lived components remained i.e. the signal level was down to the background. Time of accumulation for each data point could be varied somewhat to attain a certain level of counting statistics.

The Mc Pherson Model 247 monochromator used in the present study to isolate radiation from the foil-excited beam source is a typical grazing-incidence instrument with a spherical concave grating. A schematic of the instrument is shown in Figure 3.3. The gold-coated grating has a radius of curvature equal to 2.217 m and lies tangent to the Rowland circle of the instrument (the diameter of the circle is also 2.217 m). Radiation from the beam source emitted at 90° to the beam axis passes through the entrance-slit system (also situated on the Rowland circle) and strikes the grating at a mean angle of incidence of 87.5° (in the present investigation). The dispersed radiation is focused to a point which also lies on the Rowland circle. The exit-slit system, behind which is a photoelectric detector, is moved along the Rowland circle in order to "scan" the wavelength of the dispersed radiation.

Two gratings were available, one with 1200 grooves/mm and the second with 300 grooves/mm. The 300 grooves/mm grating has the best efficiency of light output versus input and was used in the present work even though the spectral resolution was somewhat inferior to that of the

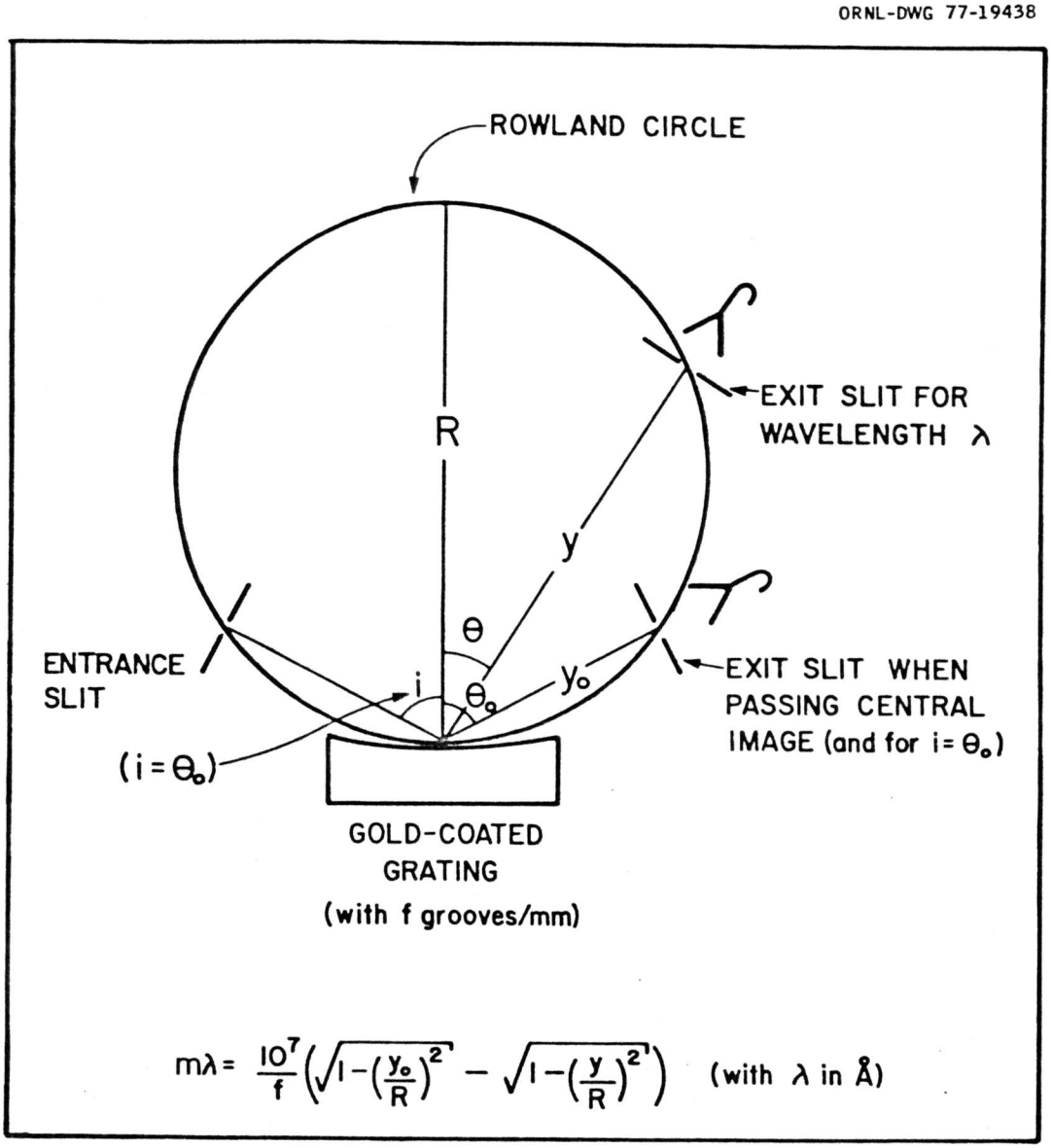


Figure 3.3. Schematic of grazing incidence spectrometer.

1200 grooves/mm grating. For the mean angle of incidence used (87.5^{o}) and the blaze angle of the grating of $2^{o}4'$; there corresponds a blaze wavelength of 191 Å. The grazing incidence instrument used here has a practical efficiency of less than 1% at the lowest wavelengths observed in the present experiment. This is mainly because the reflectivity of materials is extremely low in the EUV spectral region. Other undesirable characteristics such as astigmatism, curvature of spectral line images, non-linear dispersion, spherical abberations, etc. were not considered very important in the present study the emphasis of which is on lifetime measurements rather than high-resolution spectroscopy. The intrinsic strength of the EUV lines and a low-noise, moderately high quantum efficiency detector offset somewhat the low monochromator efficiency in the present work.

The standard grating equation is:

$$m\lambda = a(\sin i - \sin \theta) , \qquad (3.1)$$

where m is the order of interference, a is the distance between the grooves of the grating, and the angles i and θ are the angles of incidence and emergence respectively as shown in Figure 3.3. These angles are rather difficult to measure accurately with a grazing-incidence instrument but the relative differences in chord lengths for different positions of the exit slit along the Rowland circle can be determined precisely. A numerical register that is connected to the drive assembly displays the distance (x) in inches between the exit slit and the middle of the grating to within an additive constant (k). In terms of the quantities x and k we can rewrite the grating equation as:

$$m\lambda = \frac{10^7}{f}\left[\sqrt{1-\left(\frac{x_o-k}{R}\right)^2} - \sqrt{1-\left(\frac{x-k}{R}\right)^2}\right], \qquad (3.2)$$

where f is the number of grooves per mm on the grating surface. The values of f and R are quoted by the manufacturers and are known to one part in 10,000 and 17,000 respectively. Calibration of the wavelength scale of the instrument is accomplished by determining the values of x_o (the value of x when the exit slit is passing the central image) and values of x for lines of well-established wavelengths. In this work the position of lines of He I, He II, Ne II and Ar II, as produced by a hollow cathode source, were determined and fitted to the grating equation by a computer program in order to obtain a "best estimate" of the quantity k. Figure 3.4 shows some He I and He II lines that were used in the wavelength-calibration procedure. It was observed that while the values of f, R, and k remained constant throughout the experiment a shift in the position of central image (x_o) could occur. Any motion of the target chamber displaced the entrance slit assembly to which it was attached. It was found that a displacement of the entrance slit transverse to the beam axis of only 0.001" gave rise to a shift in the value of x_o of 0.025". It was therefore important to calibrate the monochromator periodically during the course of the experiment. Prior to each lifetime measurement survey spectral scans were made to determine the line centroid and the entrance and exit slit widths to be used. Slit widths were made as large as possible consistent with adequate temporal resolution and the elimination of blending of adjacent spectral features. Most lifetime measurements were made with slits of either 50 or 100 μm. Figure 3.5 is a schematic of the essential electronics which were used to control the accumulation of the spectral and lifetime data.

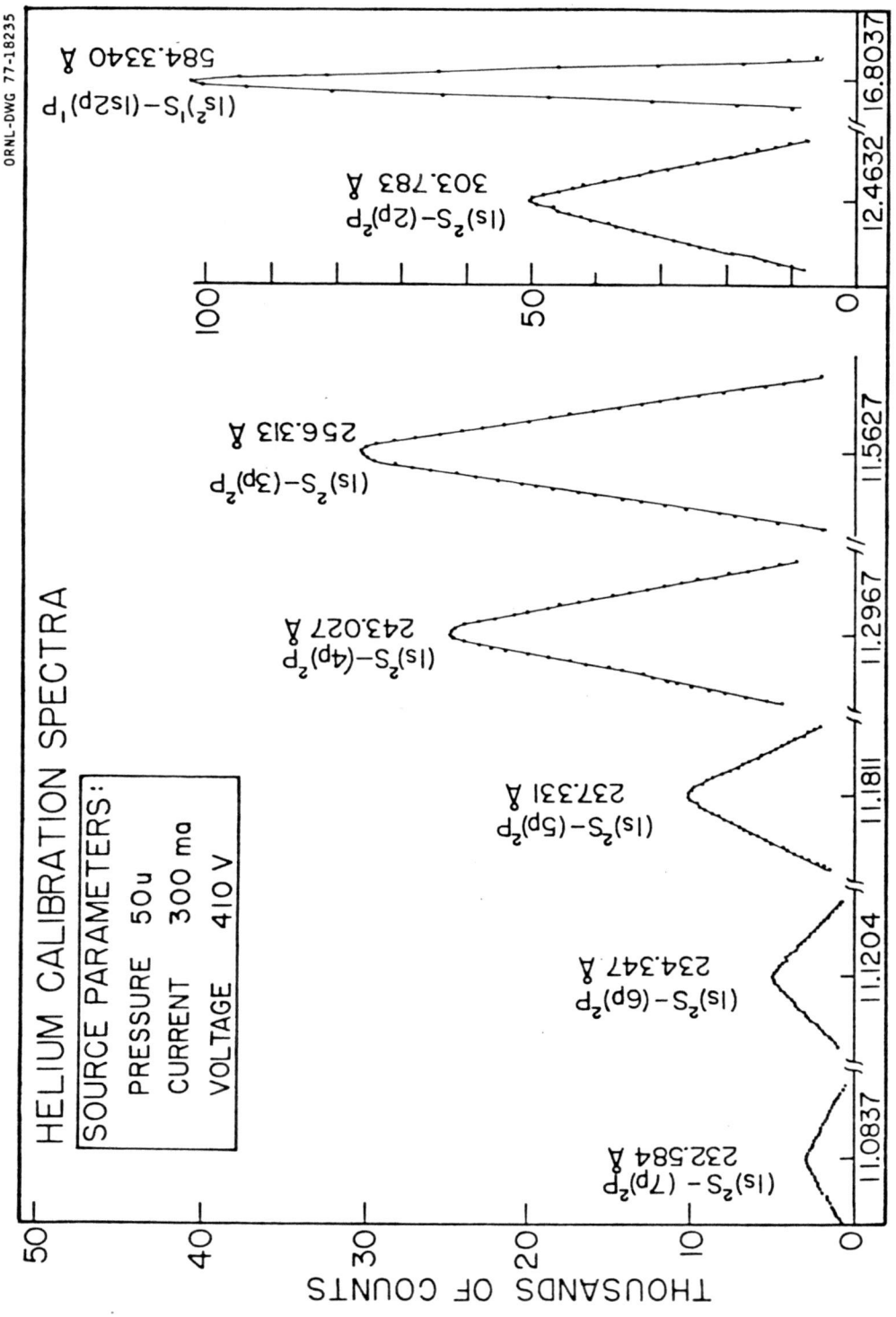


Figure 3.4. Some hollow cathode source lines used to wavelength-calibrate the grazing incidence spectrometer.

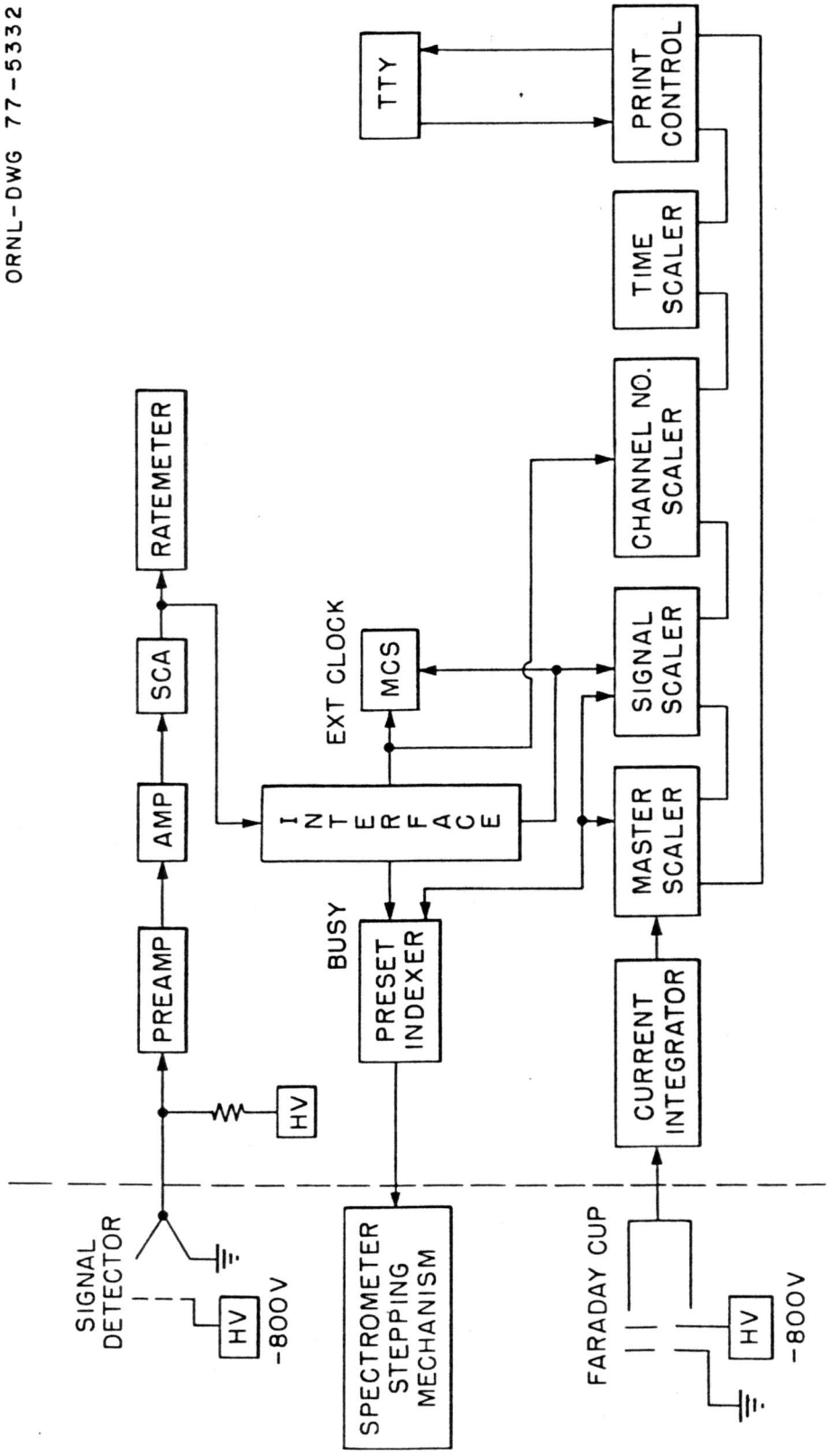


Figure 3.5. Schematic of electronic arrangement used in the present experiment.

Two different detectors, both channel electron multipliers (CEM), were used in the present work. A Mullard (Model B419B1/01) CEM was operated at 2950 V. Later in the work a lower noise Ceratron (Model EMS-1081B) CEM detector operating at 4000 V was used. The high voltage was applied to the output end of the detector through a ballast resistor with the entrance of the detector grounded. A negatively-biased (-1000V) screen that had a 90% transmittance for radiation was situated in front of the detector in order to repel stray electrons from the beam source. The average noise of the Mullard CEM detector was ~0.3 Hz while that of the Ceratron was ~0.005 Hz. The detector walls were made of a high resistance semi-conductor material. An electron photo-ejected from the detector walls near the entrance is accelerated toward the high positive potential striking the walls and producing a cascading effect as it travels. The negative output pulse thus produced was first fed into a charge-sensitive preamplifier and then into an amplifier. A single channel analyzer (SCA) was used to both shape the pulses and discriminate against low-voltage noise. Pulses transmitted by the SCA were fed into a "signal" scaler. Integrated beam charge from the Faraday cup was sent to the master scaler. Other scalers monitored the time of accumulation and the number of data steps taken. When the desired amount of beam charge had been collected by the Faraday cup the signal accumulation was halted and data from all the scalers was printed out by a teletype device which provided a "hard" copy of the data. The option was also available to accumulate data in the multiscaler mode using the multi-scaling capabilities of a multichannel analyzer. An interface module

prevented the signal scaler from accumulating when either the teletype was operating or when the stepping motor of the monochromator was changing to a new wavelength position. A beam-independent background correction was determined for each data point by multiplying the "dark-current" rate of the detector by the time of accumulation. The "dark-current" rate was determined throughout the experiment by isolating the spectrometer from the beam source. Beam-dependent background corrections were found to be small and were determined by "detuning" the monochromator on each side of the spectral line whose decay was being studied.

Figure 3.6 shows the geometrical arrangement of the beam axis, the entrance-slit system of the monochromator and the grating mask. The aperture dimensions and spacings shown in Figure 3.6 determine the length of excited beam source viewed by the spectrometer. This source length is frequently termed the spatial resolution (Δx) along the beam or sometimes the viewing region or window.

It can easily be shown that the length of the penumbra (ΔL) is given by the expression:

$$\Delta L = \frac{p}{q} (b + a) + a \ , \qquad (3.3)$$

and the length of the umbra (Δw) is calculated by the equation:

$$\Delta_w = \frac{p}{q} (b - a) - a \ , \qquad (3.4)$$

with the quantities being defined in Figure 3.6.

We will refer to the spatial resolution (Δx) as the average of the quantities ΔL and Δw:

$$\Delta x = 1/2 \ \ (\Delta L + \ w). \qquad (3.5)$$

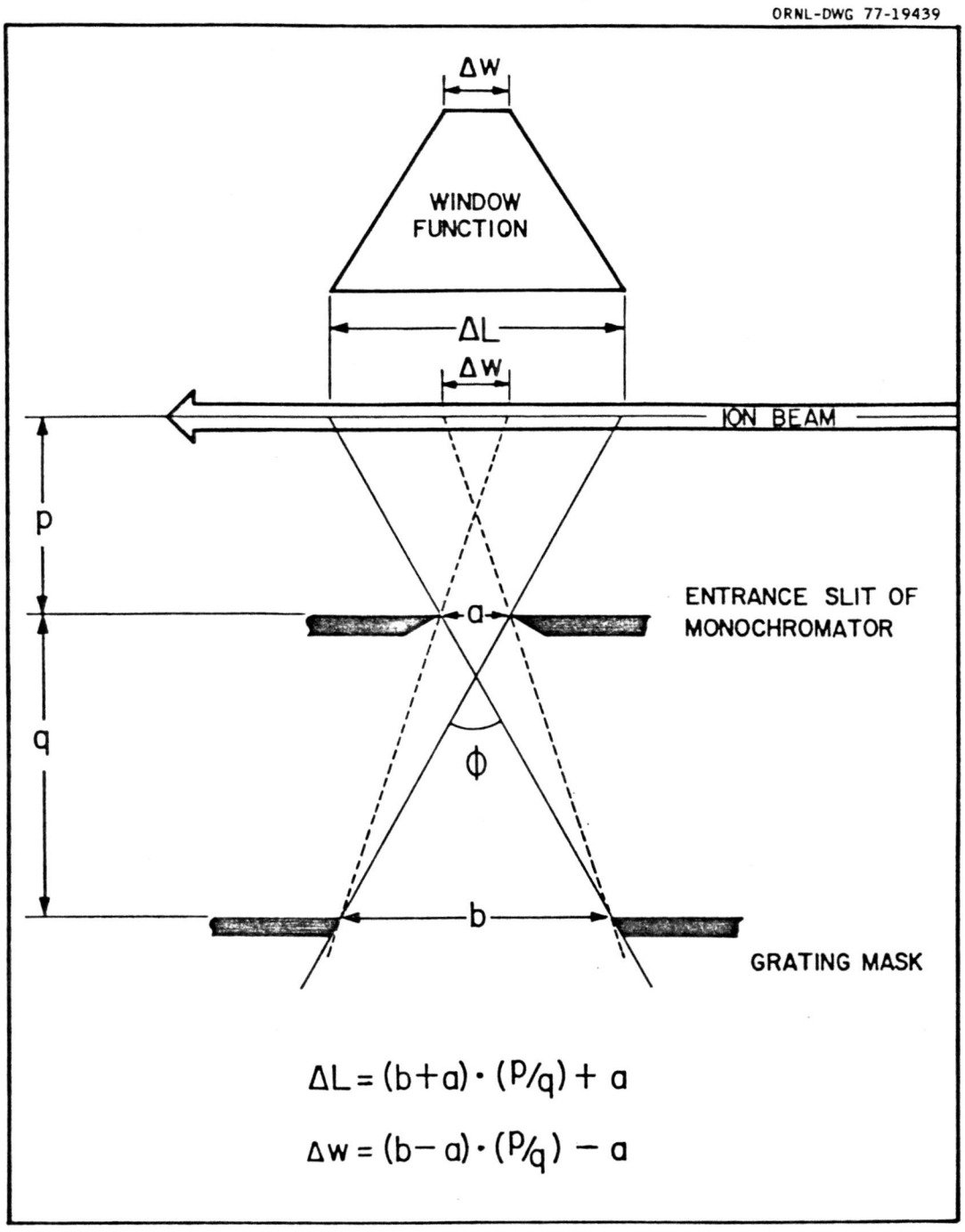


Figure 3.6. Schematic showing the relationship of the beam axis, the entrance slit and grating mask system of the monochromator.

Throughout the course of the experiment the values of the grating mask (b), the spacing between the exit slit jaws and the beam axis (p) and the distance from the entrance slit to the grating mask (q) all remained unchanged and are listed in Table 3.2.

TABLE 3.2

PARAMETERS OF THE SPECTROMETER NECESSARY TO CALCULATE THE WINDOW

q	=	6.24 cm
p	=	3.81 cm
b	=	0.38 mm

The trapezoid window function shown in the upper part of Figure 3.6 is purely geometrical and is determined by calculating the length of the umbra and penumbra of the source which are themselves determined by the aperture sizes, their relative spacings, and the distance of the source from the first aperture. In reality the window function of the apparatus will be somewhat more complex since the reflectivity of the gold-coated grating is highly dependent upon the angle of incidence for the wavelengths and the mean angle (87.5^{o}) used in this experiment. A decrease in the angle of incidence corresponds to a reduction in reflectivity and so light emitted by ions deexciting in the upstream position of the viewing region is slightly more attenuated than for light emitted from positions further downstream. This dependence of the reflectivity of the grating on the angle of incidence should be folded into the

geometric window function to yield the true spatial intensity profile. However in the present arrangement, the range of incident angles is small ($\pm 0.22^{\circ}$ from the mean angle of 87.5^{0}) and so the aforementioned effect is expected to be small. A "prompt" transition ($\sim$25 psec) was investigated in an attempt to study the shape of the true window function experimentally. The result of this measurement is shown in Figure 3.7. This study was not completely successful however since there appears to be some longer-lived tail on the lower-right hand side of the decay plot causing skewing of this side. It is thought that the present apparatus is capable of making lifetime measurements down to $\sim$25 psec without having to resort to complicated window-deconvoluting procedures. If the post-foil beam velocity, v, is known, the time of transit, Δt, of the beam ions across the viewing window, Δx, of the spectrometer can be determined by:

$$\Delta t = \Delta x/v \quad , \tag{3.6}$$

(this quantity is often refered to as the temporal resolution of the apparatus). For a 38 MeV chlorine beam the temporal resolution is estimated to be $\sim$16 psec (using 50μm entrance slits)

One consequence of the fact that the ion emitters form a fast, unidirectional beam source of finite length is that spectral lines will be both Doppler-shifted and broadened in wavelength. The magnitude of the first-order fractional shift depends upon the beam velocity and the angle of emission of the radiation with respect to the beam direction. Thus a spectral feature can be either red-shifted or blue-shifted with respect to the rest-frame wavelengths according to whether the source

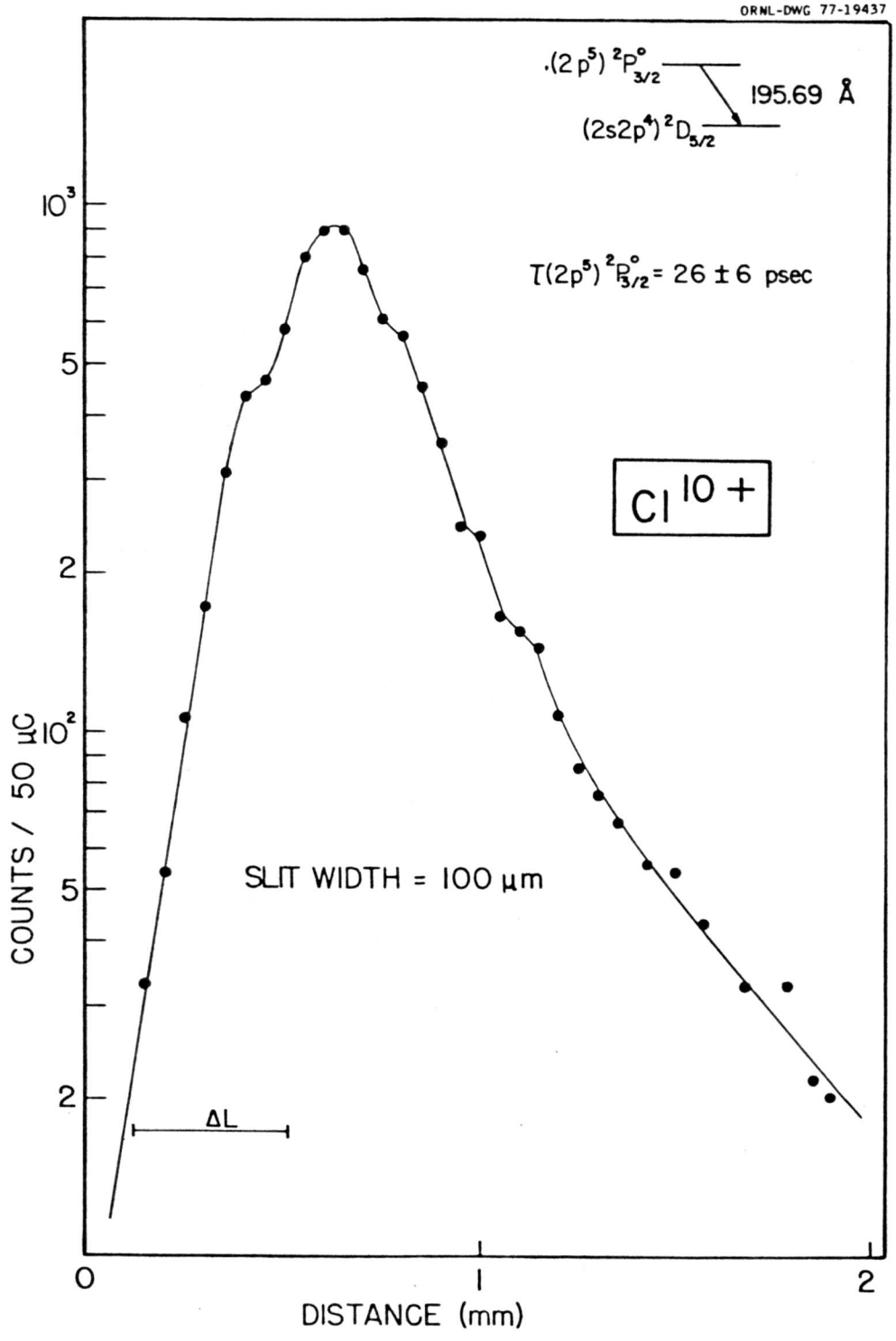


Figure 3.7 Intensity decay curve for a short-lived transition. This figure shows the instrumental window convoluted with an exponential function.

ion has a velocity component along the line of sight of the spectrometer approaching (blue-shifted) or receding (red-shifted) from the spectrometer. The second-order Doppler shift (relativistic) is independent of the angle of observation and is always a red shift. The total Doppler shift is given by:

$$\Delta\lambda/\lambda_o \simeq \beta\cos\theta + (1/2)\beta^2 + \cdots \quad , \quad (3.7)$$

where β is the velocity of the beam ion relative to that of light, θ is the angle of observation and λ_o is the rest-frame wavelength of the line. The mean angle of observation in the present work was nominally 90° which eliminates the first order shift. In actual fact a small first order contribution remains since it is very difficult to set the observation angle to 90° exactly. The second-order shift can become appredíable at high beam energies. For example, for a 39 MeV chlorine beam and a 200 Å wavelength line this quantity amounts to ~0.2 Å. The total fractional Doppler shift was experimentally determined in the present work in the following manner. The measured wavelength (the spectrometer wavelength scale was calibrated in this region with the He II Lyα line) of the foil-excited Si XI, $(1s^2 2s^2)^1S_0 - (1s^2 2s2p)^1P_1$, resonance line was compared with its well-established rest-frame wavelength. After subtraction of the second-order correction from the total shift it was possible to compute the mean angle of observation, θ. Since this angle depended only upon the geometry of the apparatus it could be also used to correct the wavelengths of lines for the chlorine ions studied in the present work.

Doppler-broadening effects occur as a result of the finite acceptance angle of the spectrometer (0.44° in the present arrangement). Radiation emitted from the source with some range of emission angles will enter the spectrometer leading to a symmetric line broadening due to the corresponding range of blue and red Doppler shifts. Lines can be asymetrically broadened if the decay length is comparable to or smaller than the source length. The fractional Doppler broadening will be proportional to the acceptance angle i.e.:

$$\Delta\lambda/\lambda_{o} \simeq \beta\alpha \quad . \tag{3.8}$$

At the short wavelengths studied in the present work ($\lambda \sim 100\text{-}400$ Å) and with the relatively small acceptance angle employed ($\alpha = 0.44^{\circ}$), Doppler broadening of the spectral features was not a problem to contend with. For example, at 38 MeV a 200 Å line from the foil-excited source will be broadened by an amount $\Delta\lambda = 0.074$ Å. This is less than the instrumental width of spectral lines at the 50 μm slit widths used in many of the spectral studies.

CHAPTER 4

RESULTS

SPECTRA

Most of the spectra were taken at beam energies of either 38 or 18 MeV using a 5 $\mu g/cm^2$ C foil as the target material. Table 4.1 lists and identifies many of the peaks observed in the spectral scan taken at 38 MeV. Figures 4.1, 4.2, and 4.3 show the spectral data with the circled numbers above the peaks corresponding to the peak-identification numbers shown in Table 4.1. The data shown in these plots have not been corrected for background. In Figure 4.1 the instrumental bandpass of 0.375 Å (fwhm) is indicated by the arrows at the half maximum of peak number 10. The "step size" (i.e. the change in chord length, as measured from the center of the grating to the exit slit, for each data point) was 0.0015 inches for these measurements which corresponds to approximately 10 data points per peak, depending upon the wavelength viewed. Table 4.2 summarizes the results of the spectral scans taken with a beam energy of 18 MeV and Figure 4.4 shows this spectrum. The instrumental bandpass used in the 18 MeV measurements was 0.75 Å (fwhm). A "step size" of 0.005 inches was used for these measurements which corresponds to approximately 8 data points per peak. The estimated uncertainty in the wavelengths quoted is in general $\pm$ 0.1 Å for strong and unblended spectral features. For weak and/or partially blended features the estimated uncertainty is 0.1 Å - 0.3 Å. Experimental wavelengths listed in Tables 4.1 and 4.2 have been corrected for first and second order Doppler shifts using the

TABLE 4.1

SPECTRUM OF FOIL-EXCITED Cl IONS AT 38 MeV INCIDENT BEAM ENERGY

Peak No.	Spectrum	Transition	Measured Wavelength (Å)			Line Intensity Relative to Peak No. 10[d]
			Present Work[a]	Other Measurements Ref.[b]	Other Measurements Ref.[c]	
1	Cl XIII	$(2s^2 2p)^2P_{1/2} - (2s2p^2)^2P_{3/2}$	195.2	195.217	195.22	2
2	Cl XI	$(2s2p^4)^2D_{5/2} - (2p^5)^2P_{3/2}$	195.6	195.69	195.69	2
3		unclassified	196.0			1
4	Cl XII	$(2s2p^3)^3D_1 - (2p^4)^3P_0$	196.3	196.22	196.33	2
5		unclassified	196.7			2
6	Cl XII	$(2s2p^3)^3D_2 - (2p^4)^3P_1$	197.5	197.543		2
7	Cl XII	$(2s2p^3)^3D_1 - (2p^4)^3P_1$	197.6	197.69		1
8	Cl XIII	$(2s^2 2p)^2P_{1/2} - (2s2p^2)^2P_{1/2}$	198.3	198.365	198.40	1
9		unclassified	198.9			1
10	Cl XII	$(2s^2 2p^2)^1D_2 - (2s2p^3)^1D_2$	199.3	199.349	199.37	10
11	Cl XII	$(2s^2 2p^2)^1S_0 - (2s2p^3)^1P_1$	200.9	200.920	200.96	1
12	Cl XIII	$(2s^2 2p)^2P_{3/2} - (2s2p^2)^2P_{3/2}$	202.1	202.088	202.10	9
	Cl XII	$(2s2p^3)^3D_2 - (2p^4)^3P_2$		202.29		

TABLE 4.1 (continued)

Peak No.	Spectrum	Transition	Measured Wavelength (Å) Present Work[a]	Other Measurements Ref.[b]	Other Measurements Ref.[c]	Line Intensity Relative to Peak No. 10[d]
13	Cl XII	$(2s2p^3)^3D_1 - (2p^4)^3P_2$	202.6	202.45		5
	Cl XII	$(2s2p^3)^3D - (2p^4)^3P_2$		202.563	202.54	
14	Cl X	$(2s^22p^4)^3P_1 - (2s2p^5)^3P_0$	203.9	203.80		1
15	Cl X	$(2s^22p^4)^3P_2 - (2s2p^5)^3P_2$	205.5	205.4		5
	Cl XIII	$(2s^22p)^2P_{3/2} - (2s2p^2)^2P_{1/2}$		205.464	205.47	
16	Cl XI	$(2s^22p^3)^2D_{3/2} - (2s2p^4)^2D_{5/2}$	209.3	209.04		5
17	Cl XI	$(2s^22p^3)^2D_{3/2} - (2s2p^4)^2D_{3/2}$	209.4	209.18	209.18	5
18	Cl XIII	$(2s^22p)^2P_{1/2} - (2s2p^2)^2S_{1/2}$	209.9	209.797	209.81	7
	Cl XI	$(2s^22p^3)^2D_{5/2} - (2s2p^4)^2D_{5/2}$		209.93	209.93	
19	Cl XI	$(2s^22p^3)^2D_{5/2} - (2s2p^4)^2D_{3/2}$	210.0	210.07		8
20	Cl XIII	$(2s2p^2)^2D_{3/2} - (2p^3)^2P_{3/2}$	215.3	214.94		3
	Cl XIII	$(2s2p^2)^2D_{5/2} - (2p^3)^2P_{3/2}$		215.183		
21	Cl X	$(2s2p^5)^1P_1 - (2p^6)^1S_0$	215.5	(Previously unreported)		1

TABLE 4.1 (continued)

Peak No.	Spectrum	Transition	Measured Wavelength (Å)			Line Intensity Relative to Peak No. 10[d]
			Present Work[a]	Other Measurements Ref.[b]	Ref.[c]	
22	Cl XIII	$(2s2p^2)^2D_{3/2} - (2p^3)^2P_{1/2}$	216.3	216.179		3
23	Cl XIII	$(2s^22p)^2P_{3/2} - (2s2p^2)^2S_{1/2}$	217.9	217.749		1
24	Cl XII	$(2s^22p^2)^3P_0 - (2s2p^3)^3P_1$	219.5	219.529		2
25	Cl XIII	$(2s2p^2)^4P_{1/2} - (2p^3)^4S_{3/2}$	221.4	221.362	221.38	2
26	Cl XII	$(2s^22p^2)^3P_1 - (2s2p^3)^3P_2$	222.7	222.696		1
27	Cl XII	$(2s^22p^2)^3P_1 - (2s2p^3)^3P_1$	222.9	223.061	223.10	1
28	Cl XII	$(2s^22p^2)^3P_1 - (2s2p^3)^3P_0$	223.2	223.141	223.14	3
29	Cl XIII	$(2s2p^2)^4P_{3/2} - (2p^3)^4S_{1/2}$	224.6	224.573	224.60	4
30			224.7			4
31	Cl XII	$(2s2p^3)^3P_1 - (2p^4)^3P_0$	226.0	225.90		1
32		unclassified	227.0			1
33	Cl XII	$(2s^22p^2)^3P_2 - (2s2p^3)^3P_2$	227.5	227.450		5

TABLE 4.1 (continued)

Peak No.	Spectrum	Transition	Measured Wavelength (Å) Present Work[a]	Other Measurements Ref.[b]	Ref.[c]	Line Intensity Relative to Peak No. 10[d]
34	Cl XII	$(2s^2 2p^2)\,^3P_2 - (2s2p^3)\,^3P_1$	227.9	227.833		2
	Cl XII	$(2s2p^3)\,^3P_1 - (2p^4)\,^3P_1$		227.85		
35	Cl XIII	$(2s2p^2)\,^4P_{5/2} - (2p^3)\,^4S_{3/2}$	229.2	229.130		5
36	Cl XII	$(2s2p^3)\,^3P_2 - (2p^4)\,^3P_2$	234.7	234.59		3
	Cl XI	$(2s^2 2p^3)\,^2P_{3/2} - (2s2p^4)\,^2D_{5/2}$		234.66	234.67	
	Cl XI	$(2s^2 2p^3)\,^4S_{3/2} - (2s2p^4)\,^4P_{1/2}$		234.83	234.84	
37	Cl XII	$(2s^2 2p^2)\,^3P_1 - (2s2p^3)\,^3D_2$	262.4	262.487	262.60	2
38	Cl XIII	$(2s^2 2p)\,^2P_{1/2} - (2s2p^2)\,^2D_{3/2}$	264.6	264.667	264.78	2
39	Cl XIII	$(2s2p^2)\,^2D_{3/2} - (2p^3)\,^2D_{5/2}$	268.2	268.25		1
40	Cl XII	$(2s^2 2p^2)\,^3P_2 - (2s2p^3)\,^3D_3$	268.6	268.63		6
	Cl XIII	$(2s2p^2)\,^2D_{5/2} - (2p^3)\,^2D_{5/2}$		268.64	268.77	
41	Cl XII	$(2s^2 2p^2)\,^3P_2 - (2s2p^3)\,^3D_2$	269.2	269.123		1
	Cl XIII	$(2s2p^2)\,^2D_{3/2} - (2p^3)\,^2D_{3/2}$		269.13	269.21	

TABLE 4.1 (continued)

Peak No.	Spectrum	Transition	Measured Wavelength (Å)			Line Intensity Relative to Peak No. 10[d]
			Present Work[a]	Other Measurements Ref.[b]	Ref.[c]	
42	Cl XII	$(2s2p^3)^1D_2 - (2p^4)^1D_2$	271.2	(previously unreported)		5
43	Cl XIII	$(2s2p^2)^2S_{1/2} - (2p^3)^2P_{3/2}$	272.9	272.87		1
44	Cl XIV	$(2s2p)^3P_1 - (2p^2)^3P_2$	276.0	276.000	276.13	1
45		unclassified	276.3			1
46	Cl XIII	$(2s^22p)^2P_{3/2} - (2s2p^2)^2D_{3/2}$	277.1	277.455	277.59	3
47	Cl XIV	$(2s2p)^1P_1 - (2p^2)^1S_0$	277.9	277.94		1
48		unclassified	279.1			1
49	Cl XIV	$(2s2p)^3P_0 - (2p^2)^3P_1$	279.8	279.718		1
50	Cl XIV	$(2s2p)^3P_1 - (2p^2)^3P_1$	284.1	284.173	284.31	1
51	Cl XIV	$(2s2p)^3P_2 - (2p^2)^3P_2$	286.1	286.183	286.183	2
52	Cl XIV	$(2s2p)^3P_1 - (2p^2)^3P_0$	290.4	290.479	290.51	1
53	Cl XIII	$(2s2p^2)^2P_{1/2} - (2p^3)^2P_{3/2}$	295.1	295.01	290.7	1
	Cl XIV	$(2s2p)^3P_2 - (2p^2)^3P_1$		295.016	295.05	

TABLE 4.1 (continued)

Peak No.	Spectrum	Transition	Measured Wavelength (Å) Present Work[a]	Other Measurements Ref.[b]	Ref.[c]	Line Intensity Relative to Peak No. 10[d]
54	Cl XIII	$(2s2p^2)^2P_{1/2} - (2p^3)^2P_{1/2}$	297.4	297.36		1
55	Cl XIII	$(2s2p^2)^2P_{3/2} - (2p^3)^2P_{3/2}$	302.3	302.26	302.24	2
56	Cl XIII	$(2s2p^2)^2P_{3/2} - (2p^3)^2P_{1/2}$	304.7	304.73		1

[a]Measured wavelength corrected for first and second-order Doppler shifts. Under optimum conditions (i.e. intense and unblended spectral features) the wavelength uncertainty is estimated at ± 0.1 Å. Weak and/or partially blended lines can only be determined to ± 0.1 Å to 0.3 Å. The instrumental bandpass employed is 0.38 Å (fwhm).

[b]B. C. Fawcett, Atomic Data and Nuclear Data Tables 16, 135 (1975).

[c]R. L. Kelly and L. J. Palumbo, Naval Research Laboratory Report NRL 7599 (washington, DC, 1973).

[d]Note that this scale is only relative since the efficiency of the apparatus varies with the wavelength.

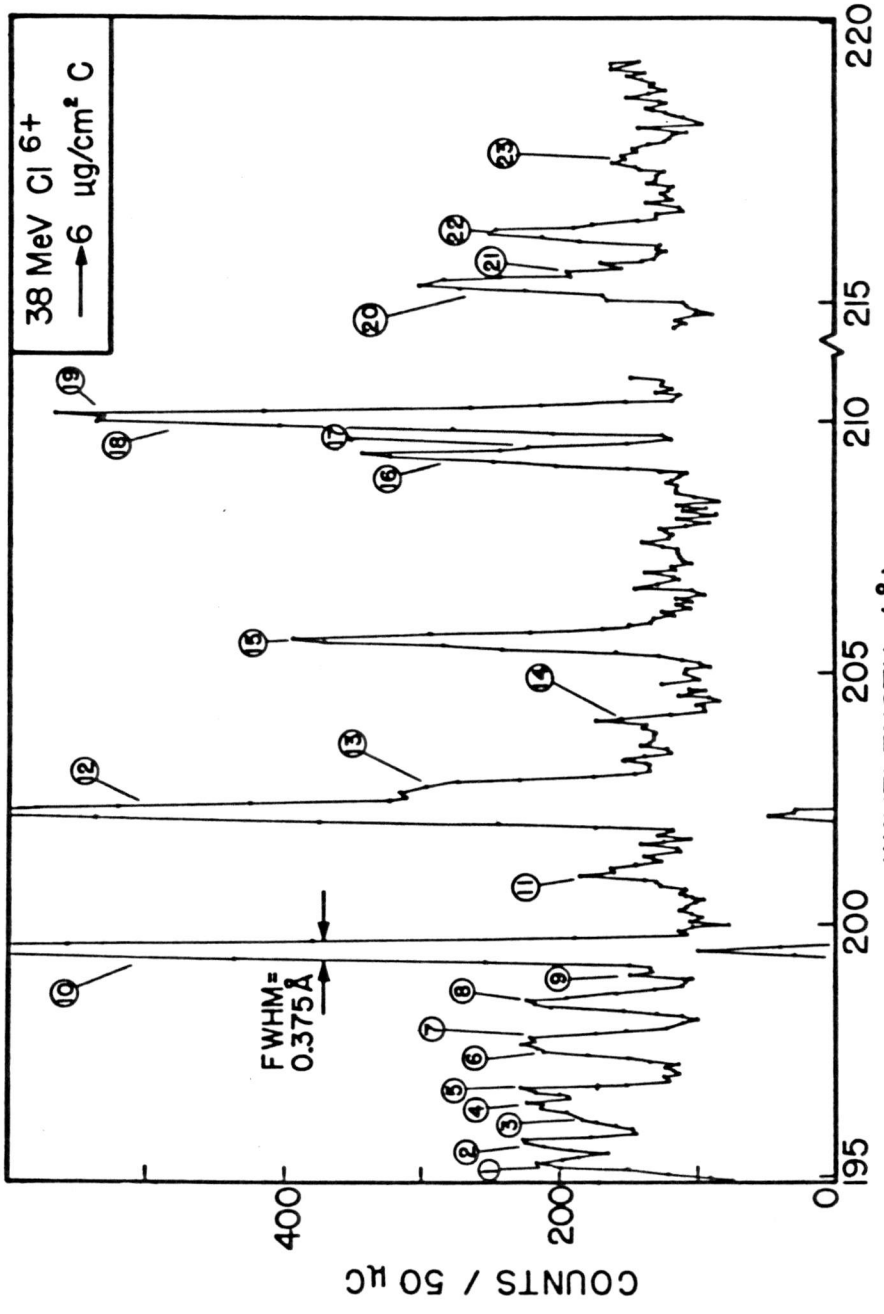


Figure 4.1. Spectrum of foil-excited chlorine ions ($195 \leq \lambda \leq 220$ Å) taken at an incident beam energy of 38 MeV. See Table 4.1 for identification.

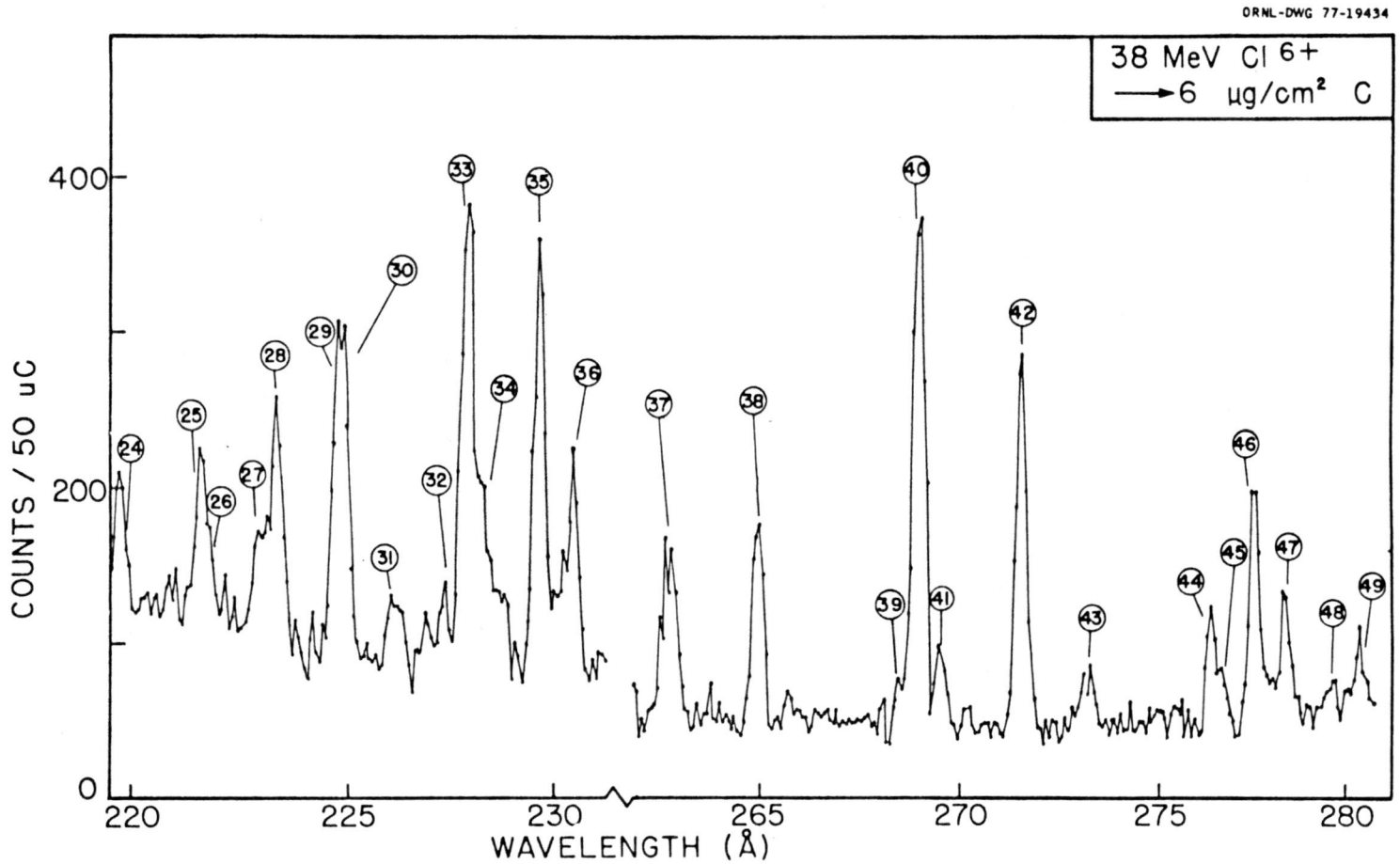


Figure 4.2. Spectrum of foil-excited chlorine ions ($220 \leq \lambda \leq 280$ Å) taken at an incident beam energy of 38 MeV. See Table 4.1 for identification.

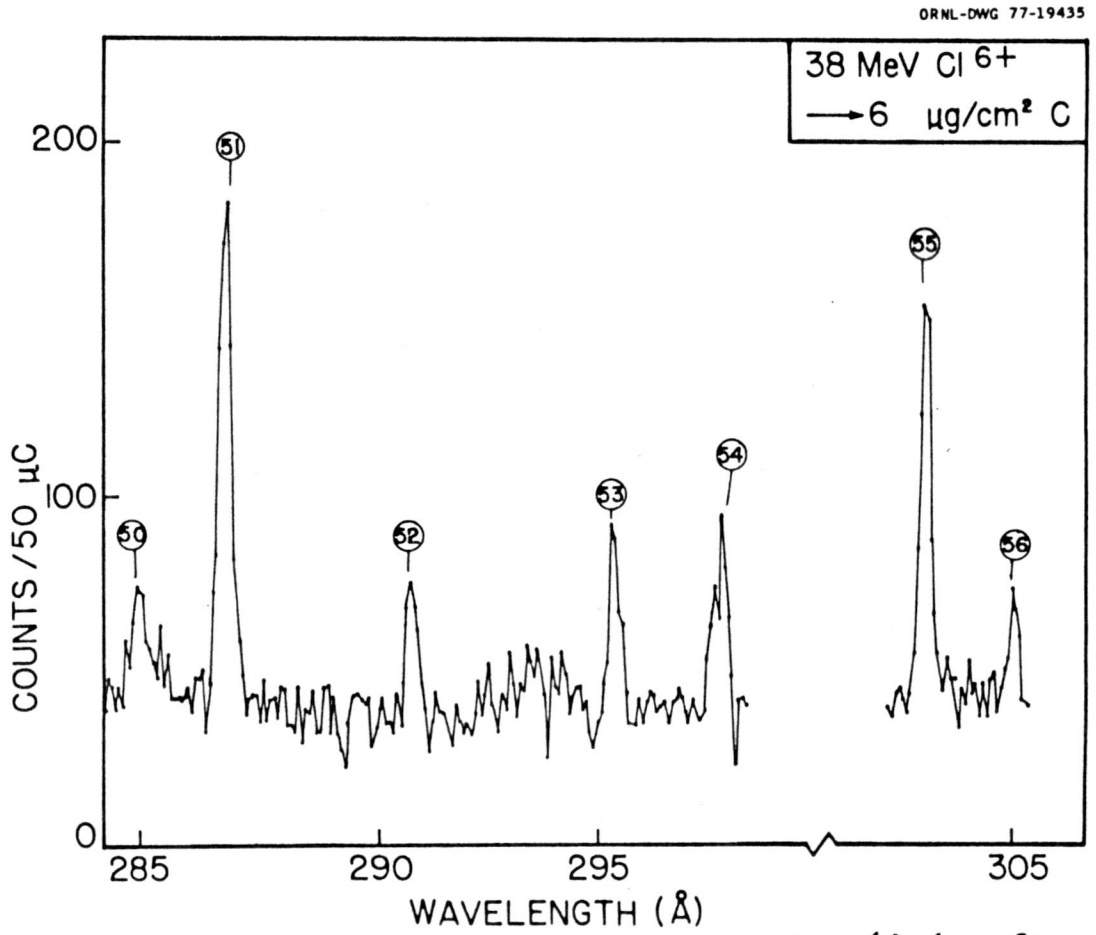


Figure 4.3. Spectrum of foil-excited chlorine ions ($285 \leq \lambda \leq 305$ Å) taken at an incident beam energy of 38 MeV. See Table 4.1 for identification.

TABLE 4.2

SPECTRUM OF FOIL-EXCITED Cl IONS AT 18 MeV INCIDENT BEAM ENERGY

Peak No.	Spectrum	Transition	Measured Wavelength (Å) Present Work[a]	Other Measurements Ref.[b]	Other Measurements Ref.[c]	Line Intensity Relative to Peak No. 10[d]
1	Cl X	$(2s2p^4)^1D_2 - (2s2p^5)^1P_1$	164.5	164.51	164.5	10
2	Cl XI	$(2s^22p^3)^2D_{5/2} - (2s2p^4)^2P_{3/2}$	166.6	166.63		7
3		unclassified	168.61			1
4		unclassified	169.7			1
5	Cl XII	$(2s^22p^2)^3P_0 - (2s2p^3)^3S_1$	172.4	172.123	172.06	1
6		unclassified	173.2			2
7	Cl XII	$(2s^22p^2)^3P_1 - (2s2p^3)^3S_1$	174.4	174.229	174.21	2
8	Cl XII	$(2s^22p^2)^1D_2 - (2s2p^3)^1P_1$	175.8	175.721	175.71	2
9	Cl XI	$(2s^22p^3)^2P_{1/2} - (2s2p^4)^2P_{1/2}$	177.1	177.00	177.00	2
	Cl XII	$(2s^22p^2)^3P_2 - (2s2p^3)^3S_1$		177.066	177.11	
10	Cl XI	$(2s^22p^3)^2P_{3/2} - (2s2p^4)^2P_{1/2}$	178.1	177.96	177.96	1
11	Cl IX	$(2s^22p^5)^2P_{3/2} - (2s2p^6)^2S_{1/2}$	180.8	180.71		3
	Cl XI	$(2s^22p^3)^2P_{1/2} - (2s2p^4)^2P_{3/2}$		180.85	180.85	

TABLE 4.2 (continued)

Peak No.	Spectrum	Transition	Measured Wavelength (Å) Present Work[a]	Other Measurements Ref.[b]	Other Measurements Ref.[c]	Line Intensity Relative to Peak No. 10[d]
12	Cl XI	$(2s^2 2p^3)^2P_{3/2} - (2s2p^4)^2P_{3/2}$	181.9	181.84	181.84	1
13	Cl IX	$(2s^2 2p^5)^2P_{1/2} - (2s2p^6)^2S_{1/2}$	185.4	185.26		1
14	Cl X	$(2s^2 2p^4)^1S_0 - (2s2p^5)^1P_1$	186.0	186.06	186.06	1
15	Cl X	$(2s^2 2p^4)^3P_2 - (2s2p^5)^3P_1$	201.5	201.50	201.50	2
	Cl XII	$(2s2p^3)^3D_2 - (2p^4)^3P_2$		202.29		
16	Cl XII	$(2s2p^3)^3D_1 - (2p^4)^3P_2$	202.3	202.45		2
	Cl XII	$(2s2p^3)^3D_3 - (2p^4)^3P_2$		202.563		
17	Cl X	$(2s^2 2p^4)^3P_1 - (2s2p^5)^3P_0$	203.8	203.80	203.80	1
18	Cl X	$(2s^2 2p^4)^3P_2 - (2s2p^5)^3P_2$	205.5	205.40	205.40	5
19	Cl X	$(2s^2 2p^4)^3P_1 - (2s2p^5)^3P_1$	206.4	206.02		1
20	Cl X	$(2s^2 2p^4)^3P_0 - (2s2p^5)^3P_1$	207.7	207.41	207.41	1

[a]Measured wavelength corrected for first- and second-order Doppler shifts. Under optimum conditions (i.e. intense and unblended spectral features) the wavelength uncertainty is estimated at ± 0.1 Å. Weak and/or partially blended lines can only be determined to ± 0.1 Å - 0.3 Å. The instrumental bandpass employed was 0.38 Å (fwhm).

TABLE 4.2 (continued)

[b]B. C. Fawcet, Atomic Data and Nuclear Data Tables 16, 135 (1975).

[c]R. L. Kelly and L. J. Palumbo, Naval Research Laboratory Report NRL 7599 (Washington, DC, 1973).

[d]Note that this scale is only relative since the efficiency of the apparatus varies with wavelength.

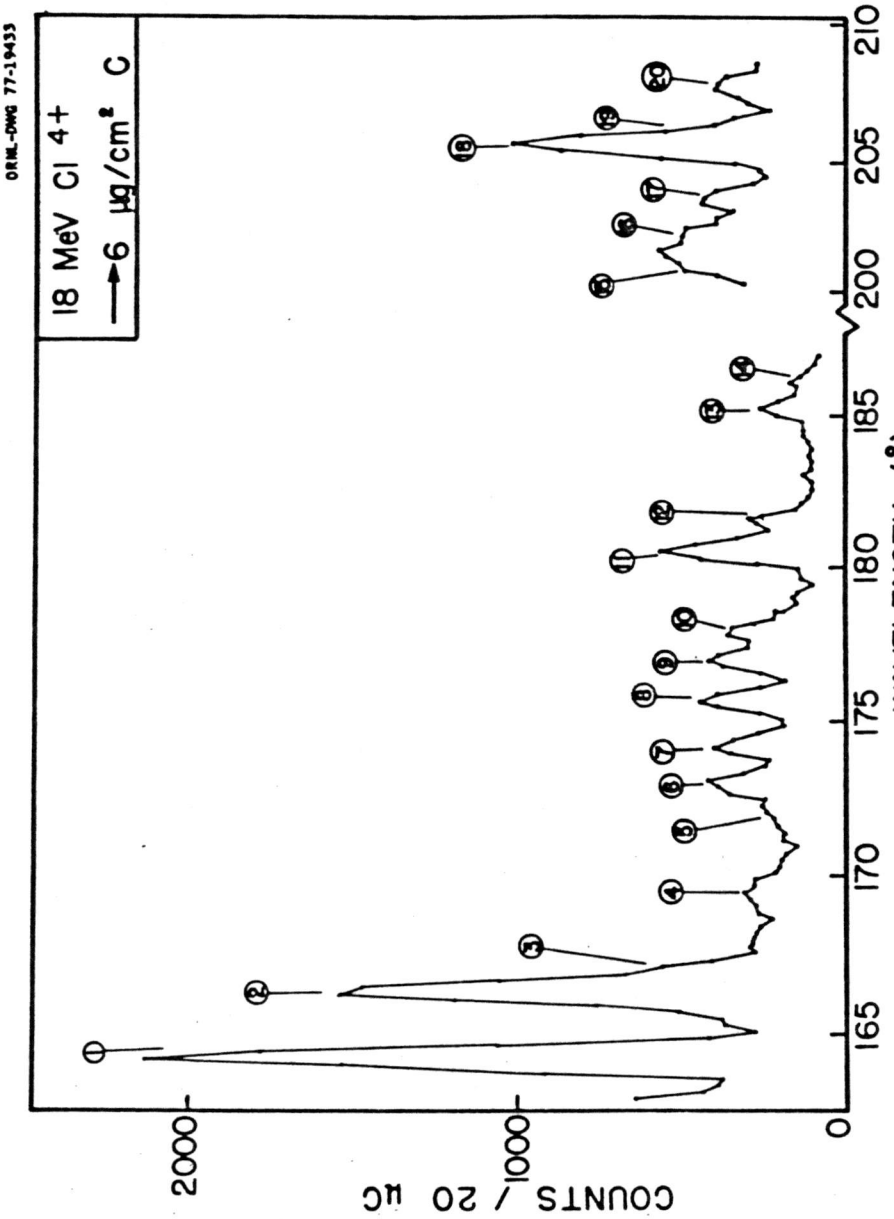


Figure 4.4. Spectrum of foil-excited chlorine ions ($160 \leq \lambda \leq 210$ Å) taken at an incident beam energy of 18 MeV. See Table 4.2 for identification.

procedure discussed earlier in the text. Wavelengths determined in the present experiment are compared to values cited in the tables of Fawcett[8] and Kelly and Palumbo.[9]

The line intensities quoted in the tables are only relative measurements using the 199.3 Å and the 164.5 Å lines as the reference lines in Tables 4.1 and 4.2 respectively. Measurements of absolute line intensities are difficult with the present apparatus because the efficiency of the spectrometer as a function of wavelength is not known. Spectral scans were also made on each individual line whose decay properties were to be studied. These scans determined the position of the line centroid so that one could accurately set the spectrometer in order to isolate the transition for the lifetime measurements. There are two previously unreported prominent lines listed in Table 4.1, the 215.5 Å and 271.2 Å lines which appear to be associated with the $(1s^2 2s2p^5)^1P_1^o - (1s^2 2p^6)^1S_0$ and the $(1s^2 2s2p^3)^1D_1^o - (1s^2 2p^4)^1D_2$ transitions in Cl X and Cl XII respectively. In addition a previously unreported feature at 331.9 Å seems to be associated with the $(1s^2 2s2p^3)^1P_1^o - (1s^2 2p^4)^1D_2$ transition in Cl XII. These assignments were made by extrapolating known transition energies along isoelectronic sequences. Observations of the variation of line intensities as a function of beam energy helped to confirm these tentative assignments.

---

[8] B. C. Fawcett, Atomic Data and Nuclear Data Tables 16, 135 (1975).

[9] R. L. Kelly, L. J. Palumbo, Atomic and Ionic Emission Lines Below 2000 Å, NRL Report 7599, Naval Research Lab, Washington, D. C.

LIFETIMES

The beam-foil excitation technique has been used to obtain the radiative lifetimes of many levels in multiply-charged chlorine ions. The charge states studied in the present work varied from 14+ to 8+. The charge distribution in a post-foil source is dependent upon the incident beam energy. In this work the energy of the beam from the ORNL tandem accelerator was chosen to optimize (as closely as was convenient) the charge state of interest in a particular measurement. Table 4.3 summarizes the beam energy parameters employed in the present work. Corrections to the energy of the beam ions emerging from the foil due to energy loss suffered in the foil are taken from the tables of Northcliffe and Schilling.[10]

The background-corrected decay data was fitted to one, two, or, in a few cases, three exponentials using a non-linear least squares computer program named DESCALC.[11] In addition, some of the multiexponential curves were also fitted using another program named HOMER.[12] In all the computer fits attempted, data points were omitted sequentialy from the beginning of the decay curves until the fitted decay lengths of the primary component approached a saturated value. This procedure eliminated possible distortions of the fit to the primary components by faster decaying components in the curve.

---

[10] L. C. Northcliffe and R. F. Schilling: Nuclear Data Tables A1, No. 3-4, Academic Press, New York, 1970.

[11] D. Larson, Private communication.

[12] D. Irwin and A. Livingston, Computer Physics Comm. 7, 95 (1974).

TABLE 4.3

ION BEAM PARAMETERS ENCOUNTERED

Charge State Studied	Incident Beam Energy Used (MeV)	Energy Correction for Energy Lost in the Foil (MeV)[a]	Typical Beam Currents[b] (namp)	% of Total Ion Flux in Charge State[c]
14+	45.501	0.117	200-500	10
13+				28
12+	38.015	0.122	200-400	27
11+				22
10+	17.966	0.123	500-600	27
9+				32
8+	8.002	0.097	700	27

[a]L. C. Northcliffe and R. F. Schilling: Nuclear Data Tables AI, No. 3-4 (Academic Press, New York, 1970).

[b]Total current as collected from the Faraday Cup.

[c]Values taken from Figure 2.1.

Survey spectra were taken at each beam energy in order to determine any potential line-blend problems. Lines within the spectra which fall within half the instrumental bandpass (base width) of the centroid of interest are considered as possible blend candidates. The instrumental bandpass (base width) in angstroms for the monochromator used in the present work is obtained by multiplying twice the reciprocal dispersion in the plane of the slit jaws (0.015 Å/ μm) by the slit width in μm (assuming a symmetric entrance-exit slit configuration). Line blending with known lines was not a serious problem in the present work. The major cause of non-single exponential decay curves was cascading i.e. repopulation of the level of interest by higher-lying levels. Cascading transitions from levels outside of the L-shell usually produce negligible contributions to the decay curve (except at distances extremely close to the foil) due to the fact that level lifetimes involving $\Delta n \neq 0$ transitions are generally much shorter than those which deexcite via $\Delta n = 0$ transtiions (as is the present case). However generally there will exist more than one excited state within the L-shell and so in-shell cascading is often a factor to consider. In-shell cascading levels also frequently have similar lifetimes to the primary level and are roughly equally populated thus compounding the problem. The highest lying level within the L-shell should be only repopulated by the negligible out-of-shell transitions. Table 4.4 is a summary of the lifetimes determined in the present experiment. Individual entries will now be discussed.

TABLE 4.4

LIFETIMES OF LOW-LYING EXCITED STATES IN MULTIPLY-CHARGED CHLORINE IONS

Ion	λ(Å)	Transition	Lifetime of Upper Level (psec)	
			Present	Theory
Cl XV	384.0	$(2s)^2S_{1/2} - (2p)^2P_{3/2}$	763 ± 38	713[a], 737[d]
	415.6	$(2s)^2S_{1/2} - (2p)^2P_{1/2}$	945 ± 47	925[a], 925[d]
Cl XIV	277.9	$(2s2p)^1P_1 - (2p^2)^1S_0$	67 ± 10	74[b], 79[e]
	458.4	$(2s2p)^1P_1 - (2p^2)^1D_2$	600 ± 60	640[b], 673[e]
	237.8	$(2s^2)^1S_0 - (2s2p)^1P_1$	150 ± 30	116[b], 121[d], 122[e]
	286.1	$(2s2p)^3P_2 - (2p^2)^3P_2$	160 ± 8	155[e]
Cl XIII	215.3	$(2s2p^2)^2D_{5/2} - (2p^3)^2P_{3/2}$	55 ± 6	55[e]
	272.9	$(2s2p^2)^2S_{1/2} - (2p^3)^2P_{3/2}$		
	419.5	$(2s2p^2)^2P_{3/2} - (2p^3)^2D_{5/2}$	121 ± 6	127[e]
	209.9	$(2s^22p)^2P_{1/2} - (2s2p^2)^2S_{1/2}$	80 ± 8	89[b], 72[c], 89[e]
	205.5	$(2s^22p)^2P_{3/2} - (2s2p^2)^2P_{1/2}$	58 ± 6	44[b], 43[c], 45[e]

TABLE 4.4 (continued)

Ion	λ (Å)	Transition	Lifetime of Upper Level (psec) Present	Theory
Cl XIII	264.6	$(2s^2 2p)^2P_{1/2} - (2s2p^2)^2D_{3/2}$	325 ± 33	344[b], 321[c], 351[e]
	224.6	$(2s2p^2)^4P_{3/2} - (2p^3)^4S_{3/2}$	53 ± 5	46[c], 50[e]
Cl XII	197.5	$(2s2p^3)^3D_1 - (2p^4)^3P_1$	35 ± 4	35[e]
	197.6	$(2s2p^3)^3D_2 - (2p^4)^3P_1$		
	202.5	$(2s2p^3)^3D_1 - (2p^4)^3P_2$	33 ± 4	
	202.6	$(2s2p^3)^3D_3 - (2p^4)^3P_2$		
	174.4	$(2s^2 2p^2)^3P_1 - (2s2p^3)^3S_1$	27 ± 5	20[b], 21[e]
	223.2	$(2s^2 2p^2)^3P_1 - (2s2p^3)^3P_0$	132 ± 7	119[b], 123[e]
	223.1	$(2s^2 2p^2)^3P_1 - (2s2p^3)^3P_1$		
	262.4	$(2s^2 2p^2)^3P_1 - (2s2p^3)^3D_2$	318 ± 6	320[b], 303[e]
	262.2	$(2s^2 2p^2)^3P_1 - (2s2p^3)^3D_1$		
	271.2	$(2s2p^3)^1D_2 - (2p^4)^1D_2$	51 ± 5	66[e]

TABLE 4.4 (continued)

Ion	λ(Å)	Transition	Lifetime of Upper Level (psec) Present	Theory
Cl XII	175.8	$(2s^2 2p^2)^1D_2 - (2s2p^3)^1P_1$	28 ± 3	27[e]
	199.3	$(2s^2 2p^2)^1D_2 - (2s2p^3)^1D_2$	70 ± 4	70[b], 41[e]
Cl XI	195.6	$(2s2p^4)^2D_{5/2} - (2p^5)^2P_{3/2}$	26 ± 5	26[e]
	192.1	$(2s^2 2p^3)^2P_{3/2} - (2s2p^4)^2S_{1/2}$	40 ± 4	37[b], 37[e]
	166.1	$(2s^2 2p^3)^2D_{3/2} - (2s2p^4)^2P_{3/2}$	22 ± 5	18[e]
	166.6	$(2s^2 2p^3)^2D_{5/2} - (2s2p^4)^2P_{3/2}$		
	209.9	$(2s^2 2p^3)^2D_{5/2} - (2s2p^4)^2D_{5/2}$	64 ± 6	67[e]
	209.4	$(2s^2 2p^3)^2D_{3/2} - (2s2p^4)^2D_{3/2}$		
	242.7	$(2s^2 2p^3)^4S_{3/2} - (2s2p^4)^4P_{5/2}$	177 ± 18	183[b], 173[e]
Cl X	215.5	$(2s2p^5)^1P_1 - (2p^6)^1S_0$	33 ± 7	18[e]
	164.5	$(2s^2 2p^4)^1D_2 - (2s2p^5)^1P_1$	24 ± 5	15[e]

TABLE 4.4 (continued)

Ion	(Å)	Transition	Lifetime of Upper Level (psec)	
			Present	Theory
Cl X	205.4	$(2s^2 2p^4)^3P_2 - (2s2p^5)^3P_2$	62 ± 9	55[b], 53[e]
Cl IX	180.7	$(2s^2 2p^5)^2P_{3/2} - (2s2p^6)^2S_{1/2}$	30 ± 6	26[b], 23[e]

[a]Y. K. Kim and J. P. Desclaux, Physical Review Letters 36, 139 (1976). The values listed in the table are extrapolations of the results reported by the above authors.

[b]O. Sinanoglu, Nuclear Instruments and Methods 110, 193 (1973). The values listed in the table are extrapolations of the results reported by the above author.

[c]L. J. Shamey, Journal of the Optical Society of America 61, 942 (1970). The values listed in the table are extrapolations of the results reported by the above author.

[d]L. Armstrong, W. R. Fielder, and D. L. Lin, Physical Review A14, 1114 (1970). The values listed in the table are extrapolations of the results of the above authors.

[e]U. I. Safronova, A. N. Ivanova, and V. N. Kharitonova, Theoretical and Experimental Chemistry 5, 325 (1969).

Cl XV (3-electron)

A measurement has been made on both members of the principal resonance doublet (2s-2p) in the Li-like ion, Cl XV. The data were taken at a beam energy of 45.5 MeV. At this energy ~10% of the post-foil source is in the Cl^{14+} charge state. An energy level diagram of this ion is shown in Figure 4.5. The wavelengths shown are the results of the higher resolution work of Fawcett.[13]

i) The decay curve for the 384.0 Å line associated with the $(1s^2 2s)^2S_{1/2} - (1s^2 2p)^2P^o_{3/2}$ transition is shown in Figure 4.6. Analysis of this curve yielded a lifetime for the $(1s^2 2p)^2P_{3/2}$ level of 763 ± 38 psec. The decay curve is seen to be well represented by a single exponential which is to be expected since no in-shell cascading is possible and out-of-shell cascades will only contribute at very small distances from the foil due to the very short-lived upper levels. There are no other known lines which could cause blending falling within the 1.5 Å (fwhm) instrumental bandpass used in this measurement.

ii) The decay curve for the 415.6 Å line associated with the $(1s^2 2s)^2S_{1/2} - (1s^2 2p)^2P^o_{3/2}$ transition is shown in Figure 4.7. A lifetime of 945 ± 47 psec was determined for the $(1s^2 2p)^2P^o_{3/2}$ level upon analysis of the data. The single exponential nature of the decay of this level was expected because no in-shell cascading was possible in this case and no other known lines fall within the 1.5 Å (fwhm) instrumental bandpass used in this measurement.

---

[13] B. C. Fawcett, Atomic Data and Nuclear Data Tables 16, 135 (1975).

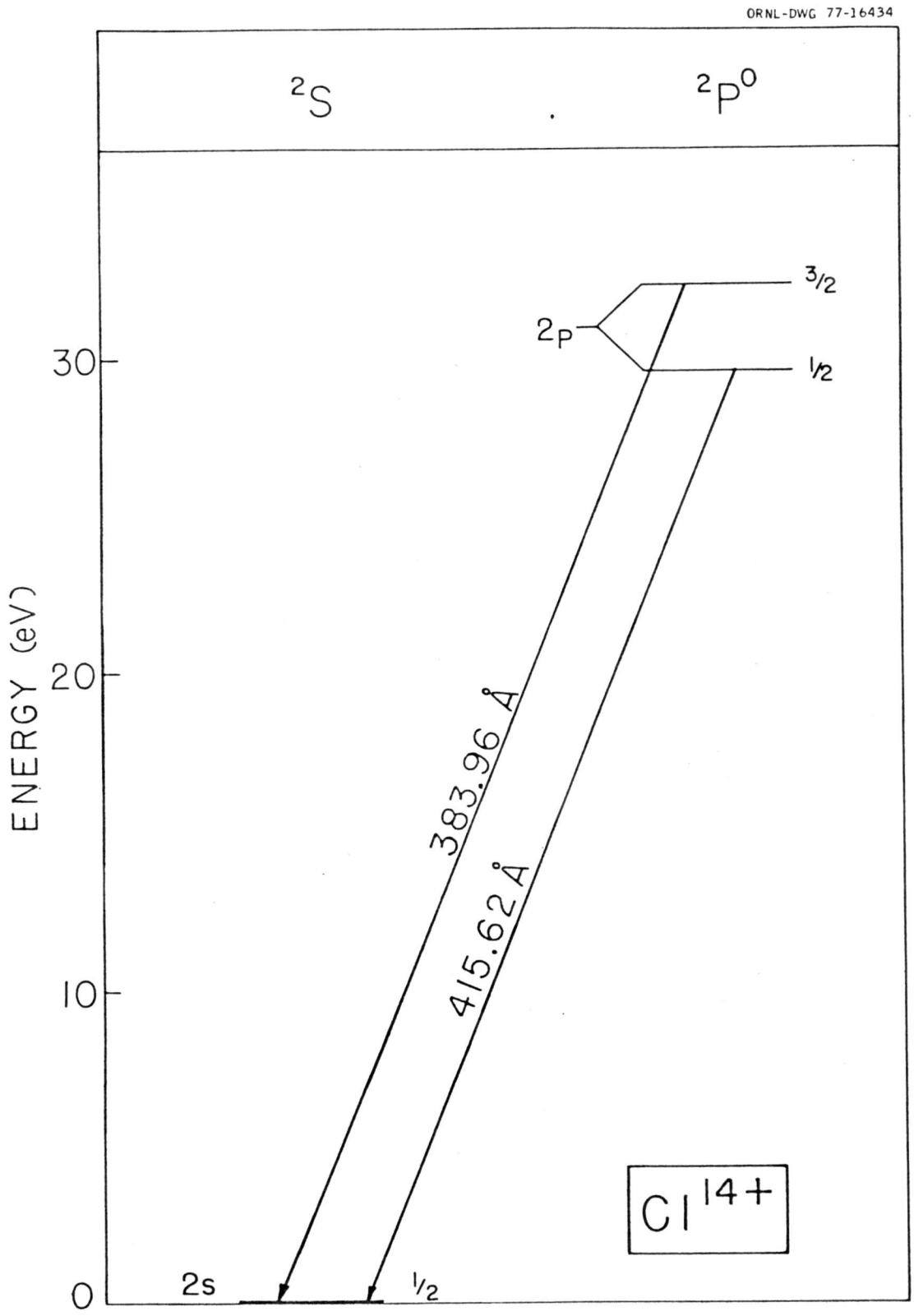


Figure 4.5. Partial energy level diagram of Li-like chlorine for $\Delta n=0$ transitions within the L-shell.

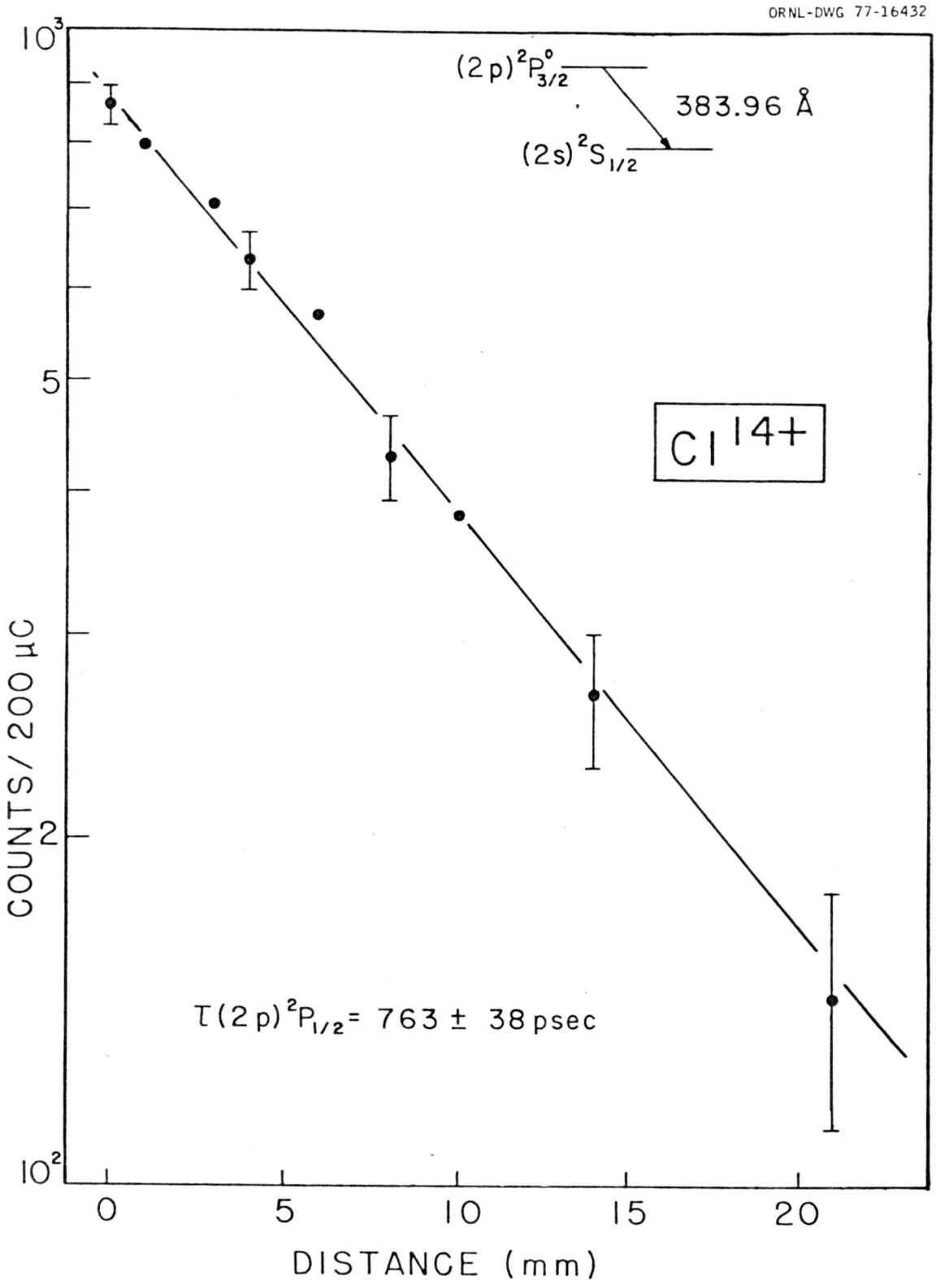


Figure 4.6. Intensity decay curve for the $(2s)^2S_{1/2} - (2p)^2P^o_{3/2}$ transition in Cl XV taken with an incident beam energy of 45.5 MeV.

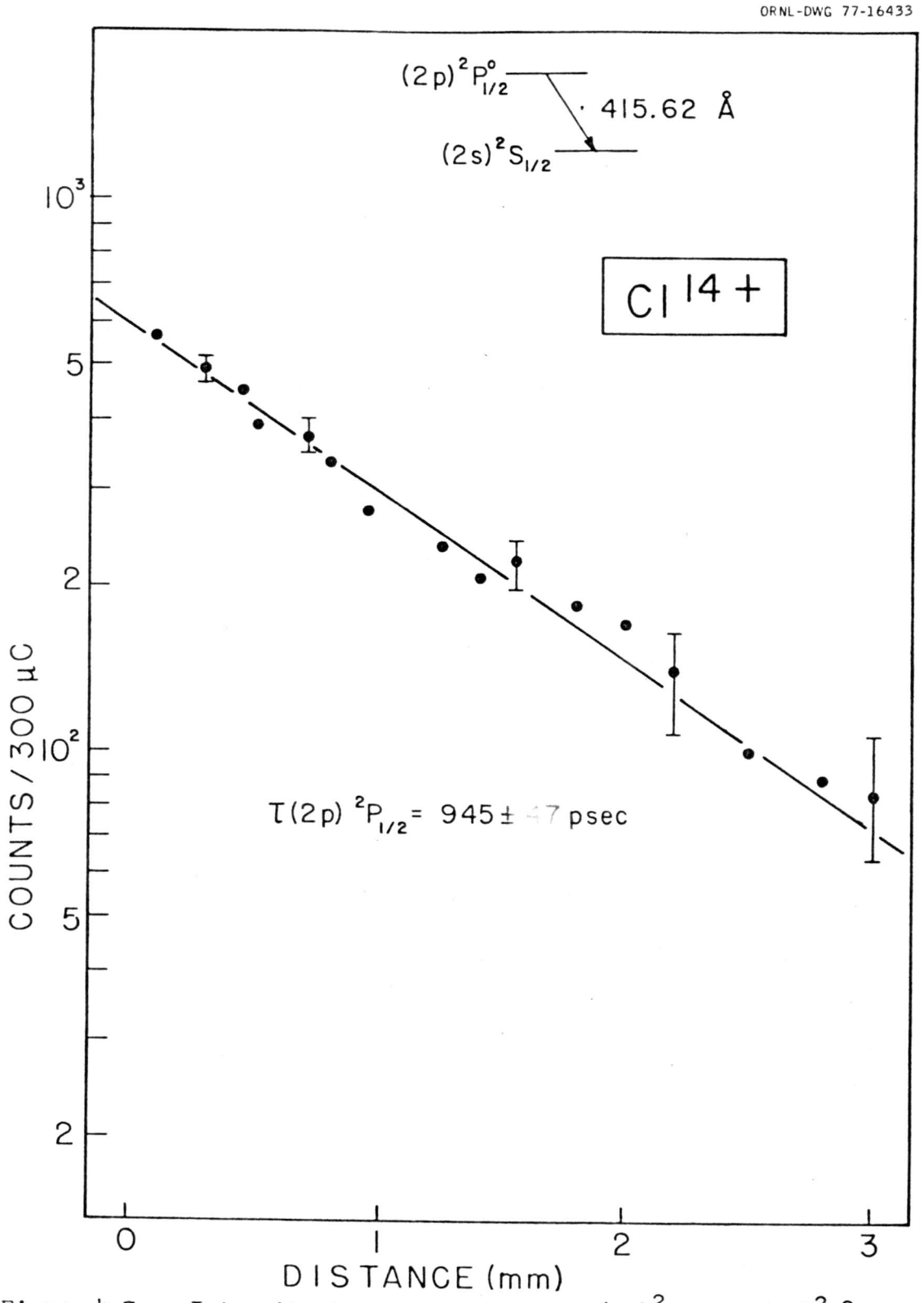


Figure 4.7. Intensity decay curve for the $(2s)^2S_{1/2} - (2p)^2P^o_{1/2}$ transition in Cl XV taken with an incident beam energy of 45.5 MeV.

Cl XIV (4-electron)

The lifetime of three singlet levels and one triplet level were measured. A beam energy of 45.5 MeV was chosen for these measurements which produced ~28% of Cl^{13+} in the post-foil source. An energy-level diagram of Cl XIV is shown in Figure 4.8. In this figure the wavelengths shown, which are multiplet averages, are derived from the higher resolution measurements of Fawcett.[14] This will also be the practice for all subsequent energy-level diagrams. The doubly-excited $(1s^2 2p^2)\,^1S_0$ and $(1s^2 2p^2)\,^1D_2$ levels are major cascade contributors to the $(1s^2 2s2p)\,^1P^o_1$ level.

i) Analysis of the decay curve associated with the $(1s^2 2s2p)\,^1P^o_1$ - $(1s^2 2p^2)\,^1S_0$ transition yielded a lifetime of 67 ± 10 psec for the $(1s^2 2p^2)\,^1S_0$ upper level. The decay in intensity of the 277.9 Å line was studied in this measurement. The decay curve is well represented by a single exponential in the curve-fitting procedure which is to be expected since no in-shell cascading exists and no other known lines lie within the 0.75 Å (fwhm) instrumental bandpass used.

ii) The decay curve of the 458.4 Å line associated with the $(1s^2 2s2p)\,^1P^o_1$ - $(1s^2 2p^2)\,^1D_2$ transition is shown in Figure 4.9. Analysis of this curve yielded a lifetime of 600 ± 60 psec for the $(1s^2 2p^2)\,^1D_2$ level. The decay data is best represented by a single exponential function. No other known lines fall within the 1.5 Å (fwhm) instrumental bandpass used in the measurement and in-shell cascading to the upper level is not possible in this case.

---

[14] B. C. Fawcett, Atomic Data and Nuclear Data Tables 16, 135 (1975).

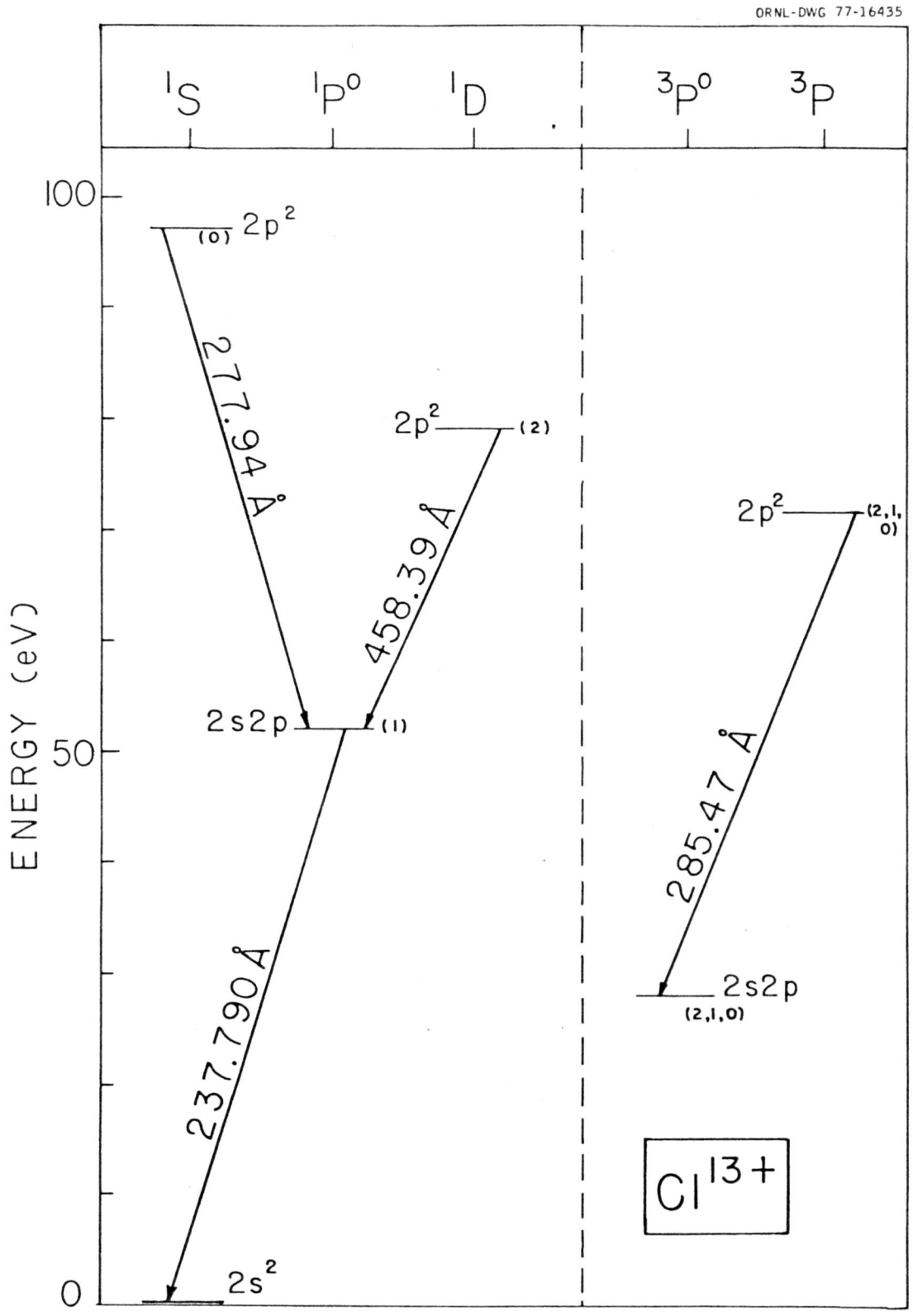


Figure 4.8. Partial energy level diagram for Cl XIV showing allowed $\Delta n=0$ transitions within the L-shell.

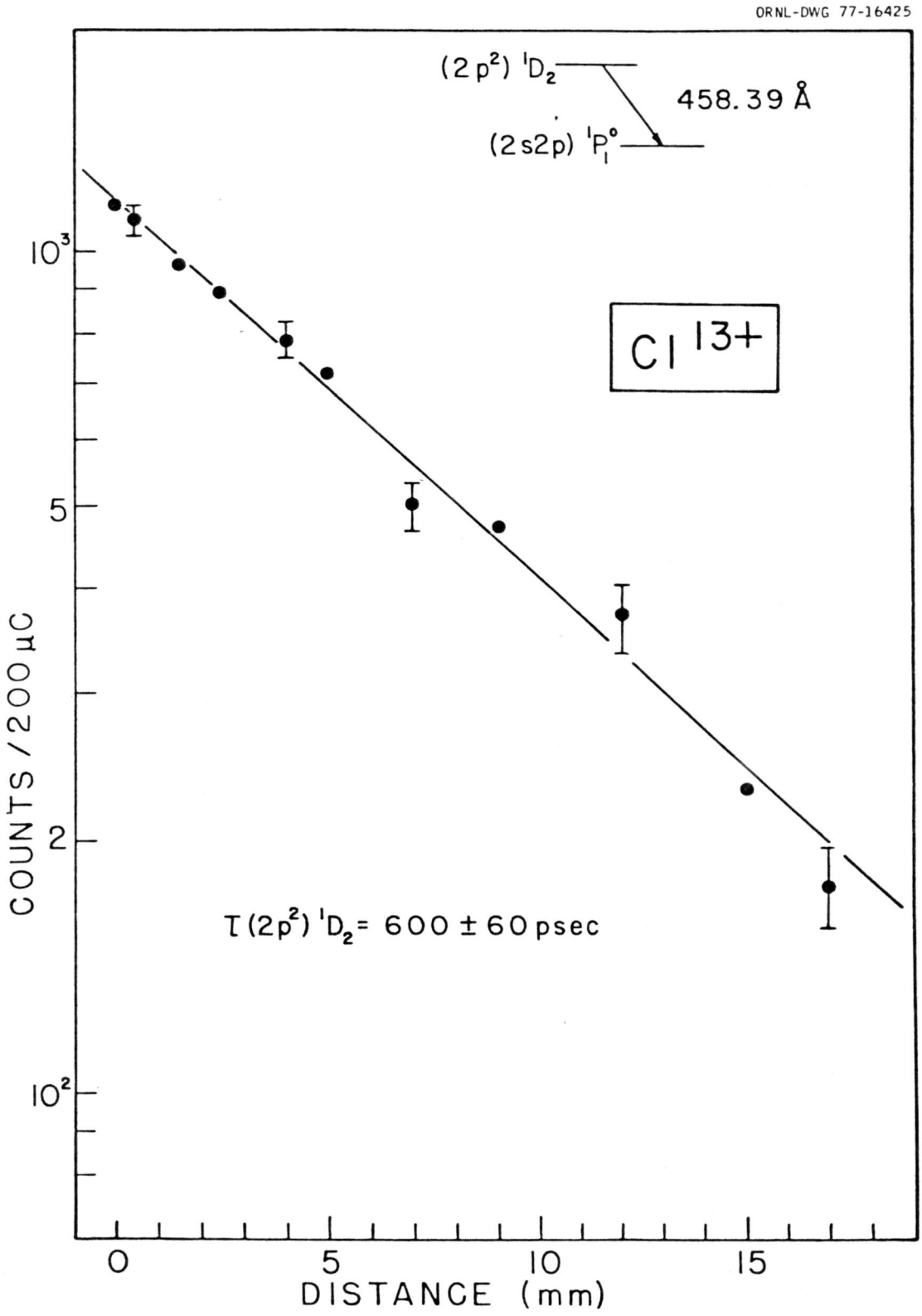


Figure 4.9. Intensity decay curve for the $(2s2p)^1P_1^o - (2p^2)^1D_2$ transition in Cl XIV taken with an incident beam energy of 45.5 MeV.

iii) The decay curve of the 237.8 Å line associated with the $(1s^2 2s^2)^1S_0$ - $(1s^2 2s2p)^1P_1^o$ transition is shown in Figure 4.10. Analysis of this curve yielded a lifetime of 150 ± 30 psec for the $(1s^2 2s2p)^1P_1^o$ level. The decay curve is seen to be adequately represented by two exponentials. These exponential components can be associated with the decay of the $(1s^2 2s2p)^1P_1^o$ level (which is the primary level being studied) and the $(1s^2 2p^2)^1D_2$ level which feeds the primary level. It appears that since the lifetime and initial population of the cascading $(1s^2 2p^2)^1S_0$ level are both comparable to that of the primary $(1s^2 2s2p)^1P_1^o$ level it is not possible to successfully measure the lifetime of either level satisfactorily. The result of this unfortunate cascade situation is that the measured decay constant of the first exponential shown in Figure 4.10 is some ~25% higher than theory predicts for the $(1s^1 2s2p)^1P_1^o$ level. The lifetime of the $(1s^2 2p^2)^1D_2$ level of 650 ± 100 psec (as extracted from the decay curve) however agrees within limits of error, with the result of 600 ± 60 psec reported above. There is no interference in this case since the lifetime is ~4 times longer than that of the primary level.

iv) The decay curve for the 286.1 Å line associated with the $(1s^2 2s2p)^3P_2^o$ - $(1s^2 2p^2)^3P_2$ transition is shown in Figure 4.11. Analysis of this curve yielded a lifetime of 160 ± 8 psec for the $(1s^2 2p^2)^3P_2$ level. The measurement was made using a beam energy of 45.5 MeV. Another measurement made at a beam energy of 38 MeV checked the velocity scaling of the experimental technique. The lifetime measurements performed at each of these two beam energies agree with each other within experimental errors. As is seen in Figure 4.11 the curve taken at an

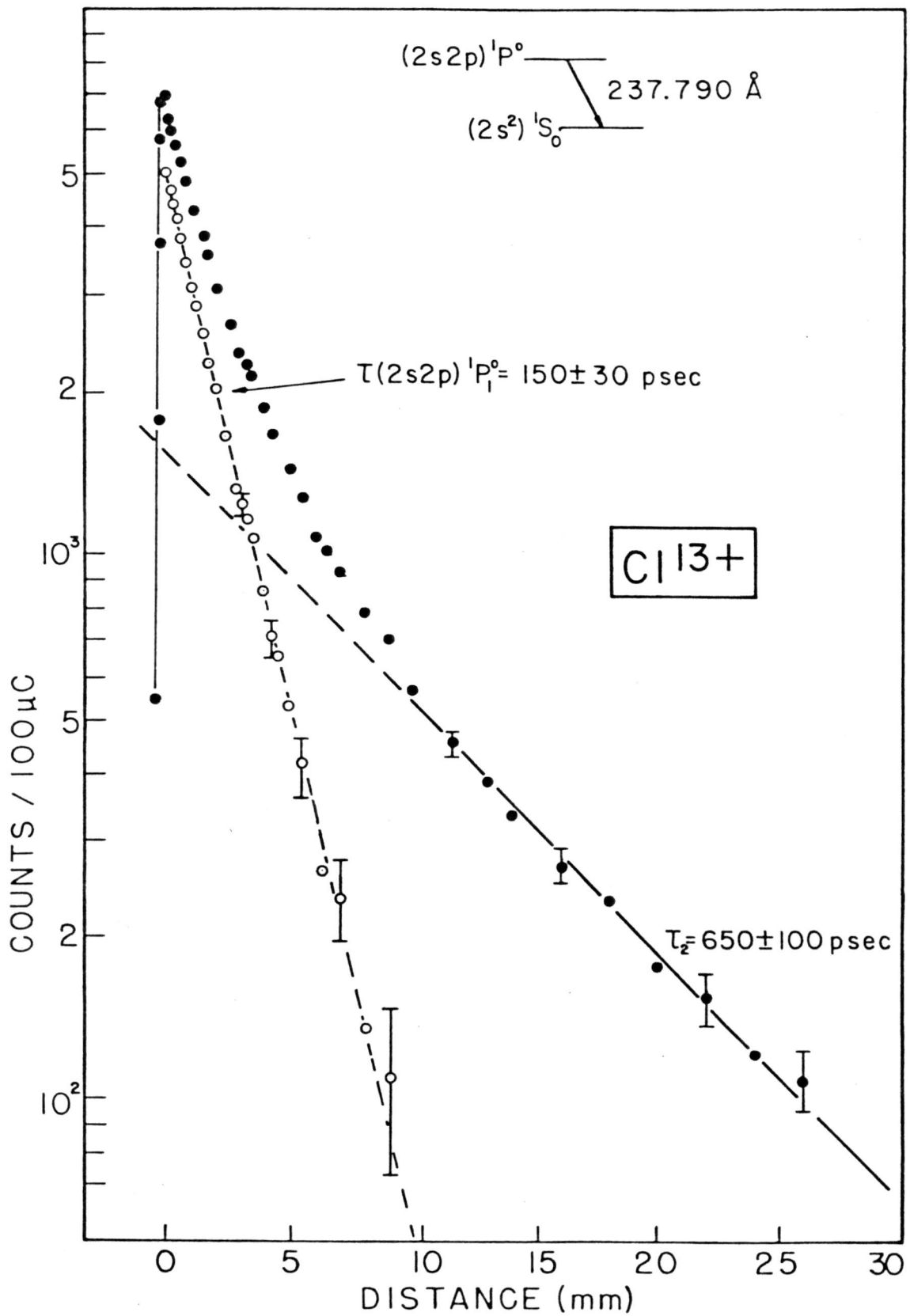


Figure 4.10. Intensity decay curve for the $(2s^2)^1S_0$ - $(2s2p)^1P_1^o$ transition in Cl XIV taken with an incident beam energy of 45.5 MeV.

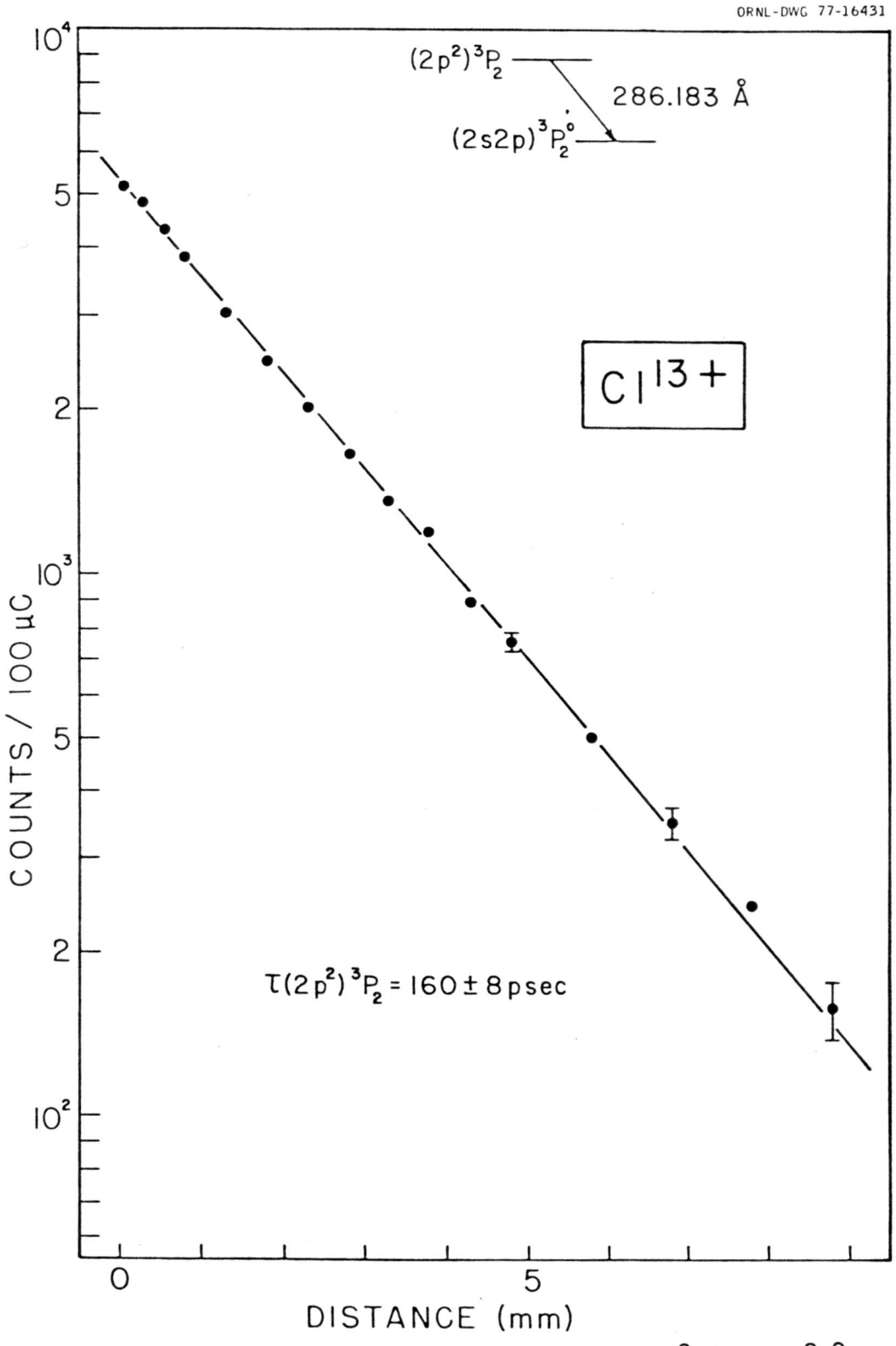


Figure 4.11. Intensity decay curve for the $(2s2p)^3P_2^o - (2p^2)^3P_2$ transition in Cl XIV taken with an incident beam energy of 45.5 MeV.

energy of 45.5 MeV is well represented by a single exponential. This was expected since no in-shell cascading is possible for this case and no other known lines fall within the 1.5 Å (fwhm) bandpass used in the measurement.

Cl XIII (5-electron)

The lifetime of five doublets and one quartet level were measured. The intensity decay measurements on these boron-like ions were performed at a beam energy of 38 MeV which produces ~27% of Cl^{12+} in the post-foil source. An energy level diagram of Cl XIII is shown in Figure 4.12. The doubly-excited $(1s^2 2p^3)^2P^o_{3/2,1/2}$ and $(1s^2 2p^3)^2D^o_{5/2,3/2}$ levels are major cascade contributors to the singly-excited levels.

i) The decay curve of the 215.3 Å line associated with a blend of lines from both the $(1s^2 2s2p^2)^2D_{5/2,3/2}$ - $(1s^2 2p^3)^2P_{3/2}$ transitions is shown in Figure 4.13. This blend is no problem since there is a common upper level. Analysis of this curve yielded a lifetime of 56 ± 6 psec for the $(1s^2 2p^3)^2P^o_{3/2}$ level. This level lifetime was also measured by studying another decay channel i.e. the $(1s^2 2s2p^2)^2S_{1/2}$ - $(1s^2 2p^3)^2P^o_{3/2}$ transition which produces a line at 272.9 Å. In this case the upper level lifetime was determined to be 53 ± 6 psec. Thus the two results agree within experimental error quoted as is to be expected. It can be seen from Figure 4.13 that the decay curve for the 215.3 Å line is best-fitted by two exponential components (the decay curve for the 272.9 Å line also had the same structure). The measured lifetime of the longer-lived exponential agrees with the theoretical prediction for the $(1s^2 2p^3)^2P^o_{3/2}$ level in Cl XIII. The origin of the shorter lived

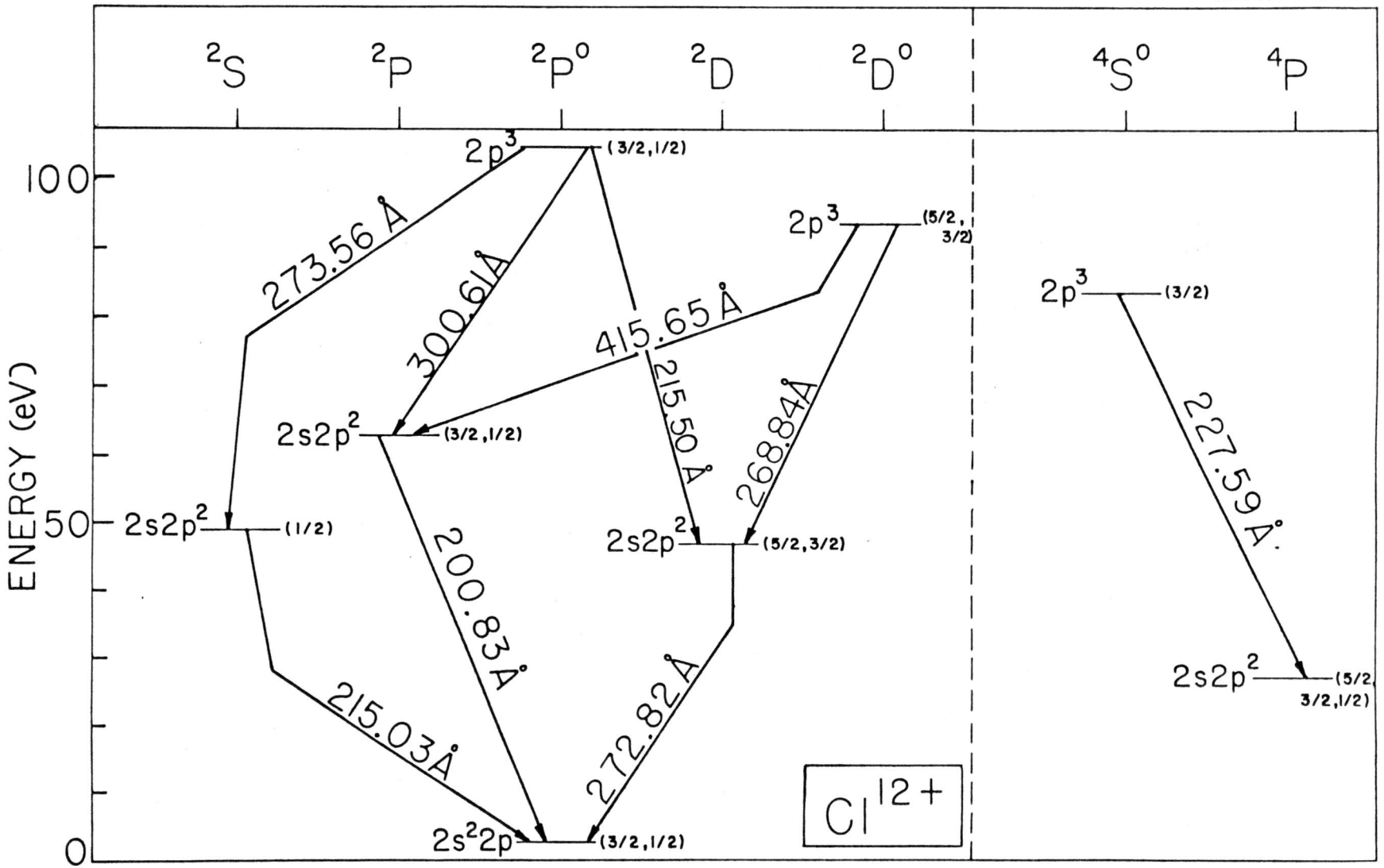


Figure 4.12. Partial energy level diagram of Cl XIII showing $\Delta n=0$ transitions within the L-shell of doublet and quartet systems. Multiplet averaged wavelengths are shown.

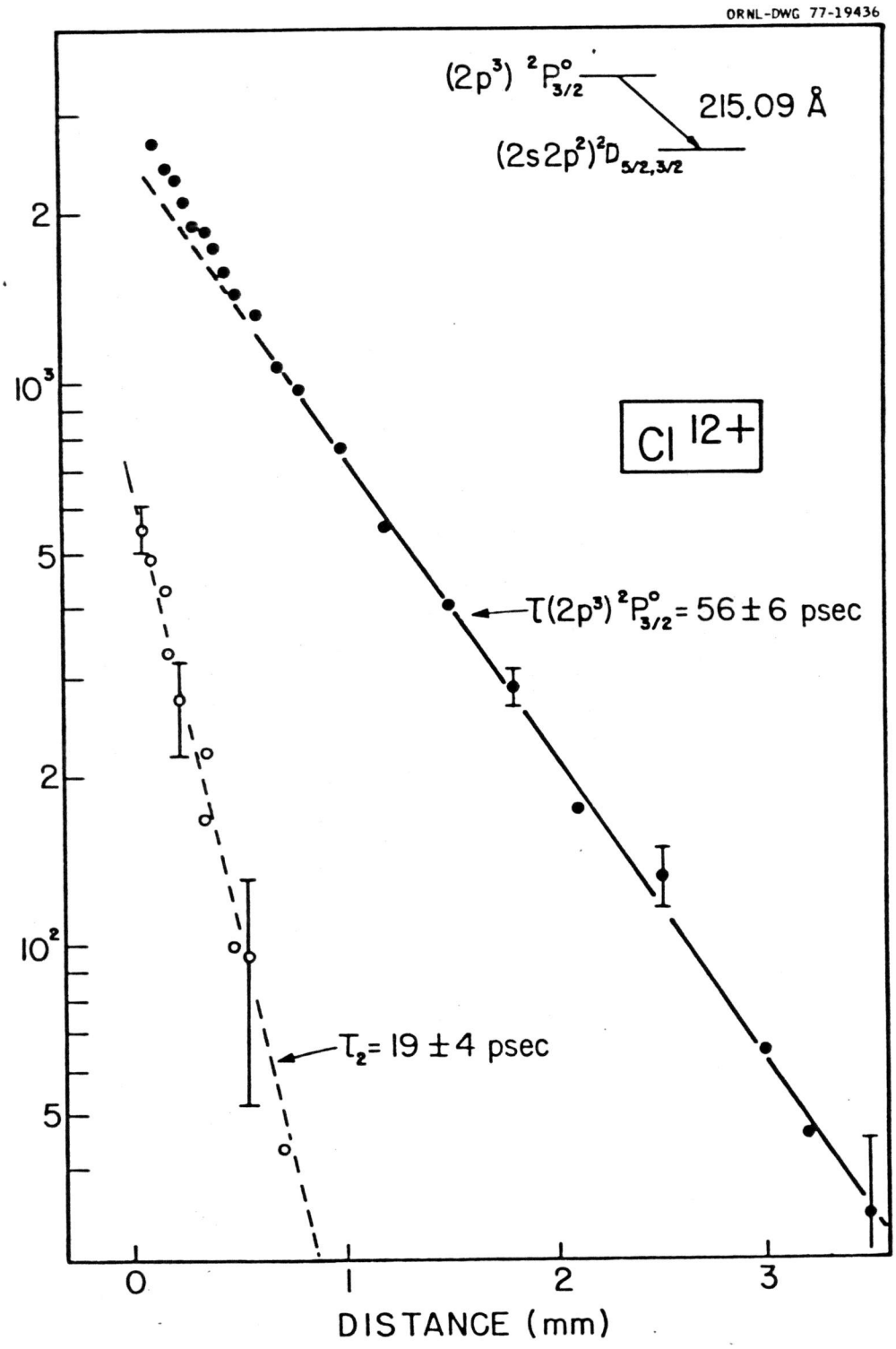


Figure 4.13. Intensity decay curve for the $(2s2p^2)^2D_{5/2,3/2}$ - $(2p^3)^2P_{3/2}$ transition in Cl XIII taken with an incident beam energy of 38 MeV.

component is not known. Cascading is eliminated since there are no possible in-shell cascade contributors and out-of-shell processes are presumably too rapid. If it were the result of a shorter-lived cascade the curve would have to exhibit the characteristic of "growing-in." It is thought that perhaps the component with a lifetime of 19 ± 4 psec shown in Figure 4.13 is due to a blend with a previously unreported line. Inspection of the spectral scan taken at 38 MeV (Figure 4.1, see page 43) shows that indeed a feature of unknown origin appears to fall on the long wavelength side of the 215.1 Å line.

ii) Analysis of the decay curve for the 419.5 Å line associated with the $(1s^2 2s 2p^2)^2P_{3/2} - (1s^2 2p^3)^2D^o_{5/2}$ transition yielded a lifetime of 120 ± 6 psec for the upper level. The curve is adequately represented by a two exponential function. In-shell cascading to the doubly-excited $(1s^2 2p^3)^2D^o_{5/2}$ level is impossible. There are no other known lines falling within the 3 Å (fwhm) instrumental bandpass used for this measurement. The origin of the shorter-lived exponential function is again probably due to an unclassified blended line.

iii) Analysis of the decay curve for the 209.9 Å line associated with the $(1s^2 2s^2 2p)^2P^o_{1/2} - (1s^2 2s 2p^2)^2S_{1/2}$ transition yields a lifetime of 80 ± 8 psec for the $(1s^2 2s 2p^2)^2S_{1/2}$ level. A weak, longer-lived cascade contribution appears in the decay curve in addition to the shorter-lived exponential representing the decay of the primary level. The only possible in-shell cascades are from the $(1s^2 2p^3)^2P_{3/2,1/2}$ which have lifetimes of ~55 psec. The weaker component in the decay curve is considerably longer lived than this and is again most probably

associated with the blending of an unclassified line. Fortunately this component has very little effect on the exponential representing the primary level.

iv) Curve-fitting analysis of the decay curve for the 205.5 Å line associated with the $(1s^2 2s^2 2p)^2P^o_{1/2}$ - $(1s^2 2s 2p^2)^2P_{1/2}$ transition yields a lifetime of 58 ± 6 psec for the $(1s^2 2s 2p^2)^2P_{1/2}$ level. The decay curve is adequately represented by two exponentials. These exponential components can be associated with the decay of the $(1s^2 2s 2p^2)^2P_{1/2}$ level (the primary level being studied) and the $(1s^2 2p^3)^2D^o_{3/2,1/2}$ levels which feed the primary level. It appears that the lifetimes and the initial populations of the cascading $(1s^2 2p^3)^2P^o_{3/2,1/2}$ levels are comparable to that of the primary $(1s^2 2s 2p^2)^2P_{1/2}$ level thus it is not possible to successfully measure (from the analysis of this curve) the lifetime of either level satisfactorily. The result of this cascade interference is that the measured decay constant of the primary level is some ~24% higher than theory predicts.

v) The decay curve of the 264.6 Å line associated with the $(1s^2 2s^2 2p)^2P^o_{1/2}$ - $(1s^2 2s 2p^2)^2D_{3/2}$ transition is shown in Figure 4.14. Analysis of the decay curve yielded a lifetime of 325 ± 33 psec for the $(1s^2 2s 2p^2)^2D_{3/2}$ level. The sum of two exponential functions were satisfactorily fitted to this data as is seen in Figure 4.14. There are no other known lines falling within the 1.5 Å (fwhm) instrumental bandpass used for this measurement. However there is a possibility of in-shell cascading from the $(1s^2 2p^3)^2P^o_{3/2,1/2}$ and $(1s^2 2p^3)^2D^o_{3/2}$ levels which have lifetimes of 55 ± 6 psec and 121 ± 12 psec respectively. The decay of the $(1s^2 2p^3)^2P^o_{3/2,1/2}$ levels are apparently too rapid to be observed

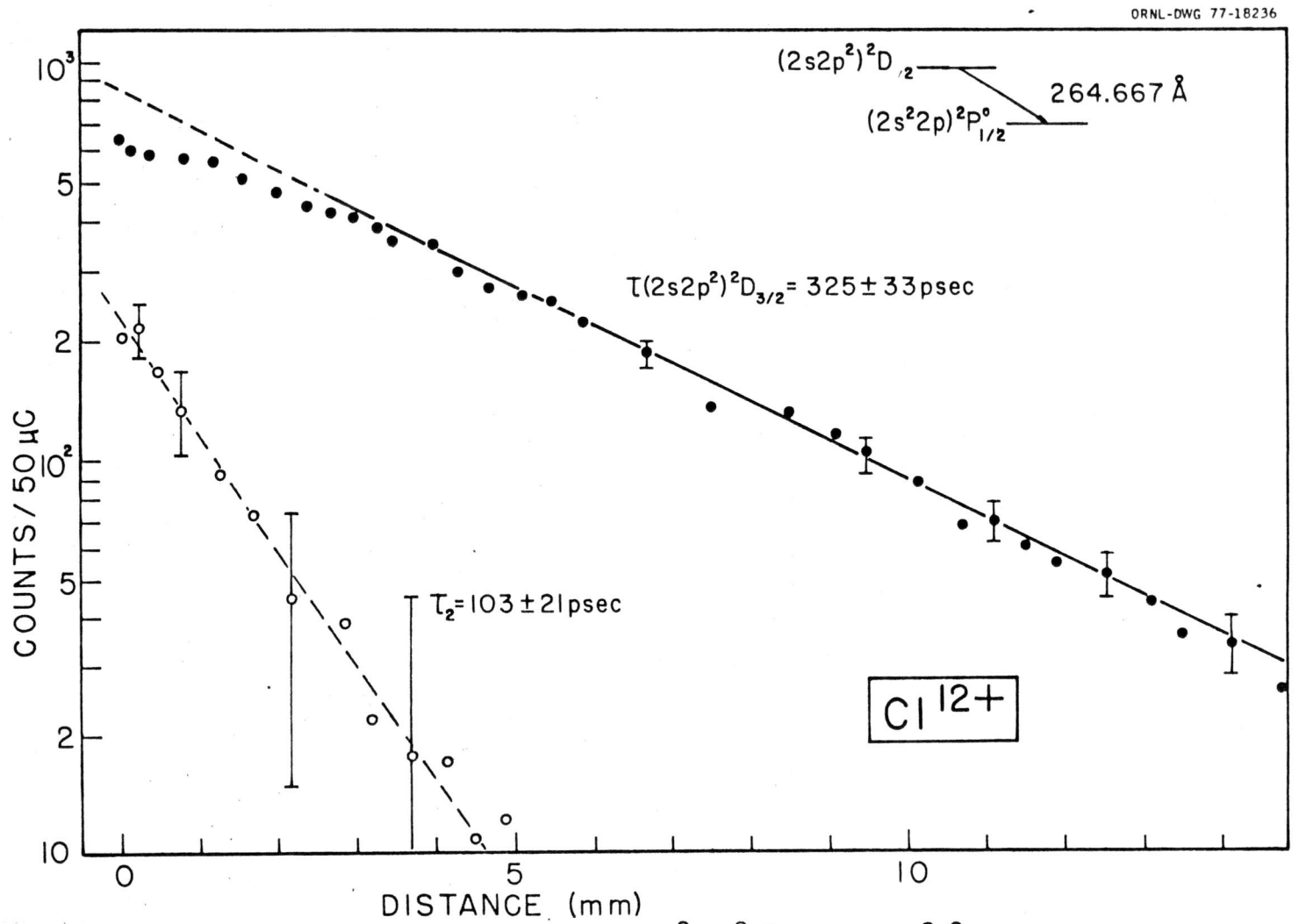


Figure 4.14. Intensity decay curve for the $(2s^22p)^2P^o_{1/2}$ - $(2s2p^2)^2D_{3/2}$ transition in Cl XIII taken with an incident beam energy of 38 MeV.

in the decay curve shown in Figure 4.14. The short-lived "growing-in" component of this decay curve (that is shown in Figure 4.14) can be associated with the decay of the $(1s^2 2p^3)\,^2D^o_{3/2}$ level. The lifetime of 103 ± 21 psec (as extracted from the decay curve) agrees, within the experimental uncertainty, with the result of 121 ± 12 psec reported above.

iv) Analysis of the curve associated with the $(1s^2 2s2p^2)\,^4P_{3/2}$ - $(1s^2 2p^3)\,^4S^o_{3/2}$ transition yielded a lifetime of 67 ± 10 psec for the $(1s^2 2p^3)\,^4S^o_{3/2}$ level. The 224.6 Å line was used in this measurement. The decay curve is adequately represented by a single exponential function in the curve-fitting procedure. Cascading due to in-shell transitions is impossible and no other known lines fall within the 1.125 Å (fwhm) instrumental bandpass used in this measurement.

Cl XII (6-electron)

A measurement has been made of the lifetime of four triplet and three singlet levels of carbon-like chlorine. A beam energy of 38 MeV was used in these measurements. At this energy ~22% of the post-foil source is in the Cl^{11+} charge state. The energy-level diagram of the triplet system of Cl XII is shown in Figure 4.15 and that of the singlet system is shown in Figure 4.16. In the triplet system, levels of the $(1s^2 2p^4)\,^3P$ term are the only in-shell cascade contributors to the levels of the three singly-excited terms: $(1s^2 2s2p^3)\,^3S^o$, $(1s^2 2s2p^3)\,^3P^o$, and $(1s^2 2s2p^3)\,^3D^o$. The spectral lines resulting from the deexcitation of levels of the two doubly-excited terms of the singlet system of Cl XII had not been previously reported in the literature. Lines falling at

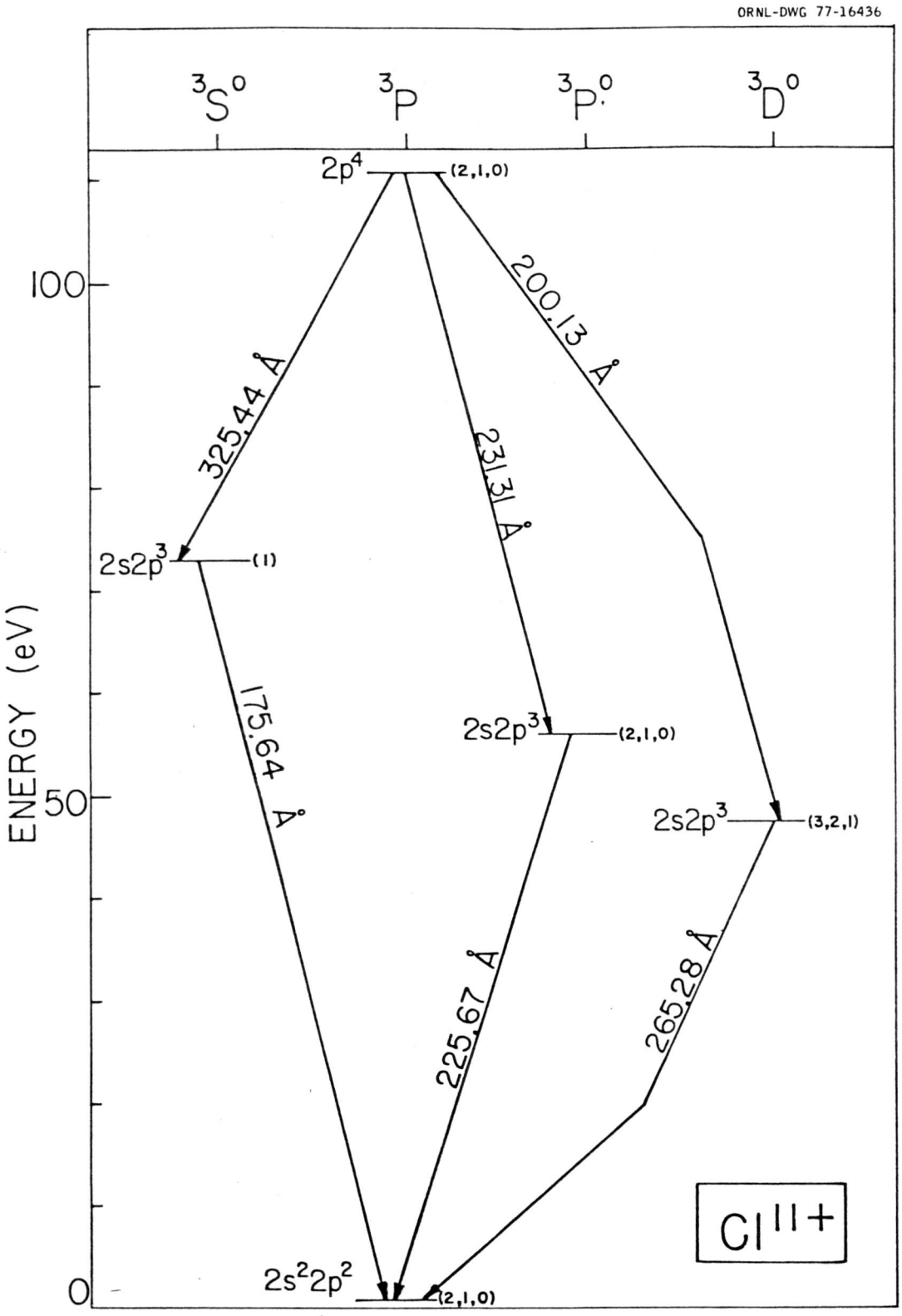


Figure 4.15. Partial energy level diagram of the triplet system of Cl XII showing $\Delta n=0$ transitions within the L-shell. The wavelengths shown are multiplet averaged.

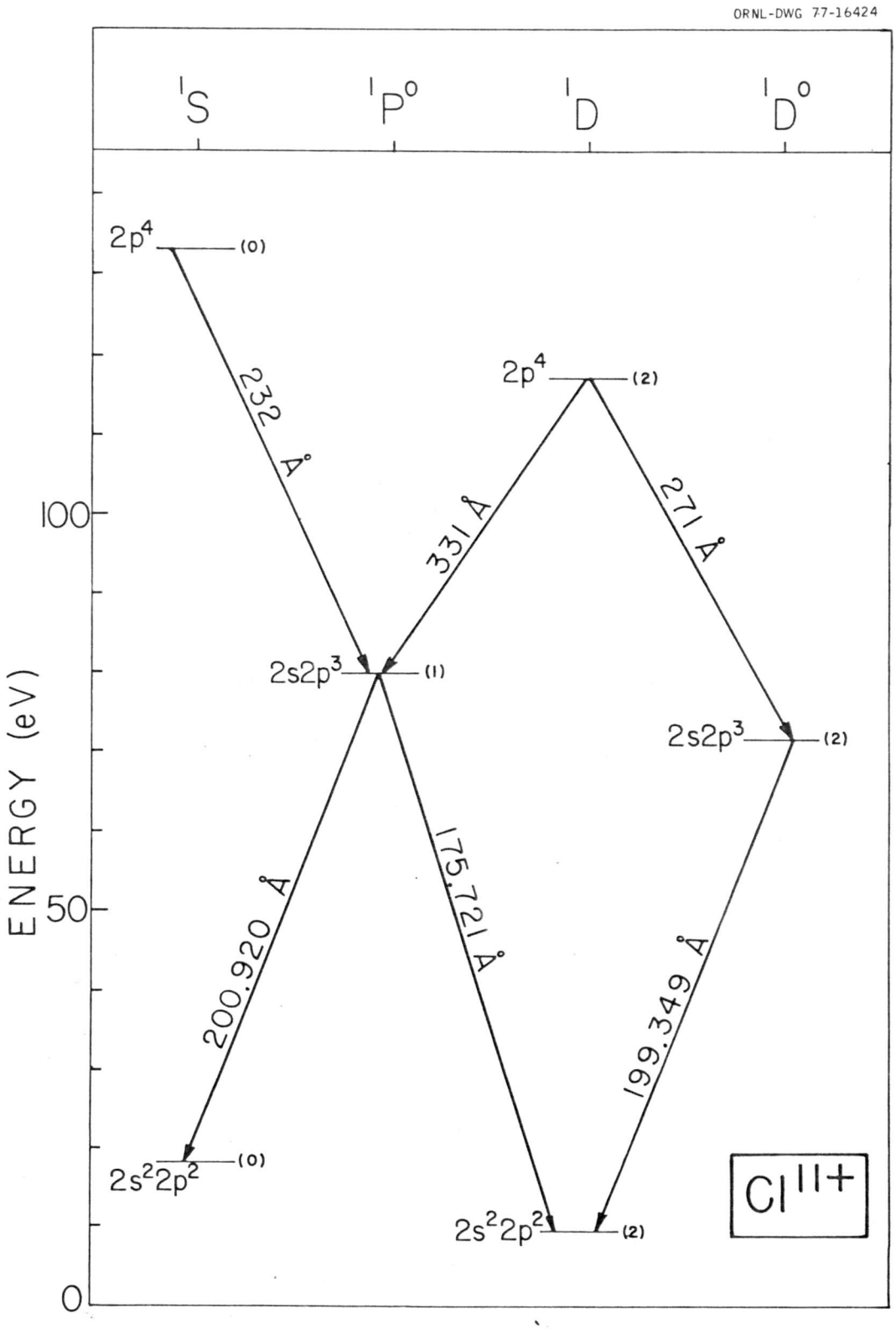


Figure 4.16. Partial energy level diagram of the singlet system of Cl XII showing $\Delta n=0$ transitions within the L-shell. The wavelengths shown are multiplet averaged.

271.2 and 331.9 Å have been tentatively assigned to the $(1s^2 2s2p^3)^1D_2^o$ - $(1s^2 2p^4)^1D_2$ and the $(1s^2 2s2p^3)^1P_1^o$ - $(1s^2 2p^4)^1D_2$ transitions respectively. The line associated with the $(1s^2 2s2p^3)^1P_1^o$ - $(1s^2 2p^4)^1S_0$ transition was not seen in the spectrum. Thus the lifetime of the $(1s^2 2p^4)^1S_0$ level could not be measured.

i) Analysis of the decay curve of the 197.6 and 197.5 Å blended lines associated with the $(1s^2 2s2p^3)^3D_{2,1}$ - $(1s^2 2p^4)^3P_1$ transitions yielded a lifetime of 35 ± 4 psec for the $(1s^2 2p^4)^3P_1$ level. The curve was adequately represented by a single exponential which was to be expected since in-shell cascading to this doubly excited level is impossible and no other known lines (other than the one cited) lie within the 1.5 Å (fwhm) instrumental bandpass used in this measurement. A measurement of the lifetime of the J=2 level of this same term was made by studying a blend of the $(1s^2 2s2p^3)^3D_{3,2}^o$ - $(1s^2 2p^4)^3P_2$ transitions which produce a feature at 202.6 Å. Analysis of this curve yielded a lifetime of 33 ± 4 psec for the $(1s^2 2p^4)^3P_2$ level thus agreeing with the result for the J=1 level within experimental error. This curve was adequately represented by two exponentials with the secondary component associated with the 202.1 Å line of B-like chlorine which falls within the 1.5 Å (fwhm) instrumental bandpass used in this measurement.

ii) Analysis of the decay curve of the 174.4 Å line associated with the $(1s^2 2s^2 2p^2)^3P_1$ - $(1s^2 2s2p^3)^3S_1^o$ transition yielded a lifetime of 27 ± 5 psec for the $(1s^2 2s2p^3)^3S_1^o$ level. The decay curve is best represented by two exponentials. The exponential components can be associated with the decay of the $(1s^2 2s2p^3)^3S_1^o$ level (which is the primary level being studied) and the $(1s^2 2p^4)^3P_{2,1,0}$ levels which feed

the primary level. Since the lifetimes and initial populations of the cascading $(1s^2 2p^4)^3P_{2,1,0}$ levels are roughly comparable to that of the primary level, the two components cannot be separated at the present level of counting statistics. It is for this reason that the quoted uncertainty in the measured lifetime is large ($\sim \pm$ 23%). No other known lines lie within the 0.75 Å (fwhm) instrumental bandpass used in this measurement.

iii) The decay curve of the 223.2 Å blend of lines associated with the $(1s^2 2s^2 2p^2)^3P_1$ - $(1s^2 2s2p^3)^3P^o_{1,0}$ transitions is shown in Figure 4.17. The lifetime of the $(1s^2 2s2p^3)^3P^o_{1,0}$ levels were found to be 132 $\pm$ 7 psec upon analysis of the decay curve. As can be seen in Figure 4.17 the curve is best fit by a single exponential function. No other known lines lie within the 1.125 Å (fwhm) instrumental bandpass used in this measurement. There is expected cascading from the $(1s^2 2p^4)^3P_{2,1,0}$ levels which should procuce a "growing-in" component on the decay curve since the lifetime of this level ($\tau \sim 35$ psec) is considerably shorter than that of the primary level being studied. This component was not however seen in the curve shown in Figure 4.17.

iv) The decay curve of the 262.4 Å blend of lines associated with the $(1s^2 2s^2 2p^2)^3P_1$ - $(1s^2 2s2p^3)^3D^o_{2,1}$ transitions is shown in Figure 4.18. The lifetime of the $(1s^2 2s2p^3)^3D^o_{2,1}$ levels were found to be 318 $\pm$ 16 psec upon analysis of the decay curve. The curve is seen to be well represented by a single exponential. No other known lines fall within the 1.5 Å (fwhm) instrumental bandpass used in this measurement. However, cascading to the levels of the primary term being studied from the

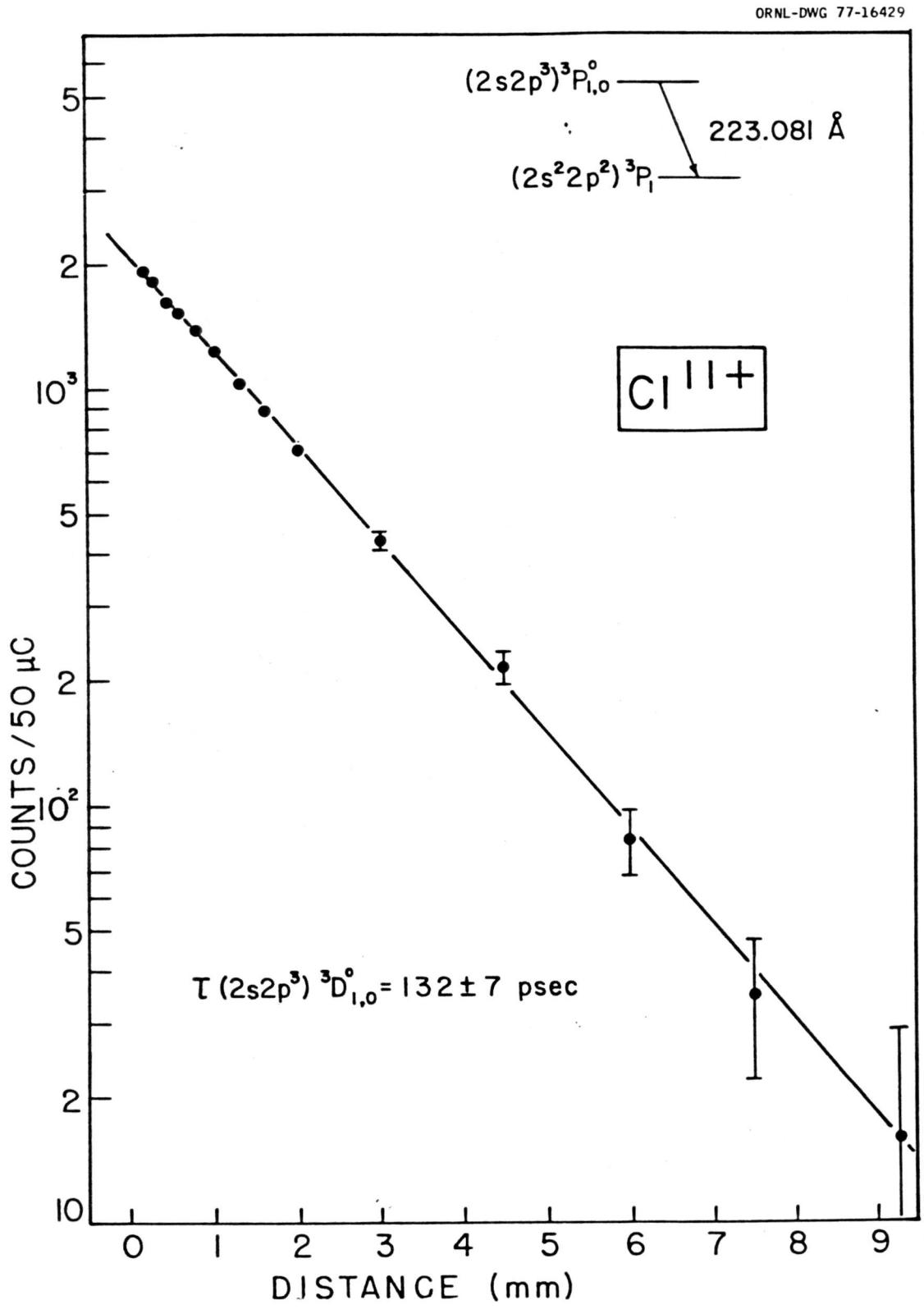


Figure 4.17. Intensity decay curve for the $(2s^22p^2)^3P_1 - (2s2p^3)^3P^o_{1,0}$ transition in Cl XII taken with an incident beam energy of 38 MeV.

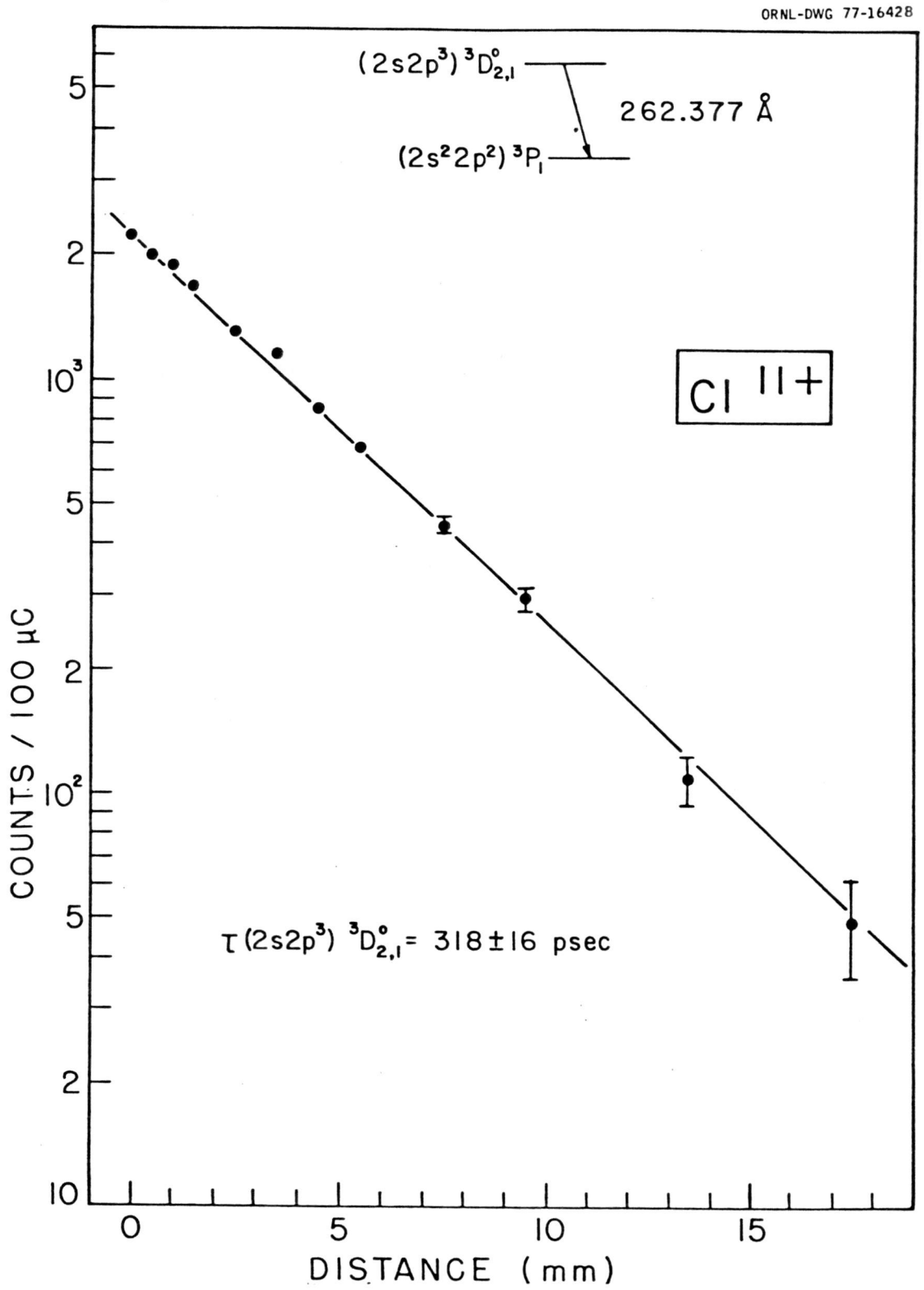


Figure 4.18. Intensity decay curve for the $(2s^2 2p^2)^3P_1 - (2s2p^3)^3D^o_{2,1}$ transition in Cl XII taken with an incident beam energy of 38 MeV.

$(1s^2 2p^4)^3P_{2,1,0}$ levels is possible but the lifetimes ($\tau \sim 35$ psec) are apparently too short to be seen in this decay curve due to the relatively long time scale used.

v) Analysis of the decay curve of the newly identified 271.2 Å line, which is believed to be associated with the $(1s^2 2s2p^3)^1D_2$ - $(1s^2 2p^4)^1D_2$ level. The curve is adequately represented by two exponential functions. There are no other known lines that fall within the 1.5 Å (fwhm) instrumental bandpass used in this measurement and in-shell cascading to the doubly-excited level is impossible. Therefore the origin of the weak, long-lived component is unknown. Tentative assignment of the 271.1 Å line to the $(1s^2 2s2p^3)^1D_2^o$ - $(1s^2 2p^4)^1D_2$ transition was accomplished by the technique of extrapolation of known transition energies along the isoelectronic sequence. The changes in line intensity as a function of beam energy helped to confirm this assignment.

vi) The decay curve of the 175.8 Å line associated with the $(1s^2 2s^2 2p^2)^1D_2$ - $(1s^2 2s2p^3)^1P_1^o$ transition was analyzed to obtain the lifetime of the $(1s^2 2s2p^3)^1P_1^o$ level. A lifetime of 28 $\pm$ 6 psec was determined from the curve fitting procedure. No known lines fall within the 0.75 Å (fwhm) instrumental bandpass used in this measurement. The primary level being studied i.e. the $(1s^2 2s2p^3)^1P_1^o$ level can be fed by two upper levels: the $(1s^2 2p^4)^1S_0$ level and the $(1s^2 2p^4)^1D_2$ level. The decay curve is best represented by two exponentials with the shorter lived of the two being associated with the primary level and the longer lived with the cascading $(1s^2 2p^4)^1D_2$ level. The longer-lived component

has a lifetime of 55 psec as measured from this curve which is in agreement with the value of 51 psec obtained in an independent measurement of the lifetime of the $(1s^2 2p^4)\,^1D_2$ level. No cascade contribution from the $(1s^2 2p^4)\,^1S_0$ level was found. However if the lifetime of this doubly-excited level happens to be comparable to the lifetimes of either of the other two levels considered above then it would be virtually impossible to extract it from the decay curve.

vii) The decay curve of the 199.3 Å line associated with the $(1s^2 2s^2 2p^2)\,^1D_2 - (1s^2 2s 2p^3)\,^1D_2^o$ transition is shown in Figure 4.19. Analysis of this curve yielded a lifetime of 70 ± 4 psec for the $(1s^2 2s 2p^3)\,^1D_1^o$ level. The curve is seen to be well represented by a single exponential. No other known lines fall within the 0.75 Å (fwhm) instrumental bandpass used in this measurement. Cascading from the $(1s^2 2p^4)\,^1D_2$ level might be expected but since its lifetime ($\tau \sim 51$ psec) is not too different from that of the primary level being studied, this component would be very difficult to separate from that of the decay curve. A cascade however always produces a measured lifetime longer than the true lifetime. The present value is in good agreement with theory so it appears cascading has a negligible effect in this case.

Cl XI (7-electron)

Lifetimes of four of the doublet levels and one quartet level of nitrogen-like chlorine were measured. These measurements were performed at a beam energy of 18 MeV which provides ~27% of Cl^{10+} in the post-foil source. The energy-level diagram for Cl XI is shown in Figure 4.20. Levels of the doubly-excited $(1s^2 2p^5)\,^2P^o$ term are major cascade

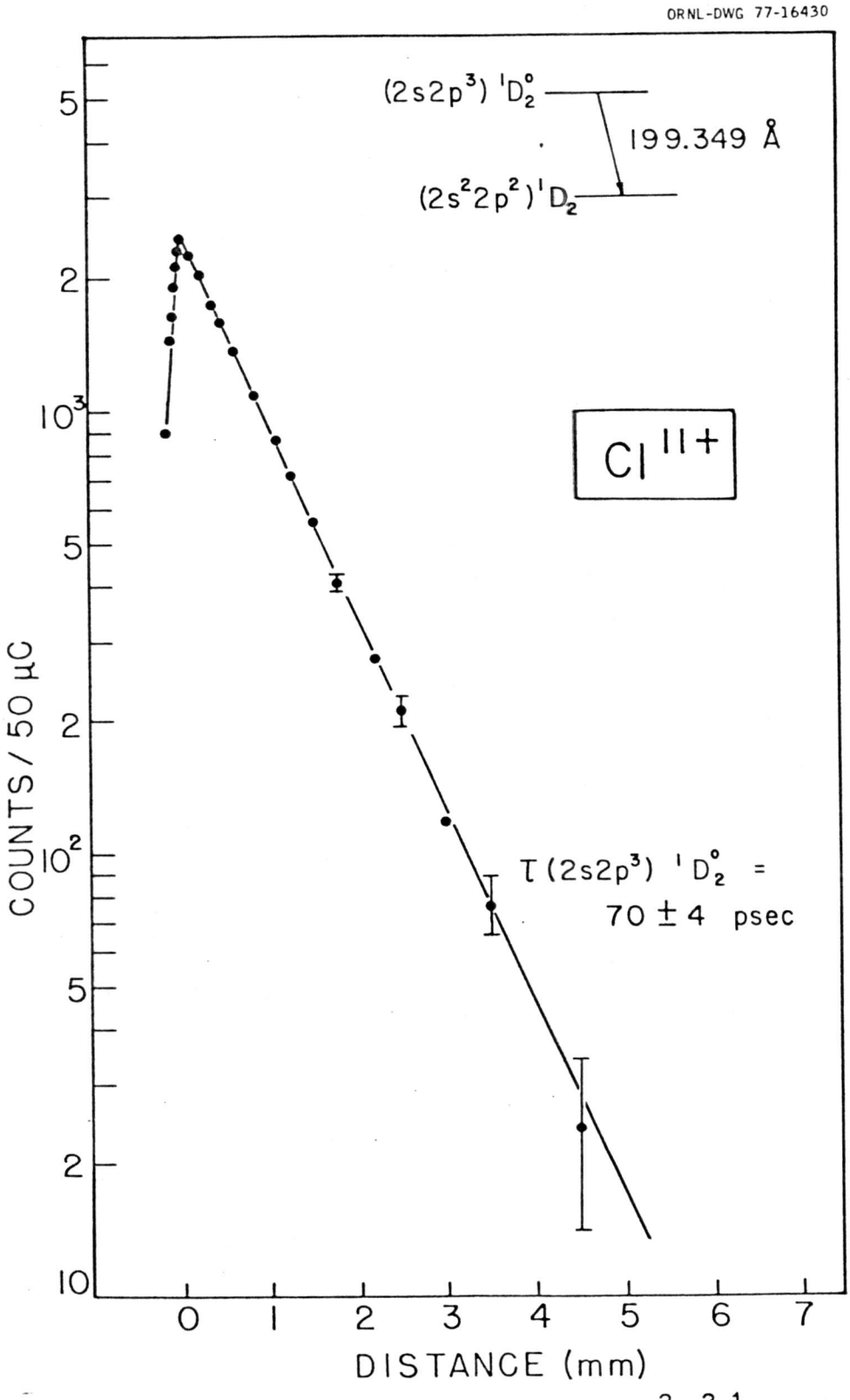


Figure 4.19. Intensity decay curve for the $(2s^2 2p^2)^1D_2 - (2s2p^3)^1D_2^o$ transition in Cl XII taken with an incident beam energy of 38 MeV.

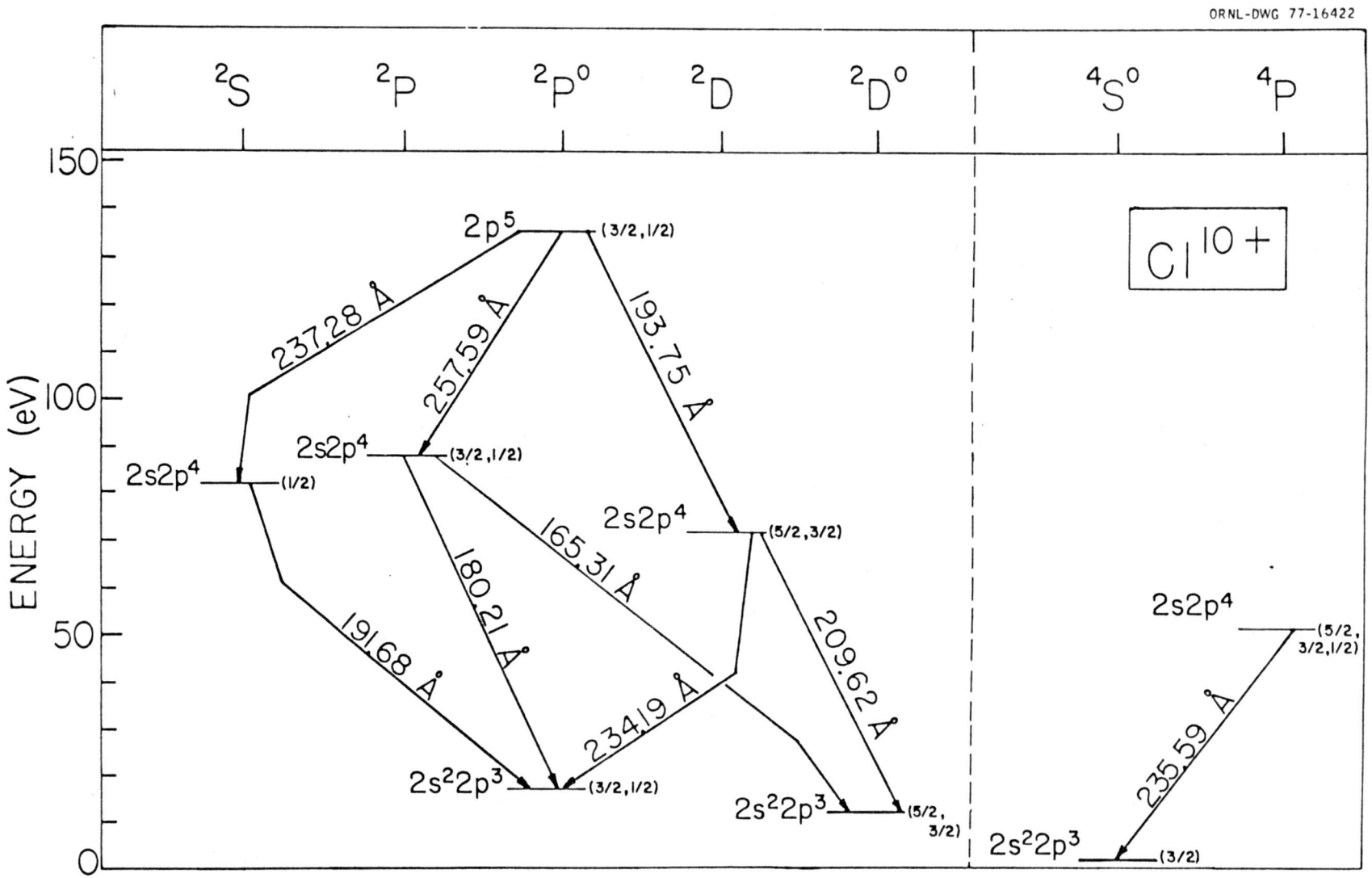


Figure 4.20. Partial energy level diagram of Cl XI showing $\Delta n=0$ transitions within the L-shell of doublet and quartet systems. Multiplet averaged wavelengths are shown.

contributors to the levels of the three singly-excited terms in the doublet system. A general feature of decay curves for N-, O-, and F-like chlorine ions is that each has a weak but long-lived component. These tails are of unknown origin. They are not thought to be associated with the data-taking techniques, e.g. normalization procedure (any problem with scattering of the beam ions at lower beam energies would have resulted in a variation of the data accumulation time and this did not occur). The components are weak enough to not appreciably affect the extraction of the decay constant of the primary exponential.

Several of the measurements reported for chlorine in this charge state approach the estimated lower limit for which lifetimes can be confidently determined with the present apparatus and procedures. The difficulty of these measurements is reflected in the somewhat larger uncertainties quoted.

i) The decay curve of the 195.6 Å line associated with the $(1s^2 2s 2p^4)^2D_{3/2} - (1s^2 2p^5)^2P^o_{3/2}$ transition is shown in Figure 4.21. Analysis of this curve yielded a lifetime of 26 $\pm$ 6 psec for the $(1s^2 2p^5)^2P^o_{3/2}$ level. There is however another line at 196.3 Å associated with the $(1s^2 2s 2p^3)^3D^o_1 - (1s^2 2p^4)^3P_0$ transition in Cl X that falls within the 1.5 Å (fwhm) instrumental bandpass used. The lifetime of the cascading $(1s^2 2p^4)^3P_0$ level ($\tau \sim 35$ psec) is comparable to that of the primary level being studied. For this reason and also since the 11^+ charge state is greatly reduced in intensity at 18 MeV ($\sim$7%), it appears that it is not possible to successfully separate these two decay components. The long-lived component of unknown origin was discussed earlier.

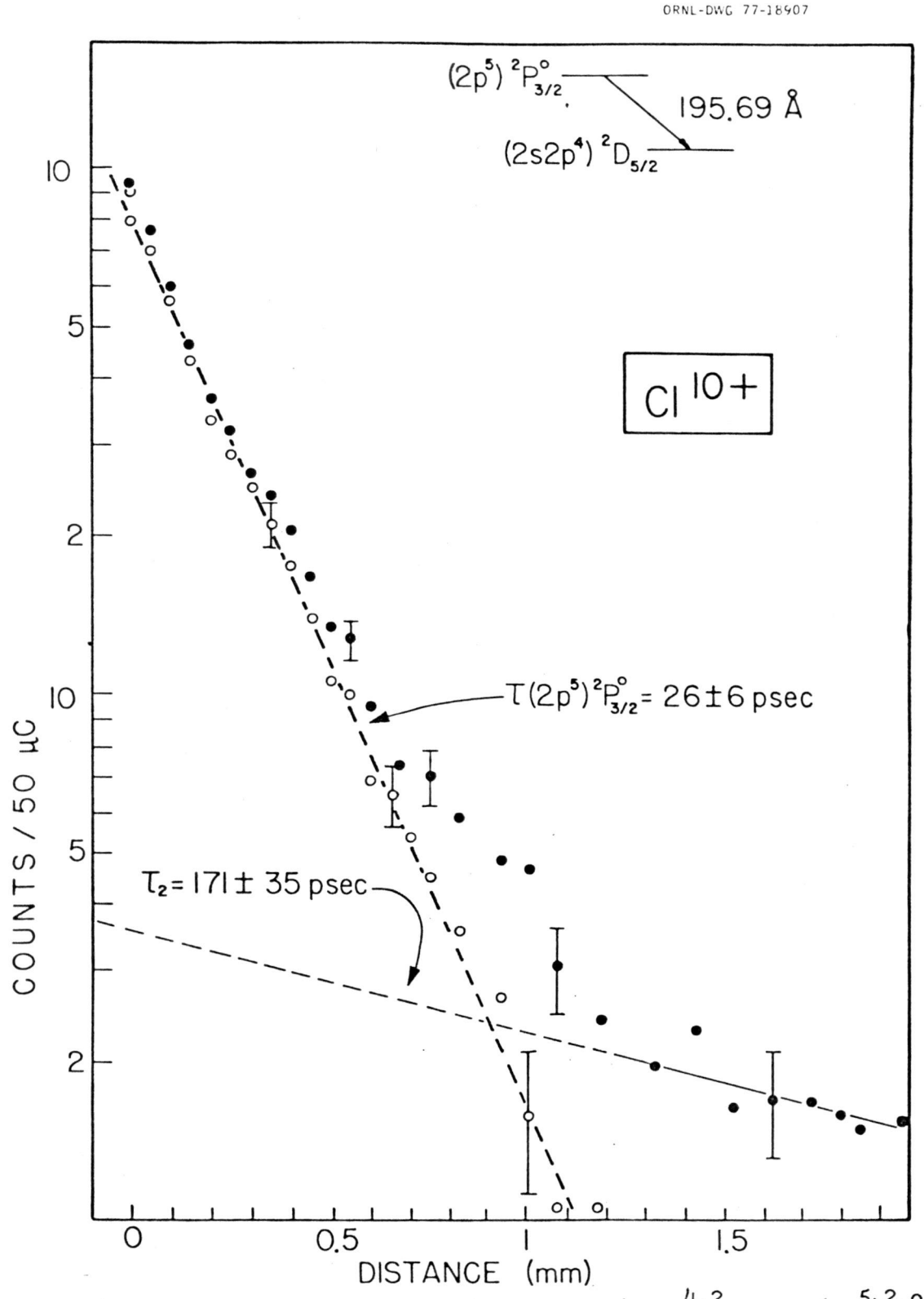


Figure 4.21. Intensity decay curve for the $(2s2p^4)^2D_{5/2}$ - $(2p^5)^2P^o_{3/2}$ transition in Cl XI taken with an incident beam energy of 18 MeV.

ii) The decay curve for the 192.1 Å line associated with the $(1s^2 2s^2 2p^3)^2 P^o_{3/2} - (1s^2 2s 2p^4)^2 S_{1/2}$ transition is shown in Figure 4.22. Analysis of the curve yielded a lifetime of 29 ± 7 psec for the $(1s^2 2s 2p^4)^2 S_{1/2}$ level. The curve is best represented by two exponential components. No other lines fall within the 1.5 Å (fwhm) instrumental bandpass used in this measurement but in-shell cascading from the $(1s^2 2p^5)^2 P^o_{3/2,1/2}$ levels are possible. Since the lifetimes of these cascading levels ($\tau \sim$ 26 psec) are comparable to that of the primary level being studied, it is impossible to successfully separate these two components in the analysis of the decay curve. As a result of this cascade problem the lifetime of the primary level, as determined by the analysis of the curve shown in Figure 4.22, may be somewhat longer than the true value. The long-lived component is of unknown origin but it has been successfully extracted from the curve.

iii) Analysis of the decay curve for the 166.6 Å blend of lines associated with the $(1s^2 2s^2 2p^3)^2 D_{5/2,3/2} - (1s^2 2s 2p^4)^2 P_{3/2}$ transitions yielded a lifetime of 22 ± 5 psec for the $(1s^2 2s 2p^4)^2 P_{3/2}$ level. This curve is adequately represented by two exponentials. No other known lines fall within the 0.75 Å (fwhm) instrumental bandpass used in this measurement. Due to the possibility of cascading from the $(1s^2 2p^5)^2 P^o_{3/2}$ levels, which have lifetimes comparable to that of the primary level being studied, the lifetime determined in the present work may be longer than the true value. Again the long lived ($\tau \sim$ 185 psec) but very weak component is of unknown origin.

iv) The decay curve for the 209.9 Å and 209.8 Å blends of lines associated with the $(1s^2 2s^2 2p^3)^2 D_{5/2,3/2} - (1s^2 2s 2p^4)^2 D_{5/2,3/2}$

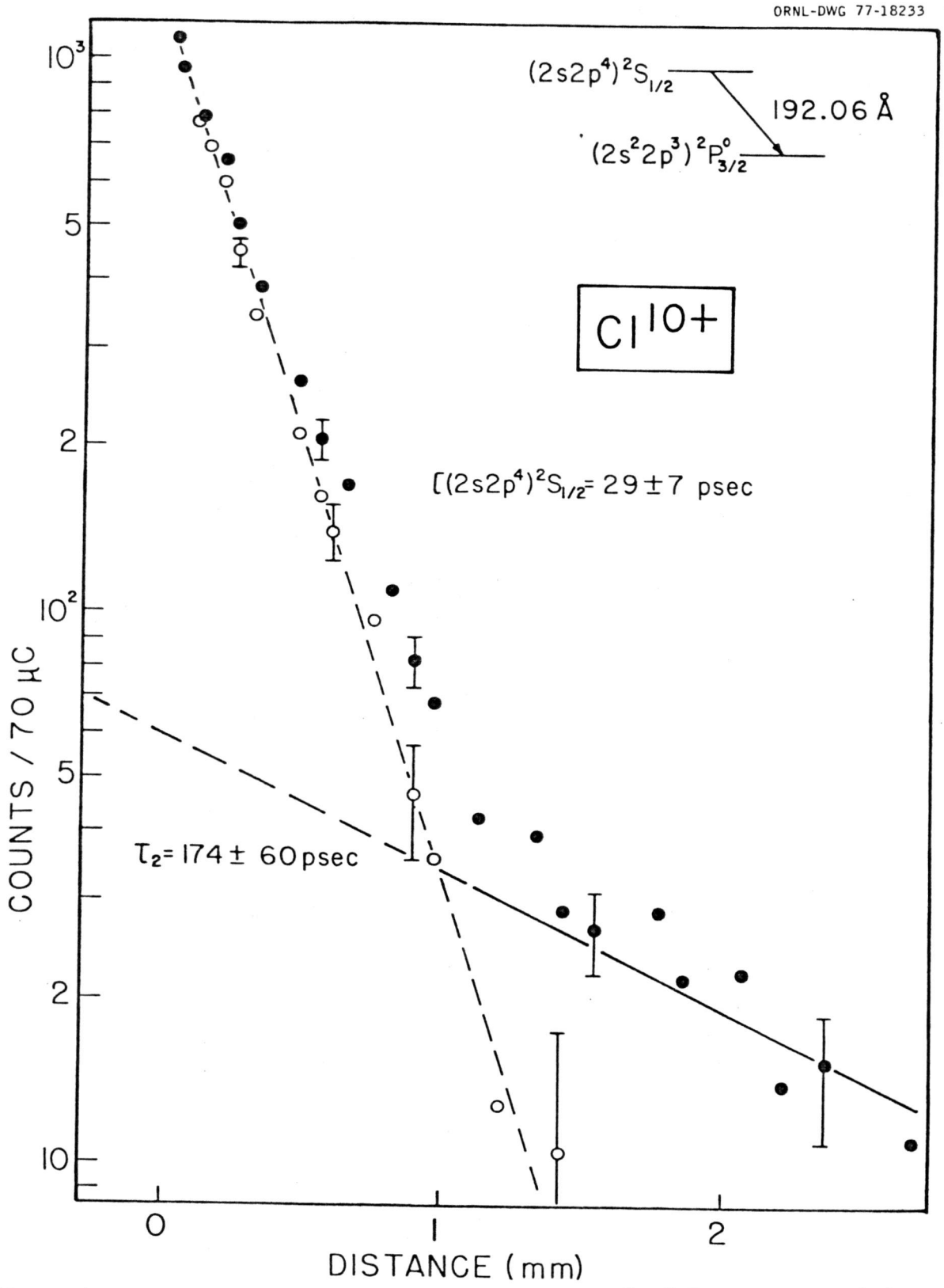


Figure 4.22. Intensity decay curve for the $(2s^22p^3)^2P^o_{3/2}$ - $(2s2p^4)^2S_{1/2}$ transition in Cl XI taken with an incident beam energy of 18 MeV.

transitions can be seen in Figure 4.23. Analysis of this curve yielded a lifetime of 64 ± 6 psec for the lifetimes of the $(1s^2 2s 2p^4)^2 D_{5/2,3/2}$ levels. No other known lines fall within the 1.5 Å (fwhm) instrumental bandpass used in this measurement. In-shell cascading is possible from the doubly-excited $(1s^2 2p^5)^2 P^o_{3/2,1/2}$ levels. Since the lifetime of the cascade ($\tau \sim 26$ psec) is shorter than that of the principal level being studied, a "growing-in" type of curve should be expected. However no such "growing-in" component was observed indicating that either the cascade decay channel from the doubly-excited levels is very weak or that the lifetimes of the two levels are so close that they can not be separated at the present level of counting statistics. A weak and long-lived ($\tau \sim 369$ psec) component can again be seen in this curve. The initial populations and decay constants of each of these long-lived tails are different for each of the transitions studied.

v) Analysis of the decay curve for the 247.2 Å line associated with the $(1s^2 2s^2 2p^3)^4 S^o_{3/2}$ - $(1s^2 2s 2p^4)^4 P_{5/2}$ transition yielded a lifetime of 177 ± 18 psec for the lifetime of the upper level. There are no other known lines falling within the 0.75 Å (fwhm) instrumental bandpass used for this measurement and in-shell cascading is not possible. The curve is adequately represented with two exponentials. The long-lived but weak component has a lifetime of 710 psec and is of unknown origin.

Cl X (8-electron)

The lifetimes of two singlet and one triplet level were measured. A beam energy of 18 MeV was used in this measurement. This beam energy resulted in ~32% of the post-foil source in the Cl^{9+} charge state.

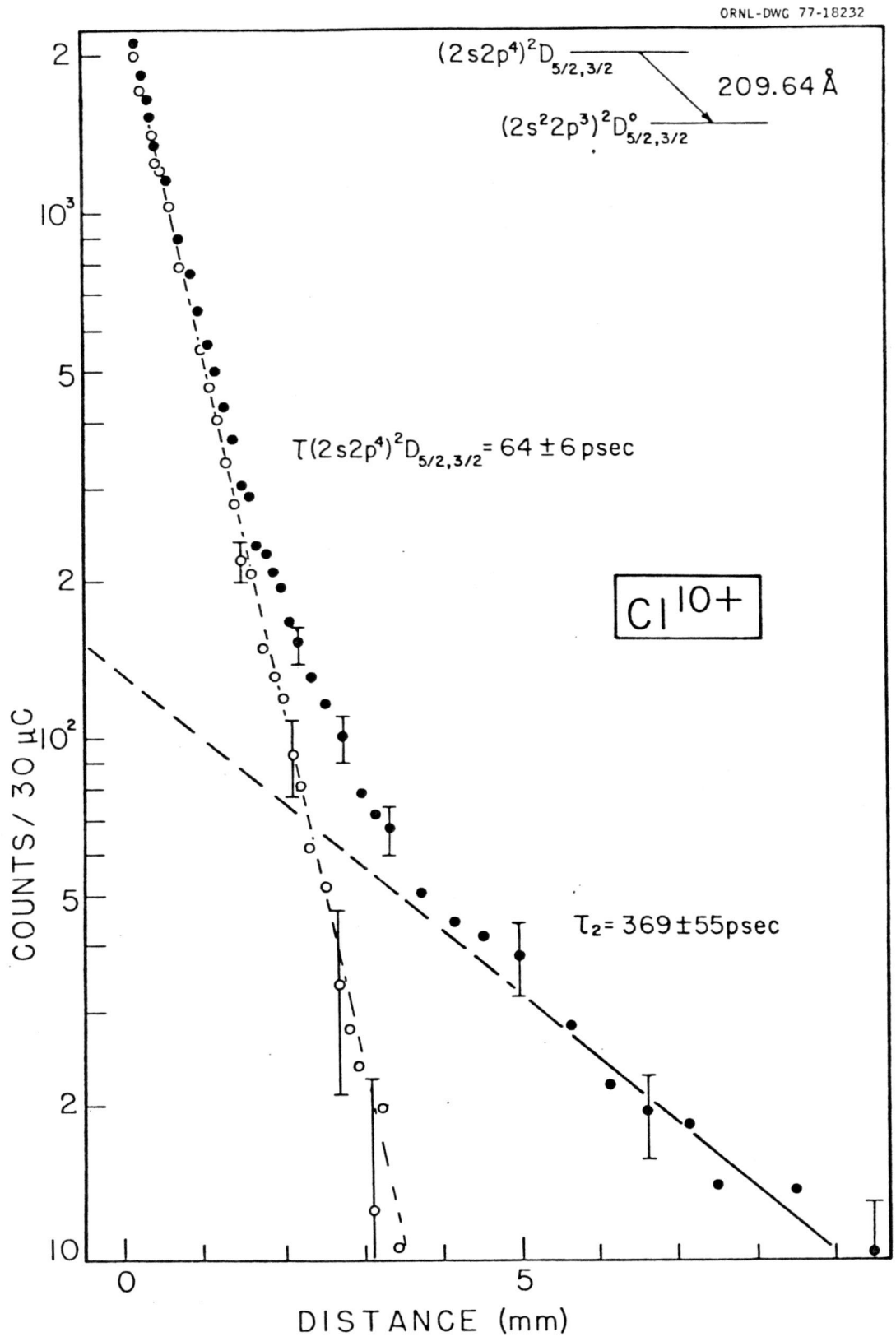


Figure 4.23. Intensity decay curve for the $(2s^22p^3)^2D^o_{5/2,3/2}$ - $(2s2p^4)^2D_{5/2,3/2}$ transition in Cl XI taken with an incident beam energy of 18 MeV.

An energy-level diagram of Cl X is shown in Figure 4.24. The doubly-excited $(1s^2 2p^6)^1S_0$ level is the only possible in-shell cascade contributor to the $(1s^2 2s2p^5)^1P_1$ level. The 215.5 Å line signaturing the decay of the $(1s^2 2p^6)^1S_0$ level had been previously unreported. As mentioned earlier, there exists a long-lived but weak component in all of the O-like decay curves that is of unknown origin. The nature of this long-lived component varies with each transition studied. As with Cl IX some of the level lifetimes measured for Cl X approach the lower limit for which a lifetime can be confidently measured with the present apparatus.

i) The decay curve for the 215.5 Å line associated with the $(1s^2 2s2p^5)^1P_1^o$ - $(1s^2 2p^6)^1S_0$ transition is shown in Figure 4.25. Analysis of this curve yielded a lifetime of 33 ± 7 psec for the $(1s^2 2p^6)^1S_0$ level. There are no expected in-shell cascades to this doubly-excited level and no other known lines fall within the 1.5 Å (fwhm) instrumental bandpass used in the measurement. The curve is best represented by two exponentials. The short-lived component is associated with the primary level being studied i.e. $(1s^2 2p^6)^1S_0$ while the origin of the weak, long-lived component ($\tau \sim 250$ psec) remains unknown.

ii) Analysis of the decay curve for the 164.5 Å line associated with the $(1s^2 2s^2 2p^4)^1D_2$ - $(1s^2 2s2p^5)^1P_1^0$ transition yielded a lifetime of 24 ± 5 psec. In-shell cascading from the $(1s^2 2p^6)^1S_0$ level is possible. However since the lifetime of this feeding level is comparable ($\tau \sim 33$ psec) to that of the primary level being studied it is very difficult to satisfactorily separate the two components. Cascading of

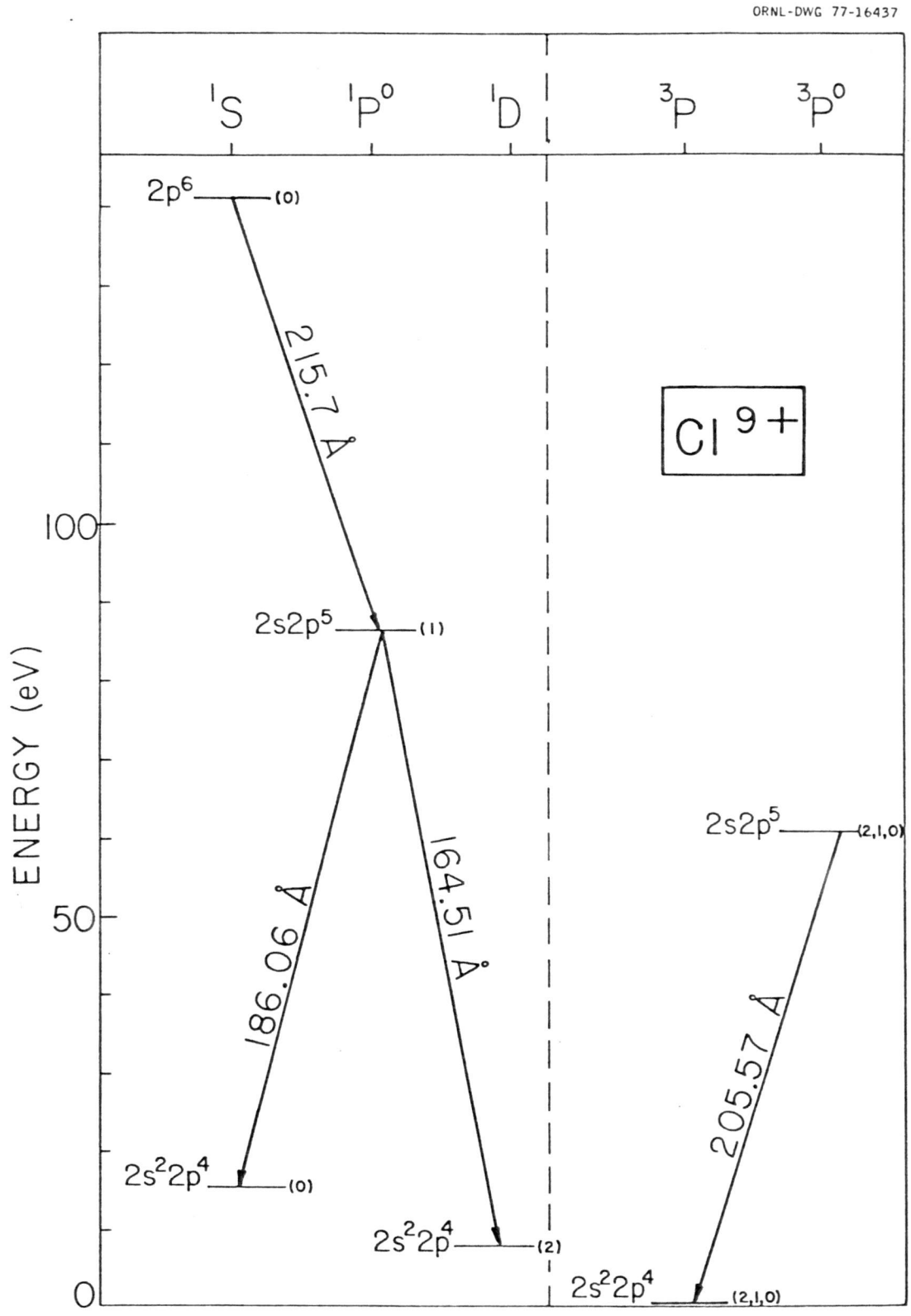


Figure 4.24. Partial energy level diagram of Cl X showing $\Delta n=0$ transitions within the L-shell. Multiplet averaged wavelengths are shown.

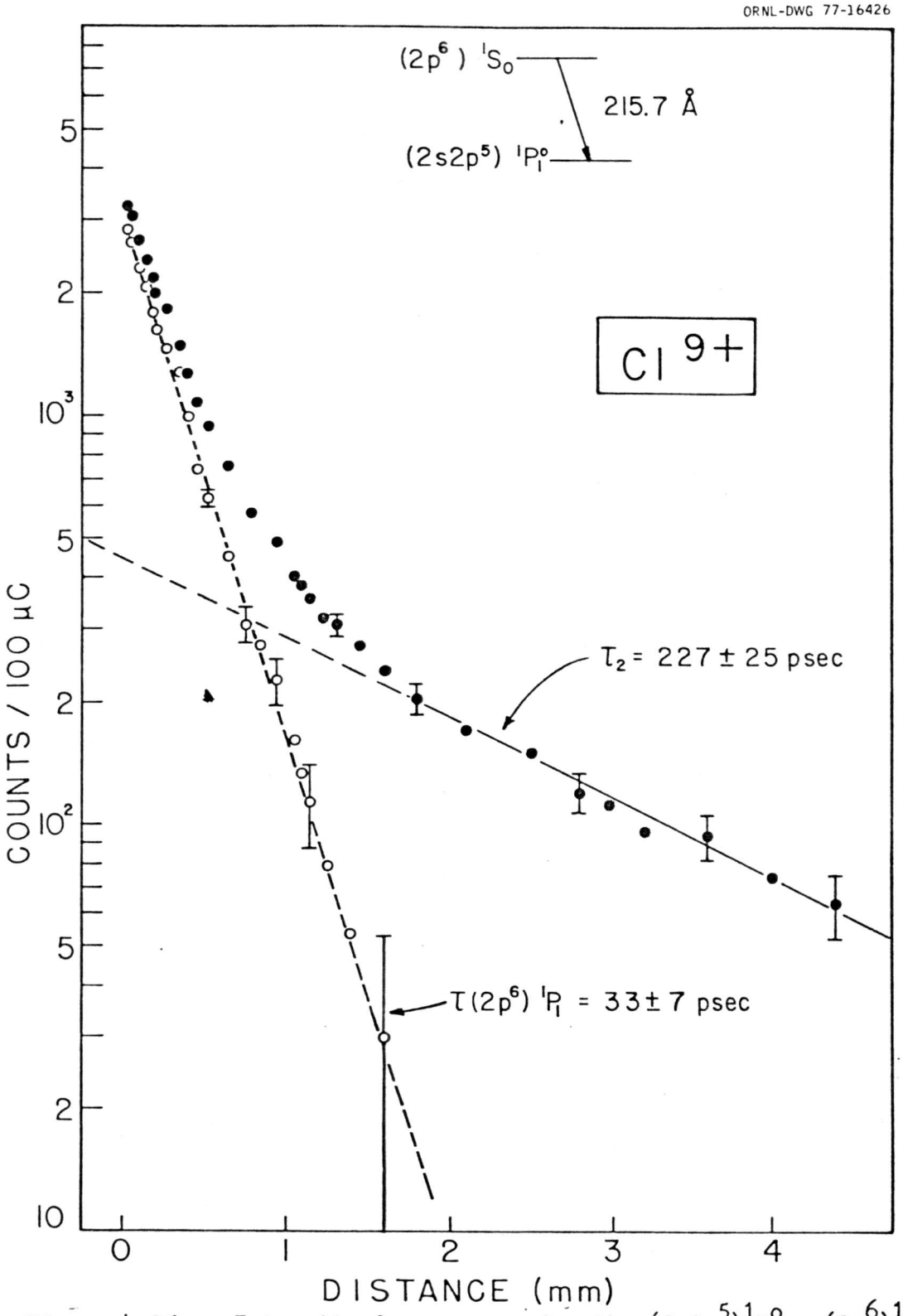


Figure 4.25. Intensity decay curve for the $(2s2p^5)^1P_1^o - (2p^6)^1S_0$ transition in Cl X taken with an incident beam energy of 18 MeV.

this type would cause the measured lifetime to be longer than the true value. When compared with theory (see Table 4.4, page 54) it is seen that the measured lifetime is indeed ~60% longer than the theoretical prediction. The long-lived component with a decay time of ~177 psec is of unknown origin.

iii) The decay curve of the 205.4 Å line associated with the $(1s^2 2s^2 2p^4)\,^3P_2 - (1s^2 2s 2p^5)\,^3P^o_2$ transition can be seen in Figure 4.26. Analysis of this curve yielded a lifetime of 62 ± 9 psec for the $(1s^2 2s 2p^4)\,^3P^o_2$ level. In-shell cascading to this level is not possible and no known lines fall within the 0.75 Å (fwhm) instrumental bandpass used in this measurement. However the curve is seen to be well represent by two exponentials. The short-lived component is associated with the decay of the primary level being studied i.e. $(1s^2 2s^2 2p^5)\,^3P_2$. The weak, long-lived component ($\tau \sim 480$ psec) is of unknown origin as has been the case in all of the 7- and 8-electron chlorine decay curves.

Cl IX (9-electron)

The lifetime of the $(1s^2 2s 2p^6)\,^2S_{1/2}$ level of F-like chlorine was measured. A beam energy of 8 MeV was used in this measurement. At this energy ~27% of the post-foil source is in the Cl^{8+} charge state. An energy-level diagram of Cl IX is shown in Figure 4.27. Also present in the decay curve is a weak, long-lived component similar to those that persisted throughout each of the decay curves for the N-like and O-like chlorine measurements.

i) The decay curve of the 180.7 Å line associated with the $(1s^2 2s^2 2p^5)\,^2P^o_{3/2} - (1s^2 2s 2p^6)\,^2S_{1/2}$ transition is shown in Figure 4.28.

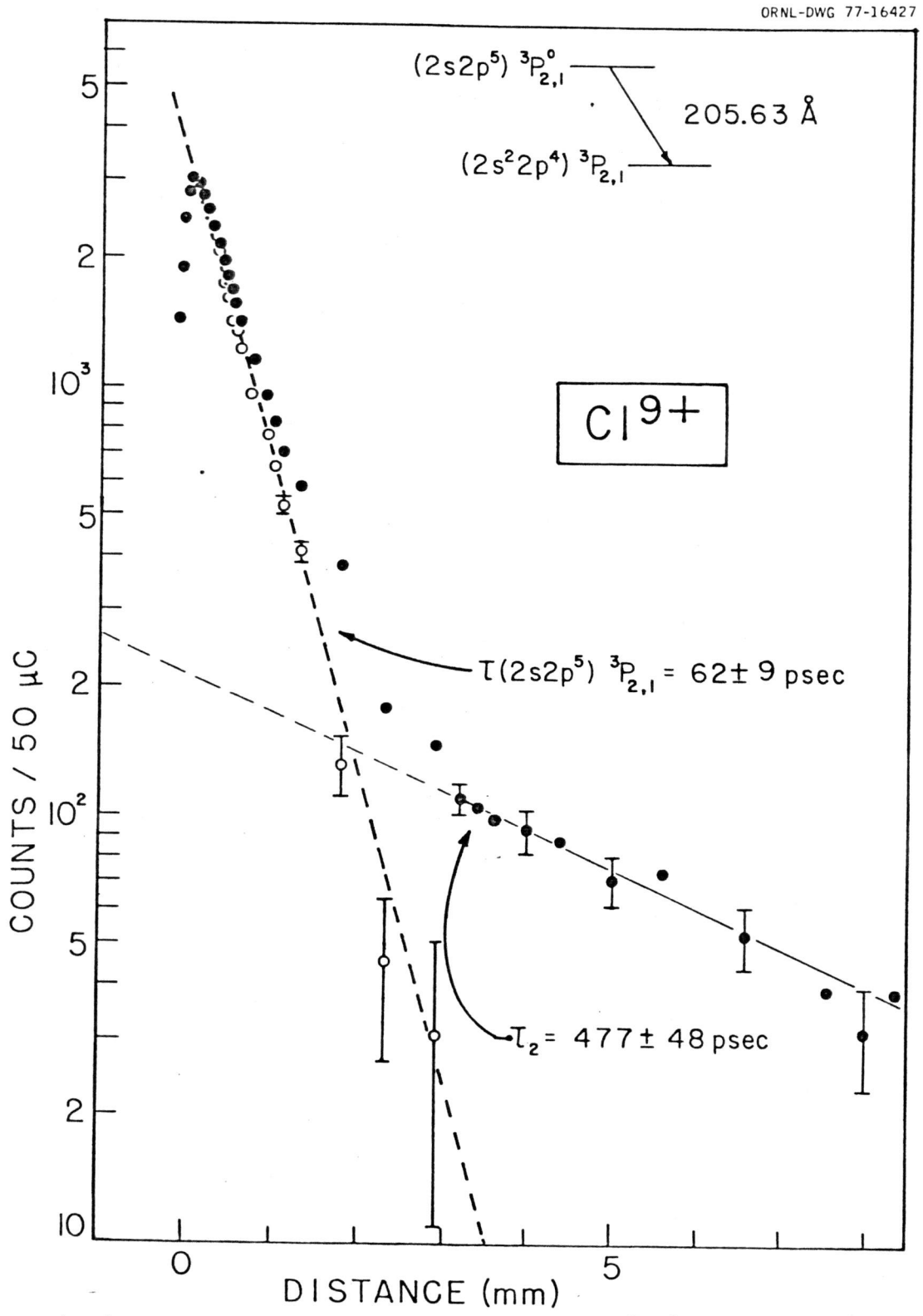


Figure 4.26. Intensity decay curve for the $(2s^2 2p^4)^3P_{2,1} - (2s2p^5)^3P^o_{2,1}$ transition in Cl X taken with an incident beam energy of 18 MeV.

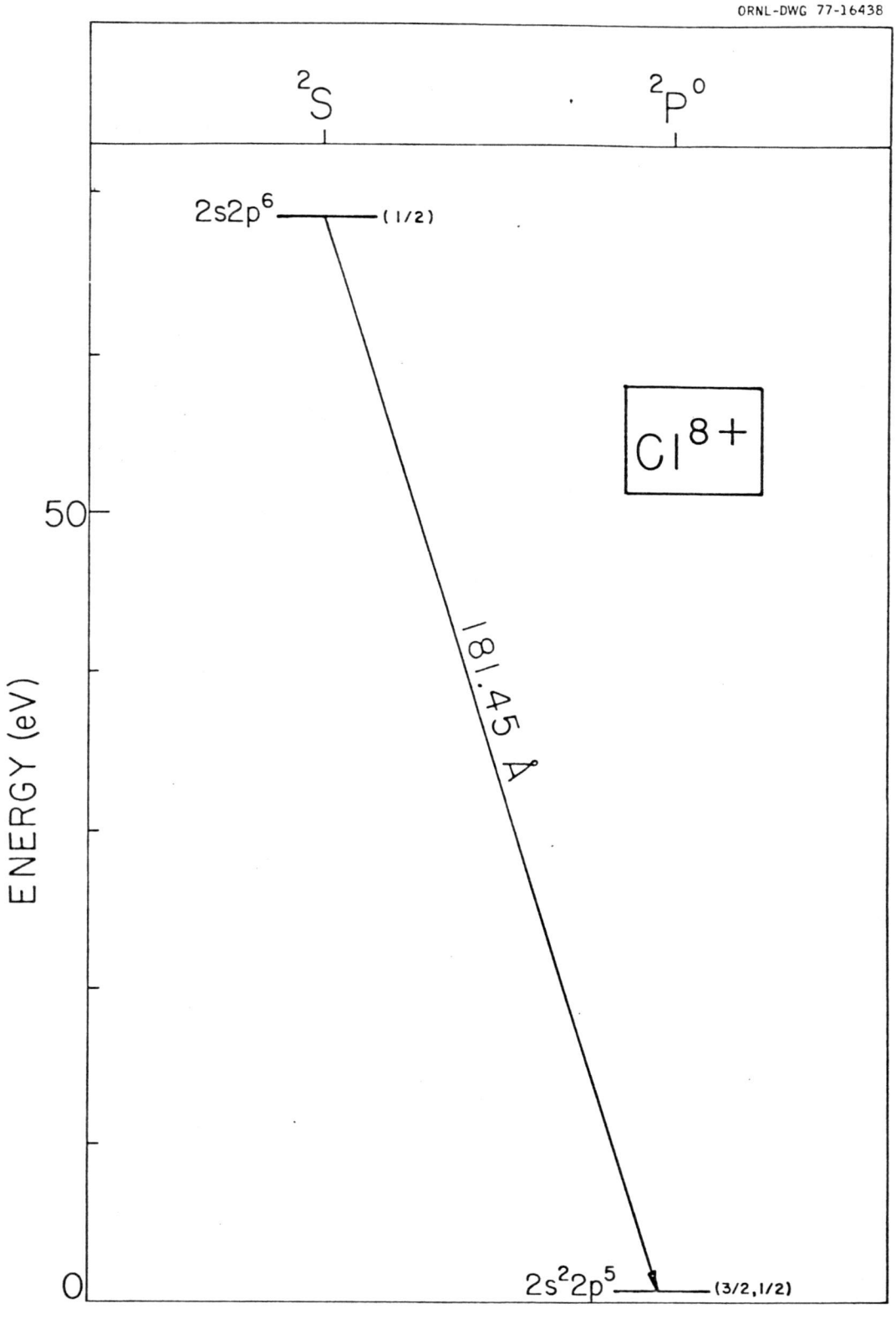


Figure 4.27. Partial energy level diagram of Cl IX showing $\Delta n=0$ transitions in the L-shell. Multiplet averaged wavelength is shown.

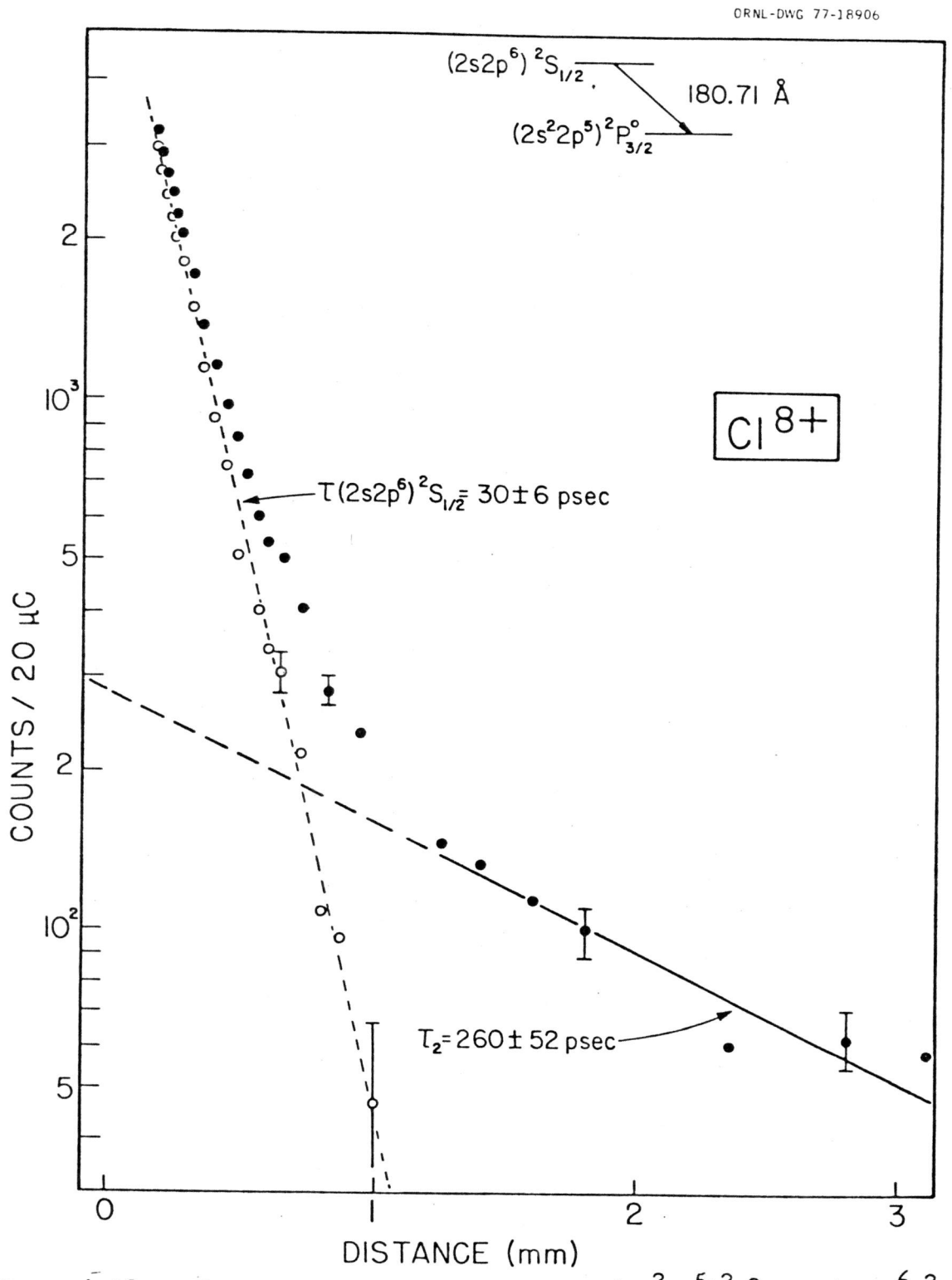


Figure 4.28. Intensity decay curve for the $(2s^2 2p^5)^2 P^o_{3/2}$ - $(2s2p^6)^2 S_{1/2}$ transition in Cl IX taken with an incident beam energy of 8 MeV.

Analysis of this decay curve yielded a lifetime of 30 ± 6 psec for the $(1s^2 2s2p^6)^2S_{1/2}$ upper level. There are no possible in-shell feeds to this level and no other known lines fall within the 1.5 Å (fwhm) instrumental bandpass used in this measurement. As can be seen in Figure 4.28, the curve is best represented by two exponentials. The short-lived component can be associated with the decay of the $(1s^2 2s2p^6)^2S_{1/2}$ primary level but the long-lived component is of unknown origin.

CHAPTER 5

DISCUSSION OF RESULTS

Table 5.1 lists the transition probabilities (A-values) and f-values that were derived from the lifetime results in the present work along with some theoretically-predicted f-values. Whenever necessary multiplet f-values have been calculated with equation (2.5) using average multiplet wavelengths and assuming that the lifetime of individual levels within a term are equal (as will be the case in valid LS coupling). The average wavelengths were calculated by the standard weighting method using energy level values that were obtained by higher-resolution spectroscopic techniques.[15]

In general the uncertainties quoted on the present results ($\sim$5-25%) are comparable to the estimated errors on the theoretical predictions. These uncertainties are arrived at in the following manner. Systematic uncertainties arising e.g. from determination of post-foil beam velocity, the reproducibility of target position and the beam-charge normalization procedure are estimated to be small ($\leq$ 1%) at the high-incident beam energies employed in the present work. Statistical uncertainties associated with the decay curve fitting process depend to some extent upon the intensity of the spectral line under study and whether or not the analysis is complicated by cascade-effects brought about by the non-selective excitation process. A 5% uncertainty limit, based upon the

---

[15] B. C. Fawcett, Atomic Data and Nuclear Data Tables 16, 135 (1975).

TABLE 5.1

TRANSITION RATES AND f-VALUES FOR $\Delta n = 0$ TRANSITIONS WITHIN THE L-SHELL OF MULTIPLY-CHARGED CHLORINE IONS

Ion	$\bar{\lambda}$(Å)	Multiplet	Present Transition Probability ($10^{10}s^{-1}$)	Multiplet Oscillator Strengths	
				Present	Theory
Cl XV	394.5	$(2s)^2S - (2p)^2P$	0.12	0.085 ± .004	0.090[a], 0.087[d], 0.082[e]
Cl XIV	277.9	$(2s2p)^1P - (2p^2)^1S$	15	0.058 ± .009	0.052[b], 0.049[e]
	458.4	$(2s2p)^1P - (2p^2)^1D$	1.7	0.088 ± .009	0.082[b], 0.078[e]
	237.8	$(2s^2)^2S - (2s2p)^1P$	0.67	0.17 ± .03	0.22[b], 0.21[d], 0.208[e]
	285.5	$(2s2p)^3P - (2p^2)^3P$	0.63	0.076 ± .004	0.079[e]
Cl XIII	215.0	$(2s^22p)^2P - (2s2p^2)^2S$	1.3	0.029 ± .003	0.026[b], 0.032[c], 0.026[e]
	200.8	$(2s^22p)^2P - (2s2p^2)^2P$	1.7	0.10 ± .01	0.137[b], 0.14[c], 0.14[e]
	272.8	$(2s^22p)^2P - (2s2p^2)^2D$	0.33	0.057 ± .006	0.054[b], 0.058[c], 0.053[e]
	227.6	$(2s2p^2)^4P - (2p^3)^4S$	1.9	0.047 ± .005	0.056[c], 0.052[e]
Cl XII	175.6	$(2s^22p^2)^3P - (2s2p^3)^3S$	3.6	0.055 ± .010	0.077[b], 0.075[e]
	225.7	$(2s^22p^2)^3P - (2s2p^3)^3P$	0.76	0.058 ± .003	0.064[b], 0.062[e]
	265.3	$(2s^22p^2)^3P - (2s2p^3)^3D$	0.31	0.055 ± .003	0.055[b], 0.058[e]

TABLE 5.1 (continued)

Ion	$\overline{\lambda}$(Å)	Multiplet	Present Transition Probability ($10^{10}s^{-1}$)	Multiplet Oscillator Strengths	
				Present	Theory
Cl XII	199.3	$(2s^2 2p^2)^1D - (2s2p^3)^1D$	1.4	0.085 ± .004	0.085[b], 0.145[e]
Cl XI	191.7	$(2s^2 2p^3)^2P - (2s2p^4)^2S$	3.4	0.046 ± .005	0.049[b], 0.049[e]
	239.6	$(2s^2 2p^3)^4S - (2s2p^4)^4P$	0.57	0.15 ± .015	0.141[b], 0.149[e]
Cl X	215.5	$(2s2p^5)^1P - (2p^6)^1S$	4.6	0.11 ± .02	0.133[e]
	205.5	$(2s^2 2p^4)^3P - (2s2p^5)^3P$	1.6	0.10 ± .015	0.116[b], 0.120[e]
Cl IX	181.5	$(2s2p^5)^2P - (2s2p^6)^2S$	3.3	0.055 ± .01	0.063[b], 0.071[e]

[a]Y. K. Kim and J. P. Desclaux, Physical Review Letters 36, 139 (1976). The values listed in the table are extrapolations fo the results reported by the above authors.

[b]O. Sinanoglu, Nuclear Instruments and Methods 110,193 (1973). The values listed in the table are extrapolations of the results reported by the above author.

[c]L. J. Shamey, Journal of the Optical Society of America 61, 942 (1970). The values listed in the table are extrapolations of the results reported by the above author.

[d]L. Armstrong, W. R. Fielder, and D. L. Lin, Physical Review A14, 1114 (1970). The values listed in the table are extrapolations of the results reported by the above authors.

[e]U. I. Safronova, A. N. Ivanova, and V. N. Kharitonova, Theoretical and Experimental Chemistry 5, 325 (1969).

curve-fitting analysis, has been quoted for lifetimes in Table 4.4 (see page 54) for transitions which are intense and are apparently unaffected by cascading or blending. If the line is weaker, the uncertainty limit for several cascade-free transitions has been increased to 10% or more to reflect the reduced counting statistics. In extreme cases in which strong cascading or blending occurs and in cases for which the cascading level has a lifetime comparable to that of the primary level being studied, the uncertainties can be as large as 25% or more. Large quoted uncertainties also arise when the lifetime of the level being studied approaches the lower limit of the apparatus. The uncertainties quoted for the f-values in Table 5.1 are equal to the uncertainties of the lifetimes of the upper level of the particular transition as quoted in Table 4.4.

The theoretical values listed in Table 5.1 represent several different types of calculations. The calculations of Kim and Desclaux[16] as well as those of Armstrong et al.[17] are based upon a relativistic multi-configurational model employing Dirac-Hartree-Fock zeroth-order wave-functions. Shamey[18] used the Hartree-Fock method with the inclusion of spin-orbit interaction and limited configuration mixing. The Z-expansion calculations of Safronova et al.[19] are based upon non-relativistic

---

[16] Y. Kim and J. Desclaux, Physical Review Letters 36, 139 (1976)

[17] L. Armstrong, W. R. Fielder, and D. L. Lin, Physical Review A14, 1114 (1970).

[18] L. J. Shamey, Journal of Optical Society of America 61, 942 (1970).

[19] U. I. Safronova, A. N. Ivanova, and V. N. Kharitonova, Theoretical and Experimental Chemistry 5, 325 (1969).

perturbation theory including some configuration interaction but not a sufficient amount to account for important correlation effects in low Z ions. Possibly the most sophisticated of the non-relativistic calculations quoted in Table 5.1 are those of Sinanoglu and coworkers.[20] These calculations effectively treat the electron-correlation problem by considering the interactions between pairs of electrons using a procedure named the Non-Closed Shell Many Electron Theory (NCMET).

A convenient way of graphically comparing experimental results with theory for many different members of an isoelectronic sequence is to make a f versus Z^{-1} plot for the transition. Such a comparison is based upon the non-relativistic approximation and provides a method of observing systematic regularities for low-to-moderately ionized members of the sequence.

The theoretical oscillator strengths quoted in Table 5.1 and credited to Kim and Desclaux, Sinanoglu, Shamey and Armstrong et al. are obtained by graphical extrapolation of calculated values toward greater nuclear charge. In the very high Z regime relativistic effects become significant and f-values tend to increase over the non-relativistic predictions.

Cl XV (3-electron)

Both members of the 2s-2p resonance doublet in the lithium-like ion, Cl XV, were studied in the present experiment. The line f-values derived from the measured lifetimes were found to be 0.28 and 0.57 for

---

[20]Sinanoglu 110, p. 193.

the $(1s^2 2s)^2S_{1/2}$ - $(1s^2 2p)^2P^o_{1/2}$ and the $(1s^2 2s)^2S_{1/2}$ - $(1s^2 2p)^2P_{3/2}$ transitions respectively. The multiplet f-value for this doublet was derived from the line f-values using the equation:

$$f_{ji}^{mult.} = \frac{1}{\bar{\lambda}\sum_{J_j}(2J_j+1)} \sum_{J_j,J_i} (2J_j+1)\ \lambda(J_j,J_i)\ f(J_j,J_i),$$

where $\bar{\lambda}$ is the average wavelength of the multiplet, J_i and J_j are the angular momenta of the upper and the lower states respectively, and λ and f are the line wavelength and oscillator strength respectively. Figure 5.1 shows the results displayed on an f versus Z^{-1} plot for the Li-sequence. The solid curve represents the calculations of Kim and Desclaux. Figure 5.2 shows a sequence plot of line f-values for lithium-like ions with $Z \geq 10$. Again the solid curve represents the calculations of Kim and Desclaux and the present results are shown as black dots. The present results for the line f-values are seen to be in good agreement with theory for both the 1/2-1/2 and the 1/2-3/2 transitions.

Cl XIV (4-electron)

The f-value results for three of the four transitions studied in the Be-like ion, Cl XIV, are in essential agreement with theory. The problem associated with the curve-fitting analysis of the decay curve for the resonance transition, $(1s^2 2s^2)^1S$ - $(1s^2 2s2p)^1P^o$, has already been discussed in Chapter 4. The doubly-excited $(1s^2 2s^2)^1S_0$ level produces a particularly difficult cascade situation which makes it impossible to obtain a satisfactory result at the level of counting statistics employed. The uncertainty limits quoted on the result for this transition attempts to take this problem into account. Figure 5.3

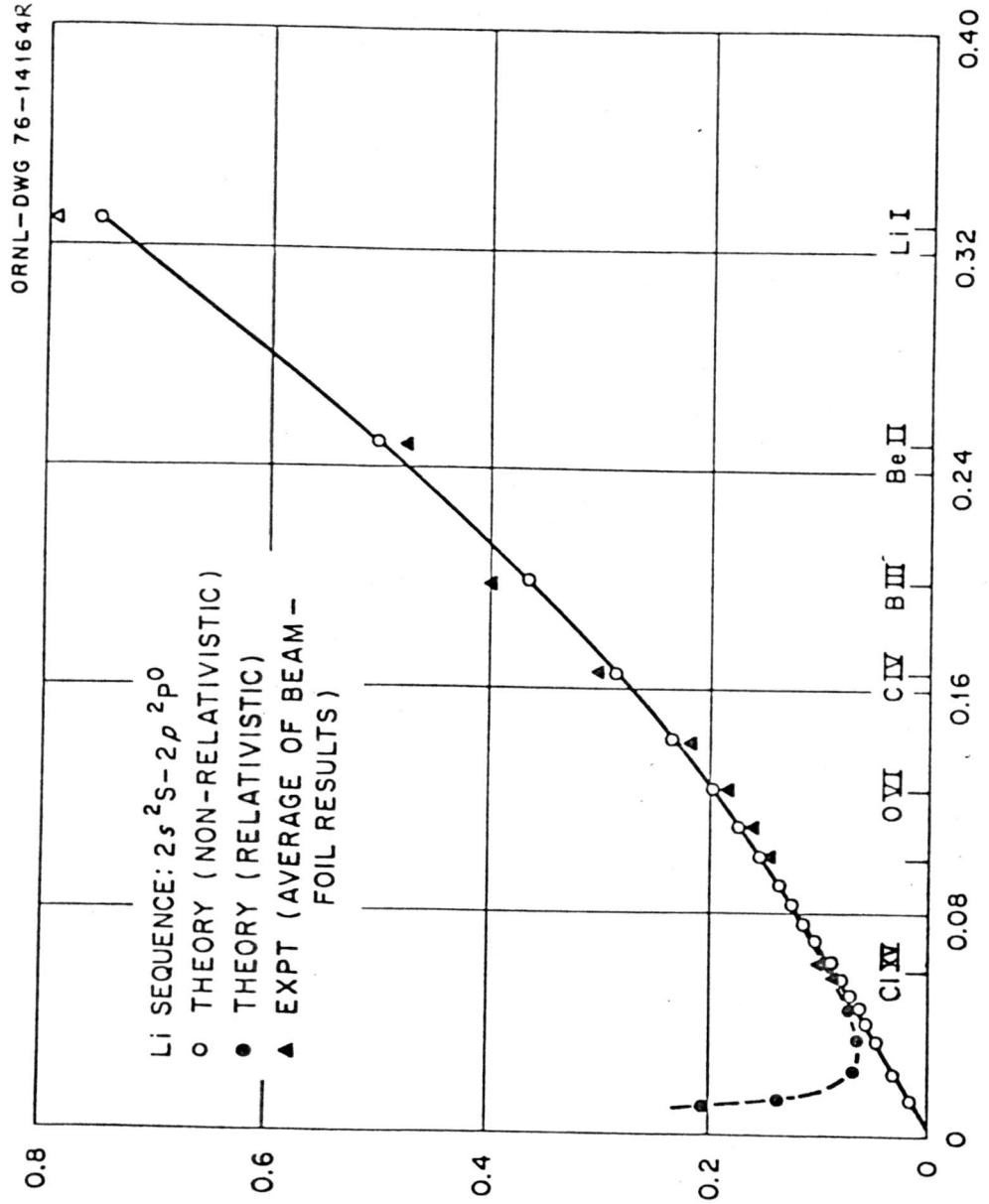


Figure 5.1. Isoelectronic sequence plot showing the multiplet f-value of the $(2s)^2S - (2p)^2P^o$ transition versus inverse nuclear charge.

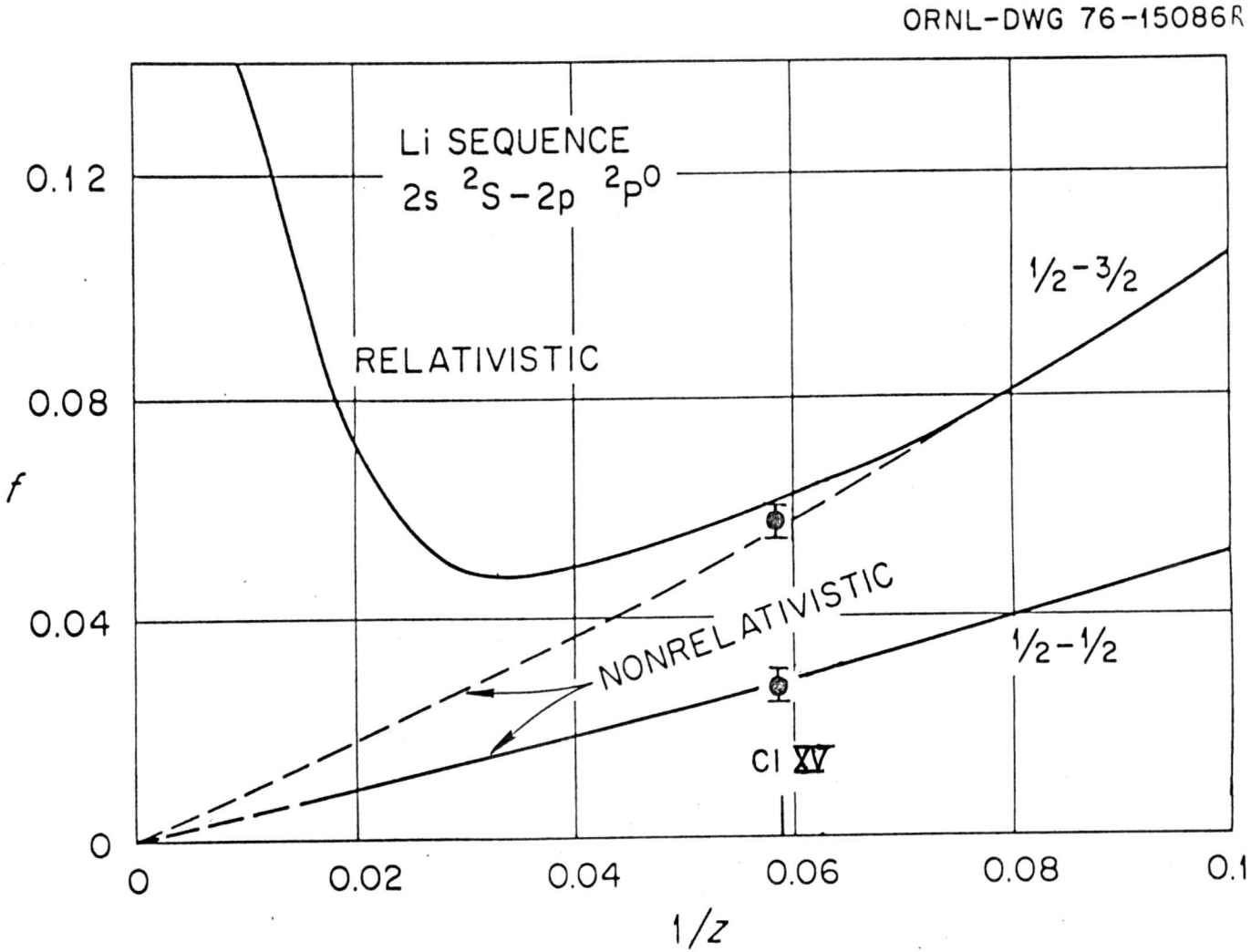


Figure 5.2. Isoelectronic sequence plot showing the line f-values of the Li-like transitions as measured in the present work.

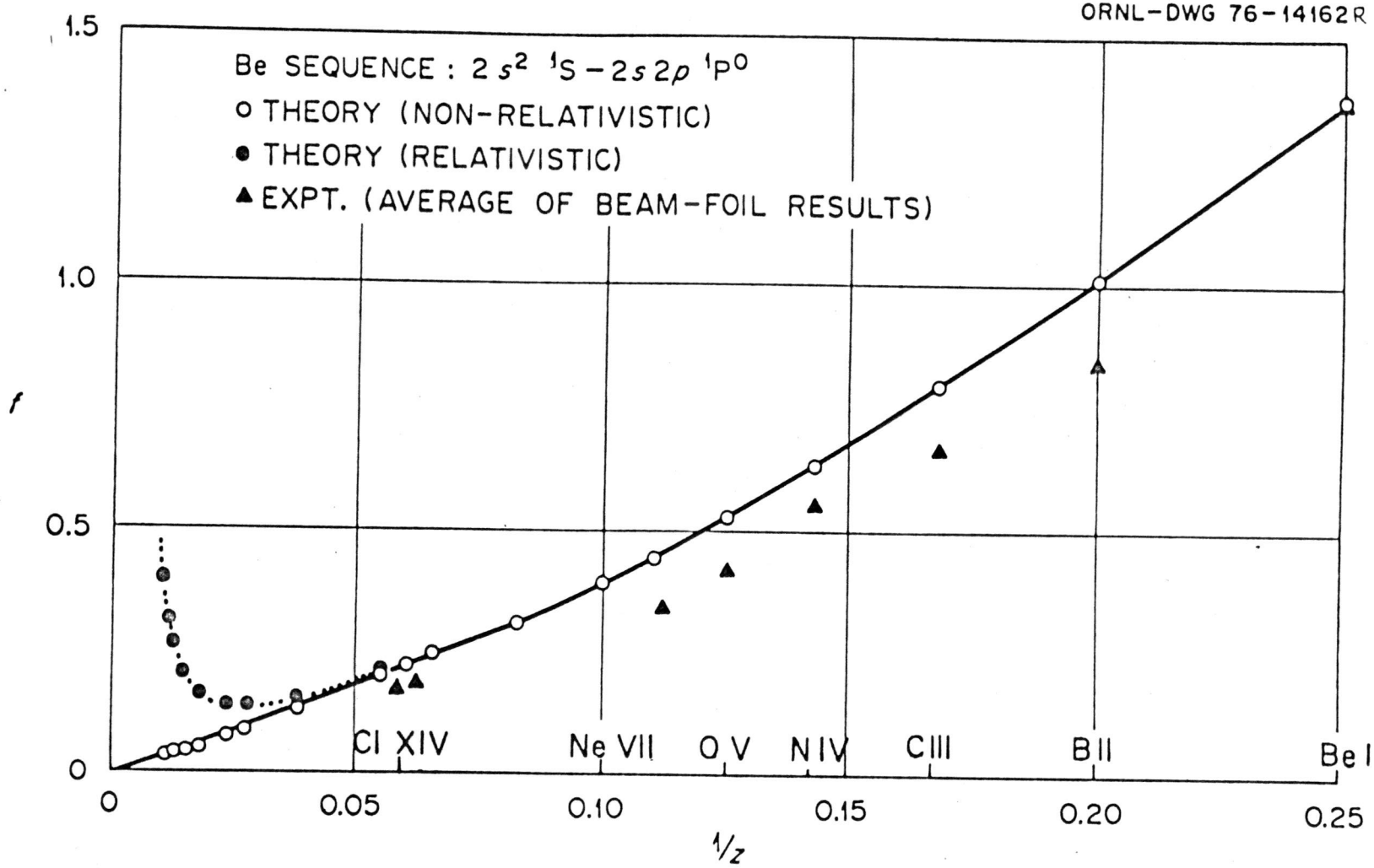


Figure 5.3. Isoelectronic sequence plot showing the multiplet f-value of the $(2s^2)^1S$ - $(2s2p)^1P^o$ transition versus inverse nuclear charge.

shows that this same cascade problem appears to exist for most of the other members of the Be-sequence. The beam-foil result for Be I however is in excellent agreement with theory presumably because the $(1s^2 2p^2)^1S_0$ level deexcites predominately via autoionization in this case. Figure 5.4 shows the f-values for the $(1s^2 2s2p)^1P^o$ - $(1s^2 2p^2)^1S$ transition along the Be-sequence. A similar plot for the $(1s^2 2s2p)^3P$ - $(1s^2 2p^2)^3P$ multiplet is shown in Figure 5.5. It can be seen that agreement between beam-foil results and theory is generally quite good throughout the sequence. The solid curve represents the non-relativistic calculations of Sinanoglu. Extrapolations to higher members of the sequence were made using Sinanoglu's lower Z results. The relativistic calculations of Kim and Desclaux are shown as dotted lines. Figure 5.6 shows the f versus Z^{-1} plot for the $(1s^2 2s2p)^1P$ - $(1s^2 2p^2)^1D$ transition which feeds the $(1s^2 2s2p)^1P$ level. Again the agreement between beam-foil results and theory along the entire sequence is generally good. The solid line in Figure 5.5 represents Sinanoglu's calculations. An extrapolation to higher members of the sequence is represented by a dotted line. The relativistic calculations, also represented by a dotted line, are those of Kim and Desclaux.

Cl XIII (5-electron)

The f-values determined for four transitions in the B-like ion, Cl XIII, are shown in Table 5.1. The experimentally obtained f-value for the $(1s^2 2s^2 2p)^2P^o$ - $(1s^2 2s2p^2)^2S$ transition is in essential agreement with the theoretical values as is seen in Table 5.1. A sequence plot of the f-value for this transition versus Z^{-1} is shown in Figure 5.7

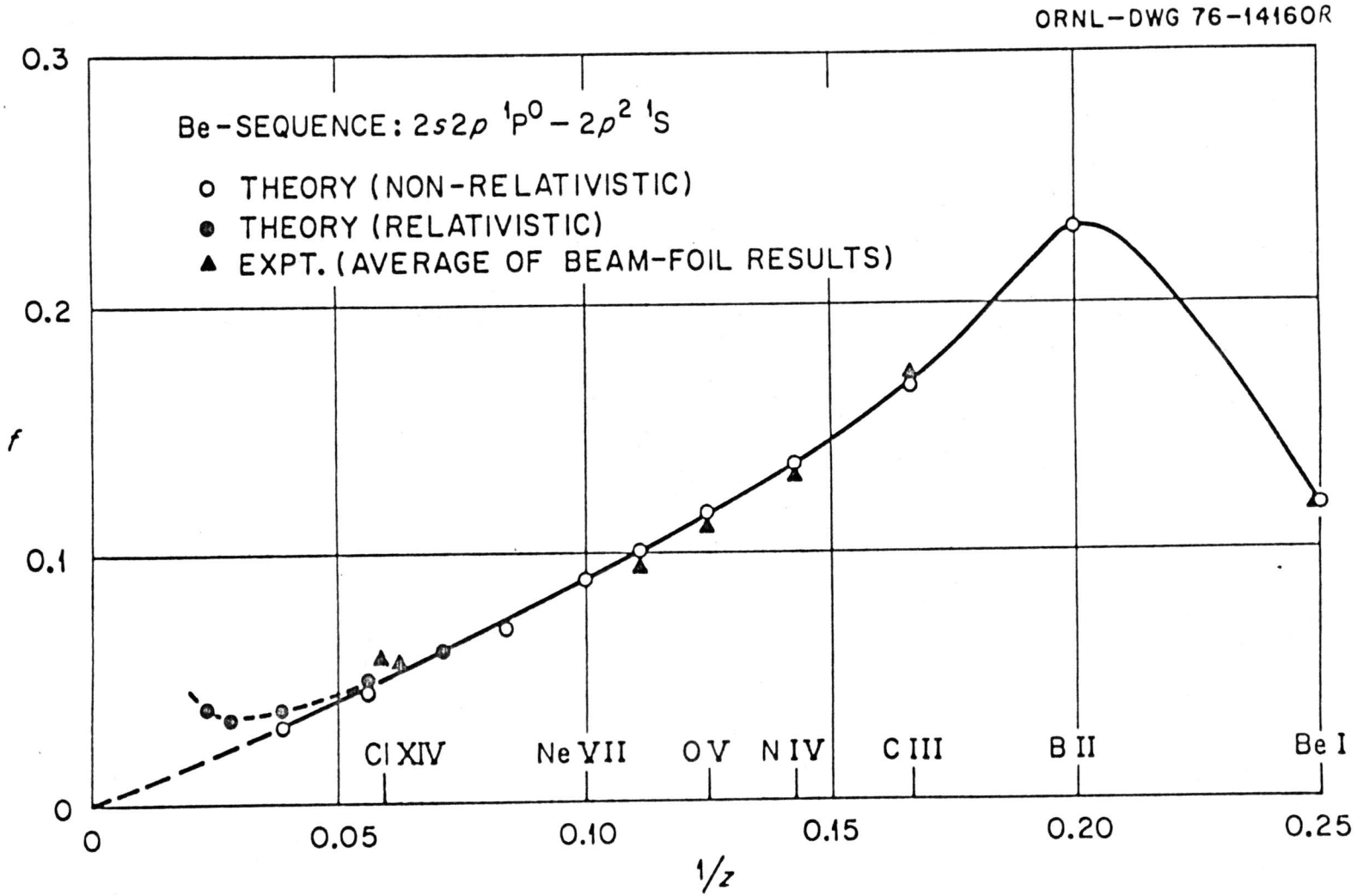


Figure 5.4. Isoelectronic sequence plot showing the multiplet f-value of the $(2s2p)^1P^o$ - $(2p^2)^1S$ transition versus inverse nuclear charge.

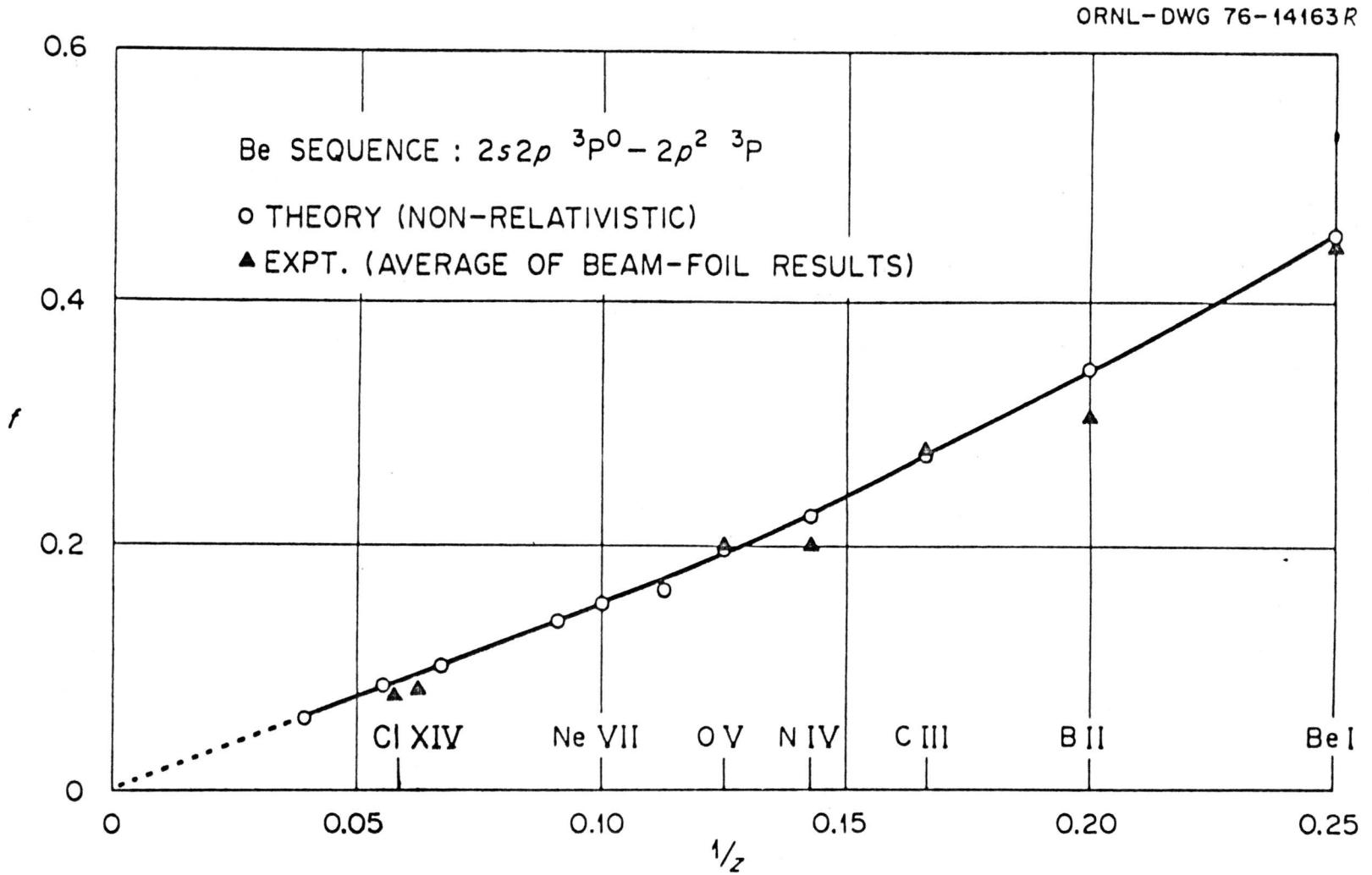


Figure 5.5. Isoelectronic sequence plot showing the multiplet f-value of the $(2s2p)^3P^o$ - $(2p^2)^3P$ transition versus inverse nuclear charge.

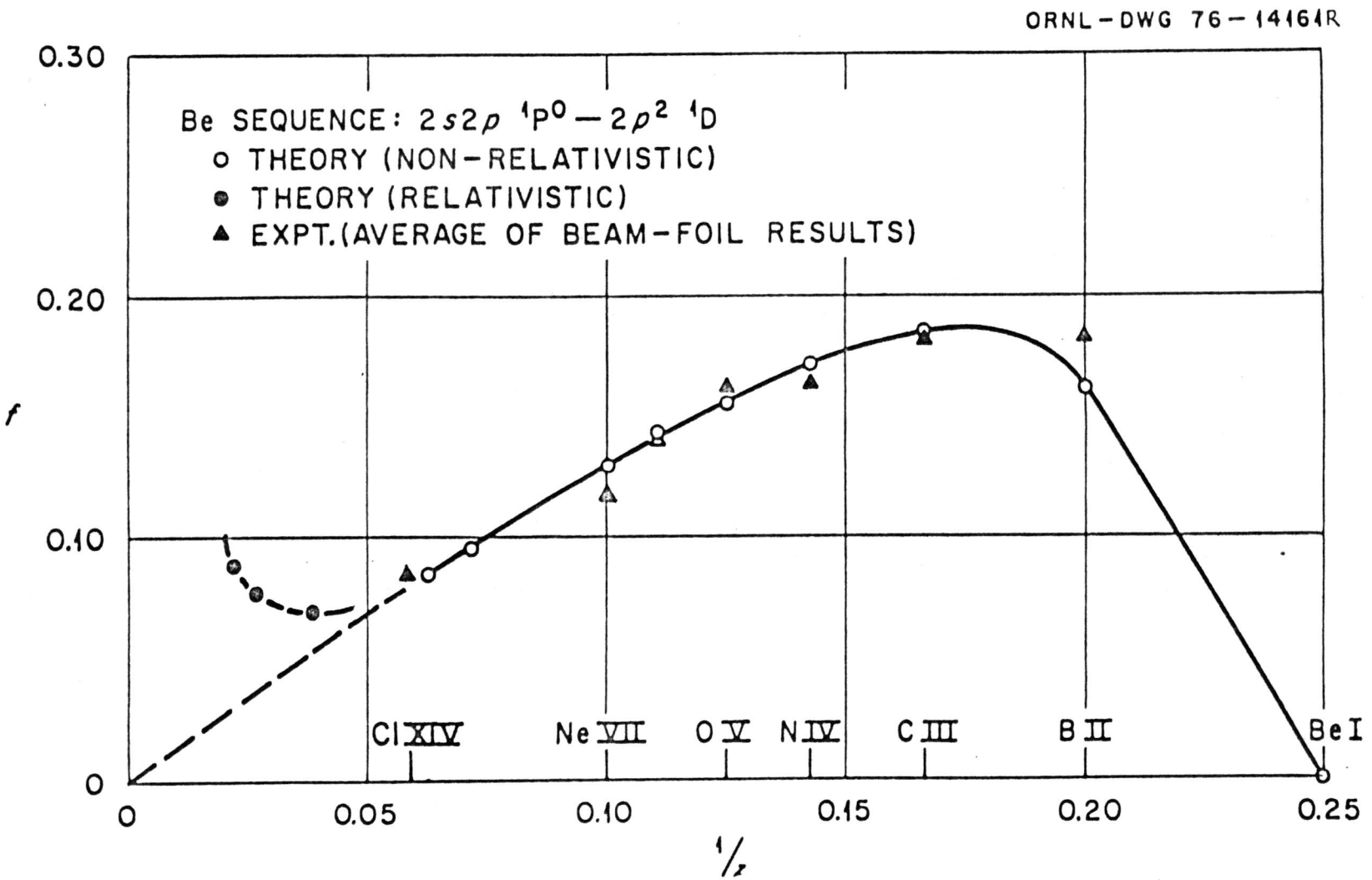


Figure 5.6. Isoelectronic sequence plot showing the multiplet f-value of the $(2s2p)^1P^o$ - $(2p^2)^1D$ transition versus inverse nuclear charge.

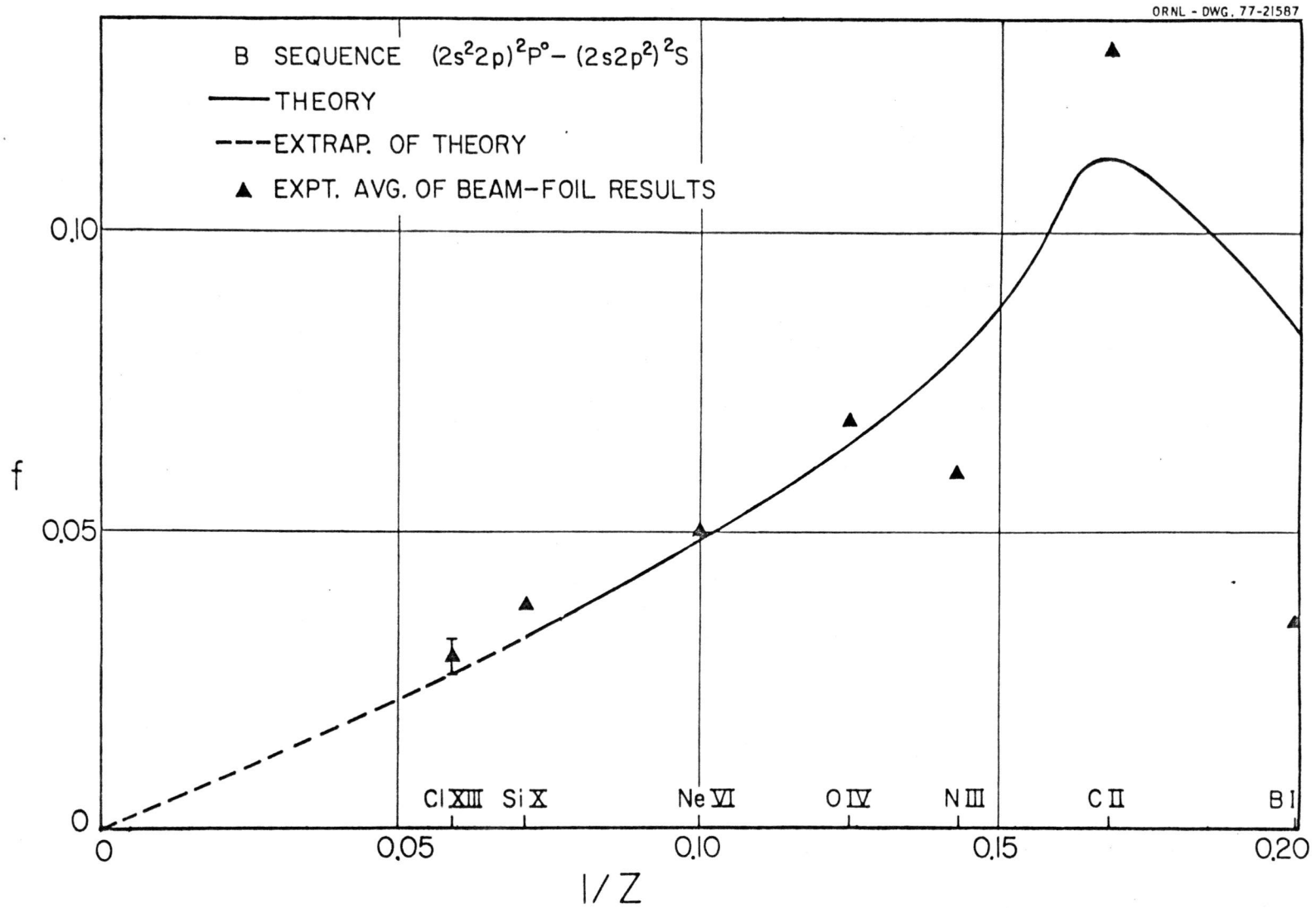


Figure 5.7. Isoelectronic sequence plot showing the multiplet f-value of the $(2s^2 2p)^2P^o$ - $(2s2p^2)^2S$ transition versus inverse nuclear charge.

with the theoretical predictions of Sinanoglu depicted by a continuous line. The dashed line is an extrapolation of Sinanoglu's results. Referring to Figure 5.7, the experimental results appear to lie slightly above the theoretical curve for values of nuclear charge greater than eight. Since high f-values cannot be explained by experimental problems such as cascading, such a situation could indicate that the theoretical results are somewhat in error in this case. The f-value presently quoted for the $(1s^2 2s^2 2p)^2P^o$ - $(1s^2 2s 2p^2)^2P$ transition is lower than theory predicts but it is seen from Figure 5.8 that all but one of the beam-foil experimental values also lie lower than Sinanoglu's calculations. These low f-values may be attributed to the cascade situation for this level i.e. repopulation from the levels of the $(1s^2 2p^3)^2P^o$ term (as was discussed in Chapter 4). The f-value quoted in the present work for the $(1s^2 2s^2 2p)^2P^o$ - $(1s^2 2s 2p^2)^2D$ transition is seen in Figure 5.9 to lie between the extrapolated non-relativistic calculations of Sinanoglu and the relativistic calculations of Sinanoglu and Luken which are plotted with a dotted line. The f-value for the $(1s^2 2s 2p^2)^3P$ - $(1s^2 2p^3)^4S^o$ transition is shown in Figure 5.10. The theoretical curve, which is from the work of Safronova et al., is depicted by a solid line.

Cl XII (6-electron)

F-values for the singlet and three of the triplet transitions of the C-like ion, Cl XII, were determined in this experiment. In Table 5.1 it is seen that experimental f-values for the $(1s^2 2p^2)^3P$ - $(1s^2 2s 2p^3)^3S$ transition is some $\sim$27% lower than theory predicts.

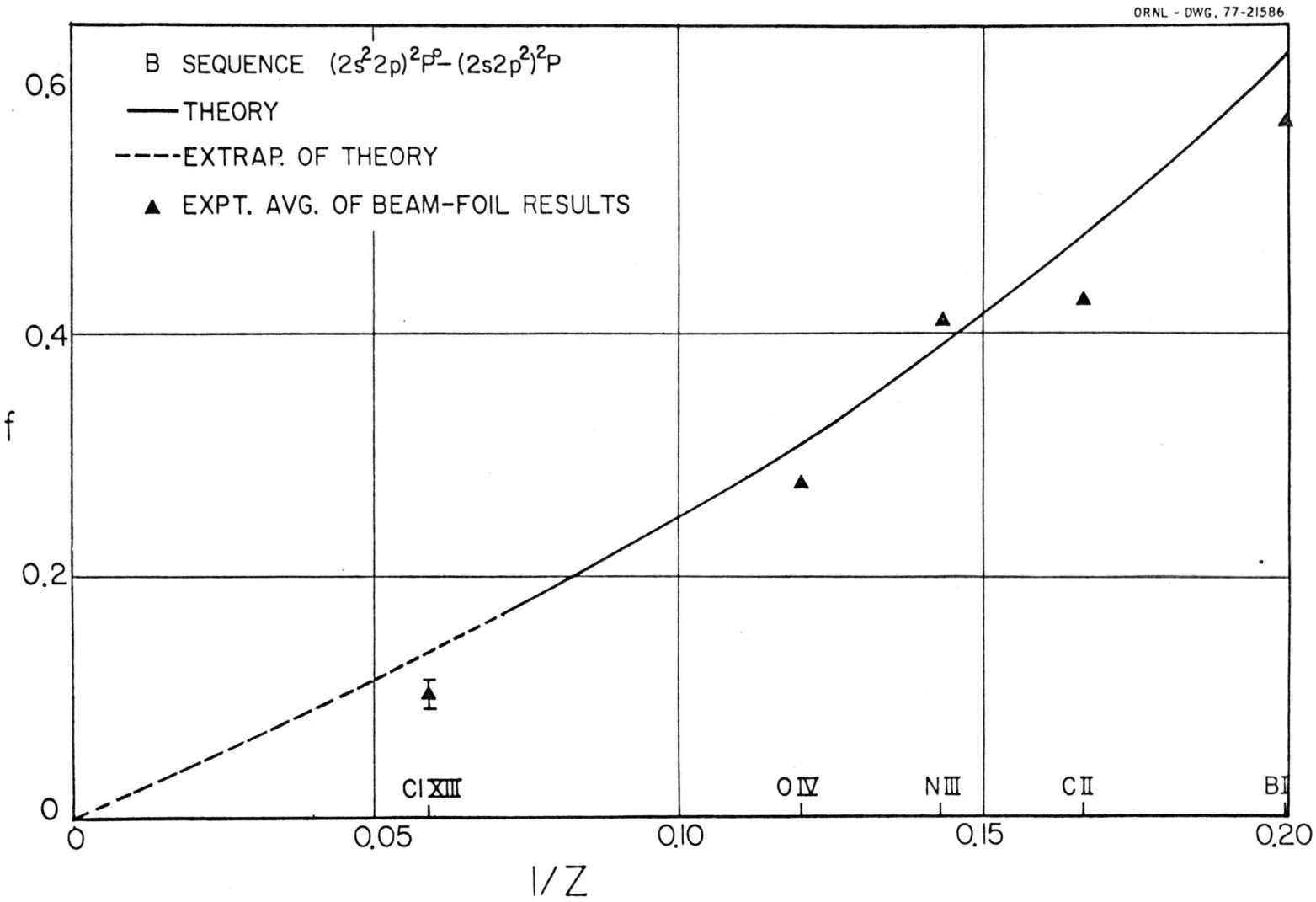


Figure 5.8. Isoelectronic sequence plot showing the multiplet f-value of the $(2s^2 2p)^2P^o - (2s2p^2)^2P$ transition versus inverse nuclear charge.

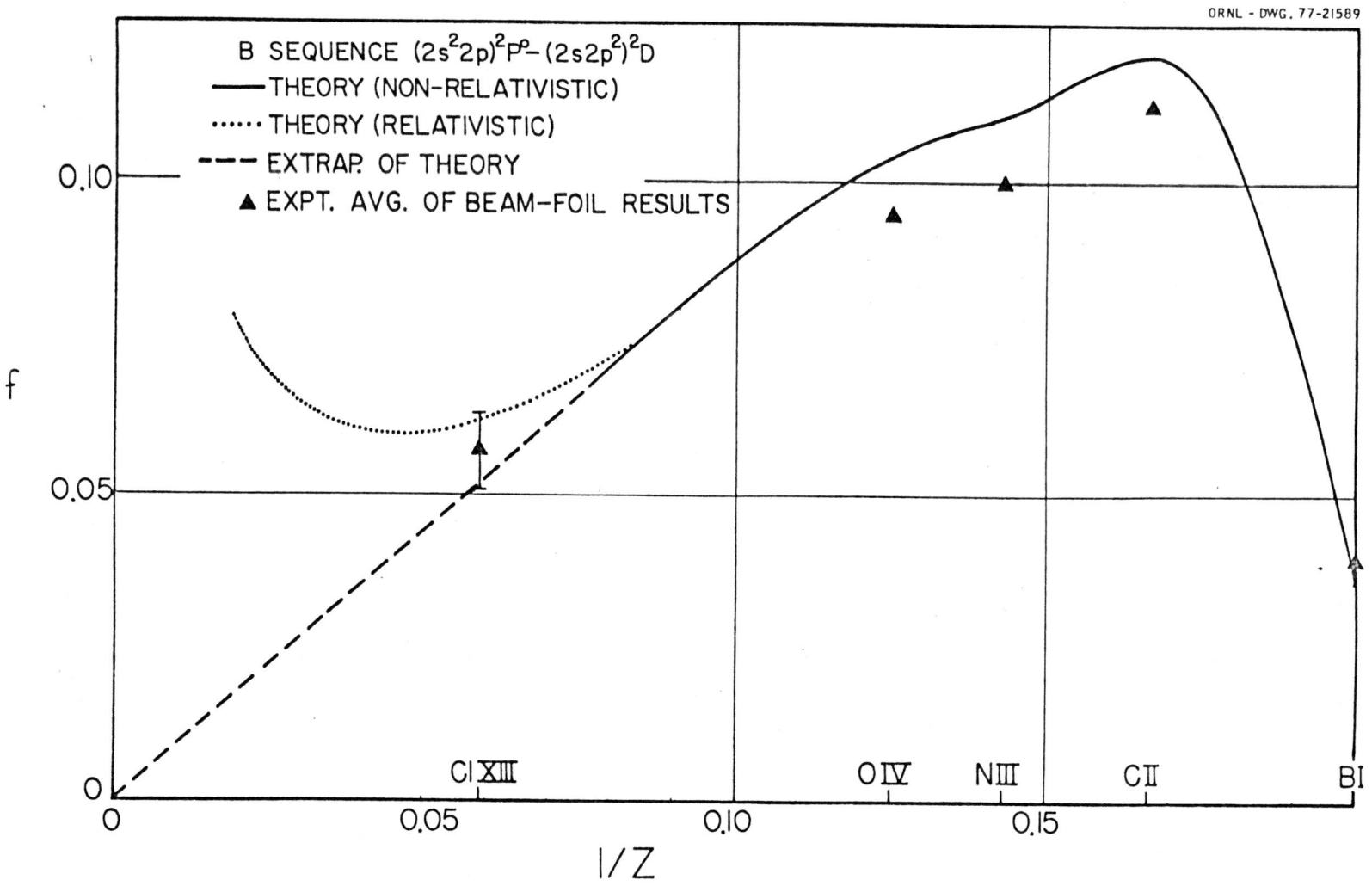


Figure 5.9. Isoelectronic sequence plot showing the multiplet f-value of the $(2s^2 2p)^2P^o$ - $(2s2p^2)^2D$ transition versus inverse nuclear charge.

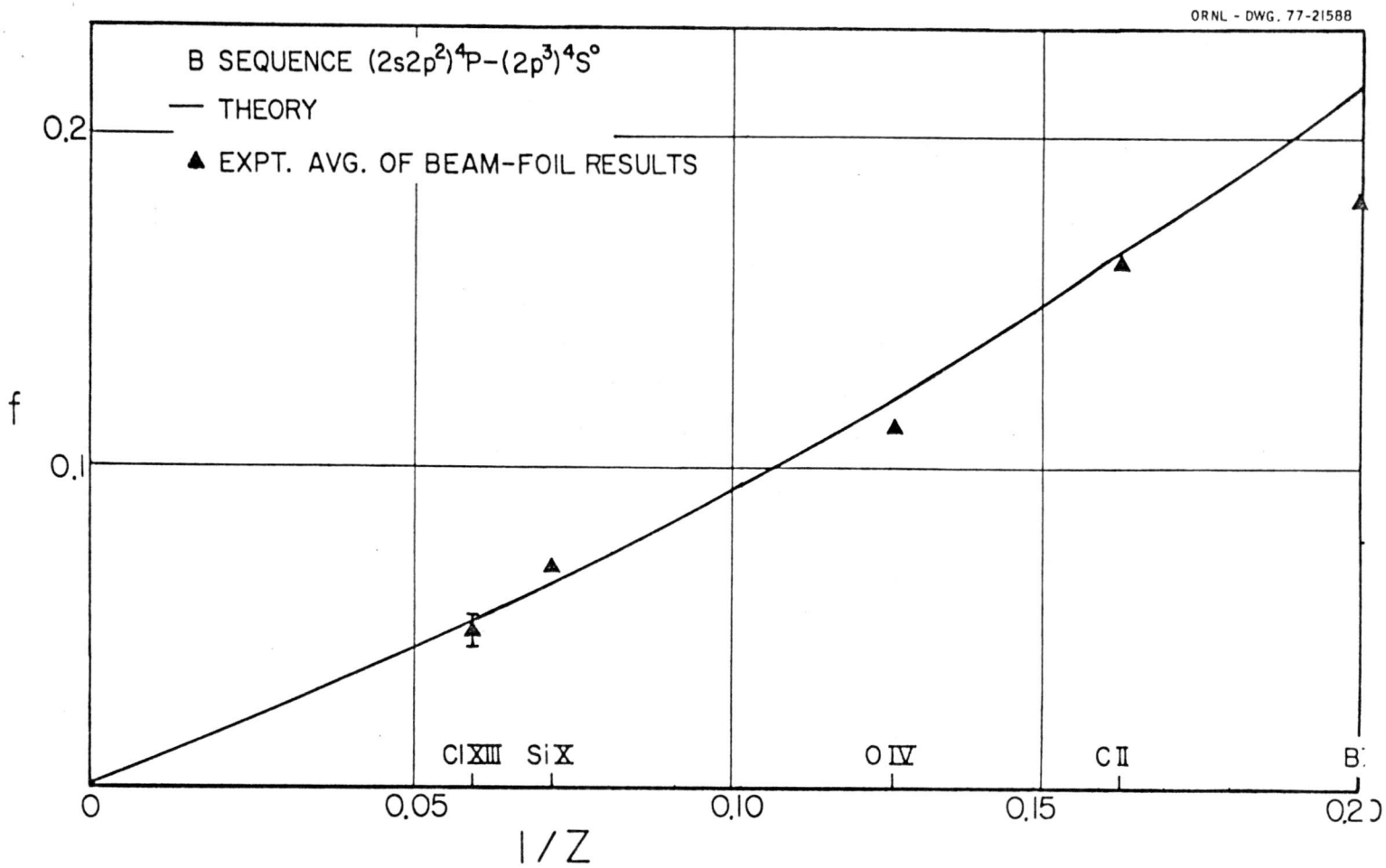


Figure 5.10. Isoelectronic sequence plot showing the multiplet f-value of the $(2s2p^2)^4P - (2p^3)^4S^o$ transition versus inverse nuclear charge.

When looking at the isoelectronic-sequence plot of the f-values of this transition versus Z^{-1} shown in Figure 5.11, it is seen that all of the beam-foil values lie lower than the theoretically-predicted values of Sinanoglu and co-workers that are shown by the solid line. The experimental results of this experiment (and possibly those for other members of the sequence also) can perhaps be attributed to the difficult cascading situation described in Chapter 4. In addition, extrapolation of the theoretical values to obtain the value quoted in Table 5.1 can lead to errors which might explain some of the differences between theory and experiment in this case. The experimental f-value for the $(1s^2 2s^2 2p^2)\,^3P^o$ - $(1s^2 2s 2p^3)\,^3P$ transition listed in Table 5.1 is somewhat lower than theory. It is unlikely that this is due to cascading. The isoelectronic sequence plot for this transition is shown in Figure 5.12. One sees that all of the beam-foil values differ substantially from Sinanoglu's theoretical results even though the general shape of the theoretical curve seems to follow the experimentally measured trends. The experimental value of the present investigation is seen to be in better agreement with theory than is the case for other members of the sequence.

The experimental f-value of the $(1s^2 2s^2 2p^2)\,^3P$ - $(1s^2 2s 2p^3)\,^3D$ transition agrees well with theory as can be seen both in Table 5.1 and Figure 5.13. The solid line in Figure 5.13 represents the calculations of Sinanoglu and the dashed line represents the calculations of Safronova et al. Both theoretical predictions are plotted graphically to illustrate their different range of applicability. For lower Z members of the sequence the difference is quite apparent. The perturbation

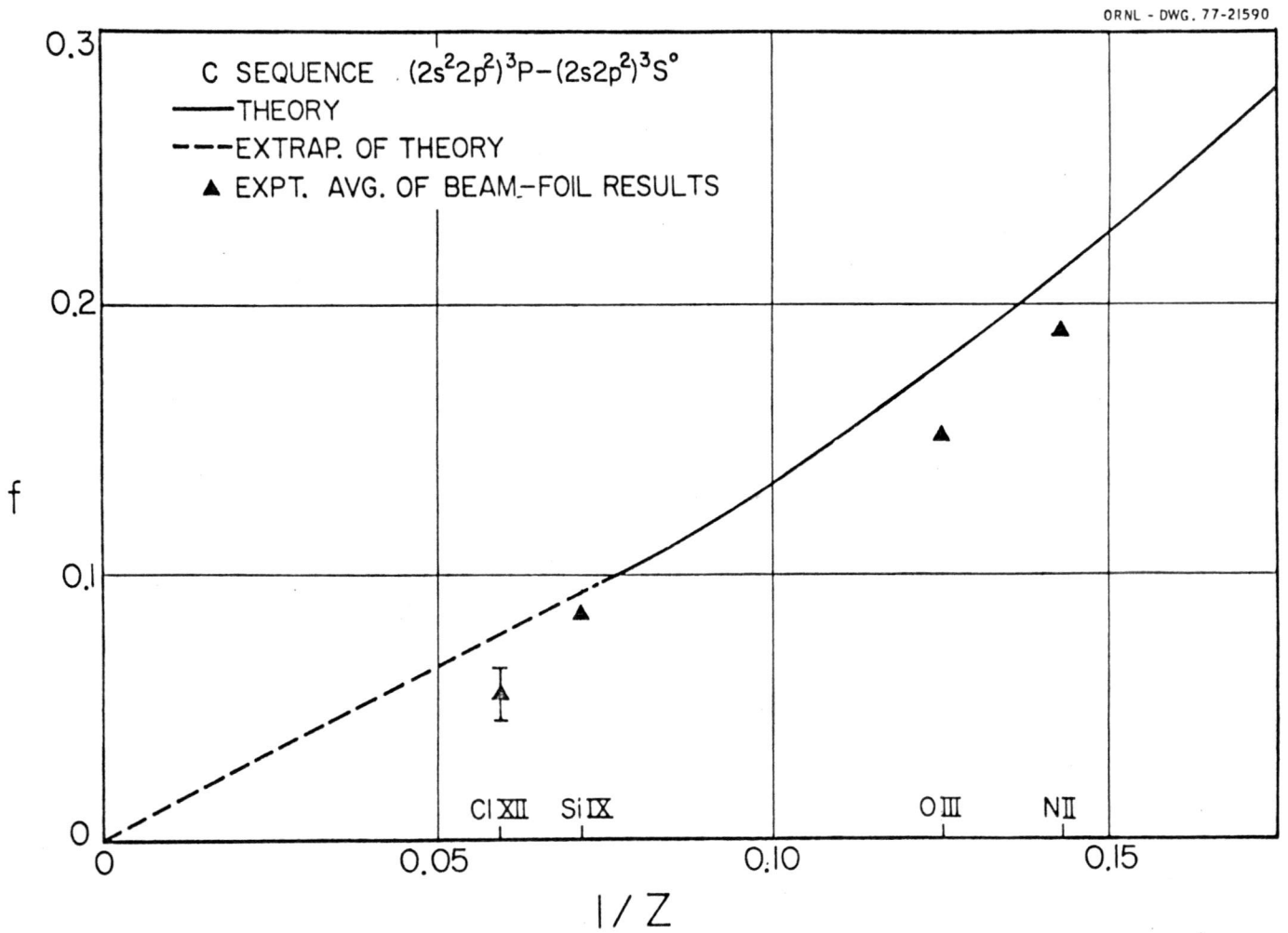


Figure 5.11. Isoelectronic sequence plot showing the multiplet f-value of the $(2s^2 2p^2)^3P - (2s2p^2)^3S^o$ transition versus inverse nuclear charge.

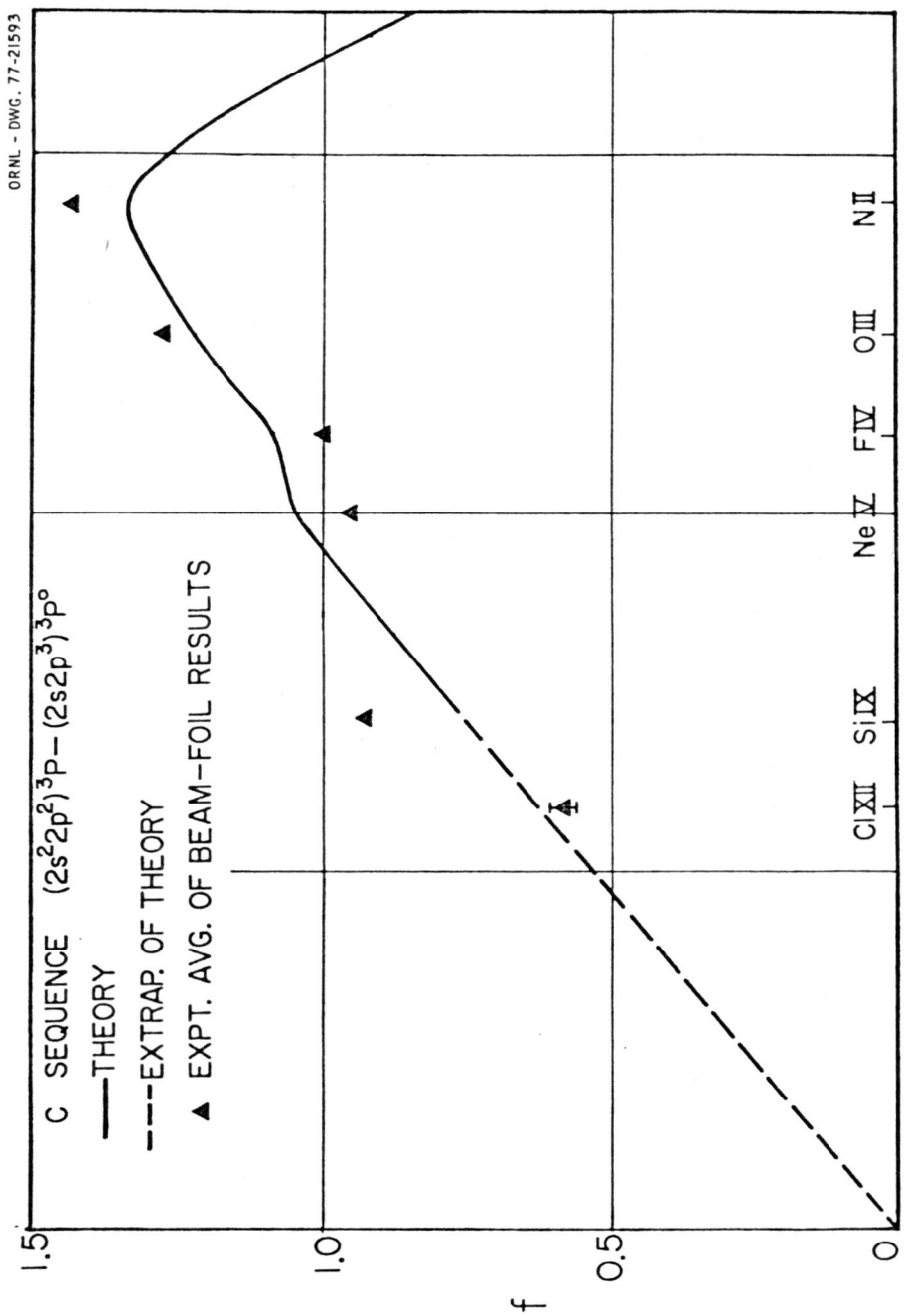


Figure 5.12. Isoelectronic sequence plot showing the multiplet f-value of the $(2s^22p^2)^3P - (2s2p^3)^3P^o$ transition versus inverse nuclear charge.

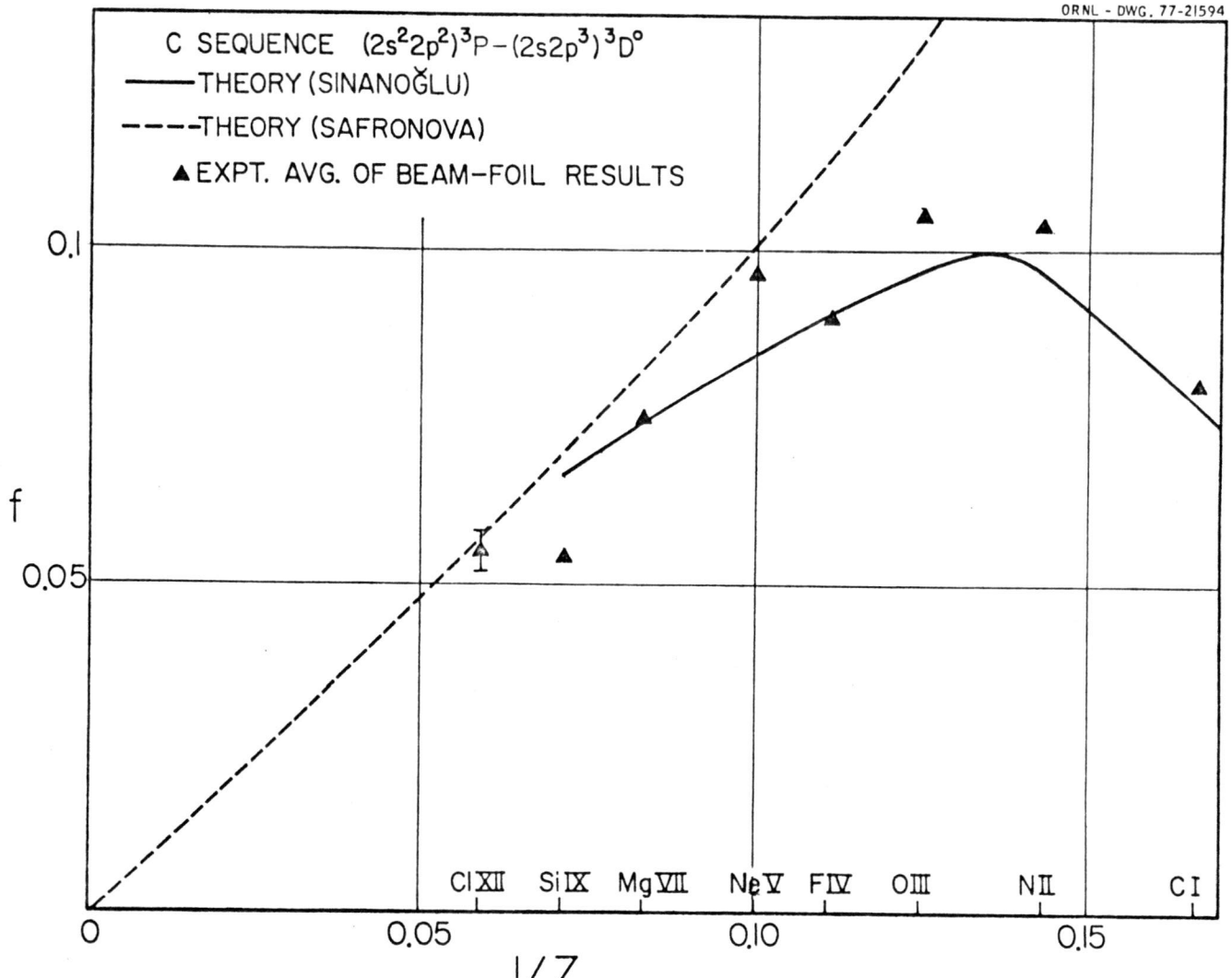


Figure 5.13. Isoelectronic sequence plot showing the multiplet f-value of the $(2s^2 2p^2)^3P - (2s2p^3)^3D^o$ transition versus inverse nuclear charge.

theory approach of Safronova et al. does not adequately account for the electron-correlation effects that are substantial for the low-Z members of the sequence. For the higher Z members of the sequence the electron-repulsion term contributes proportionally less to the total energy of the system and the relatively simple perturbation theory calculations of Safronova et al. approach the predictions of Sinanoglu who incorporates electron-correletion effects throughout the sequence. For a nuclear charge of 17 (that studied in the present work) the two theories essentially coincide. The agreement between experiment and theory for the f-value of the $(1s^2 2s^2 2p^2)\,^1D$ - $(1s^2 2s 2p^3)\,^1D$ transition is good as can be seen in both Table 5.1 and Figure 5.14. The solid line curve of Figure 5.14 represents the calculations of Sinanoglu with the broken line showing the extrapolation of these results to infinite Z.

Cl XI (7-electron)

F-values were determined for two transitions in N-like chlorine, Cl XI. Both of these experimental f-values are in general agreement with theory as is seen in Table 5.1. Figures 5.15 and 5.16 show the isoelectronic-sequence plots of f versus Z^{-1} for the $(1s^2 2s^2 2p^3)\,^2P^o$ - $(1s^2 2p^4)\,^2S$ and $(1s^2 2s^2 2p^3)\,^4S^o$ - $(1s^2 2s 2p^4)\,^4P$ transitions respectively. In both of these figures the solid line represents the calculations of Sinanoglu and the dashed line those of Safronova et al. Again these two theoretical approaches are plotted together for comparative purposes. Experimental data for other members of this isoelectronic sequence is sparse.

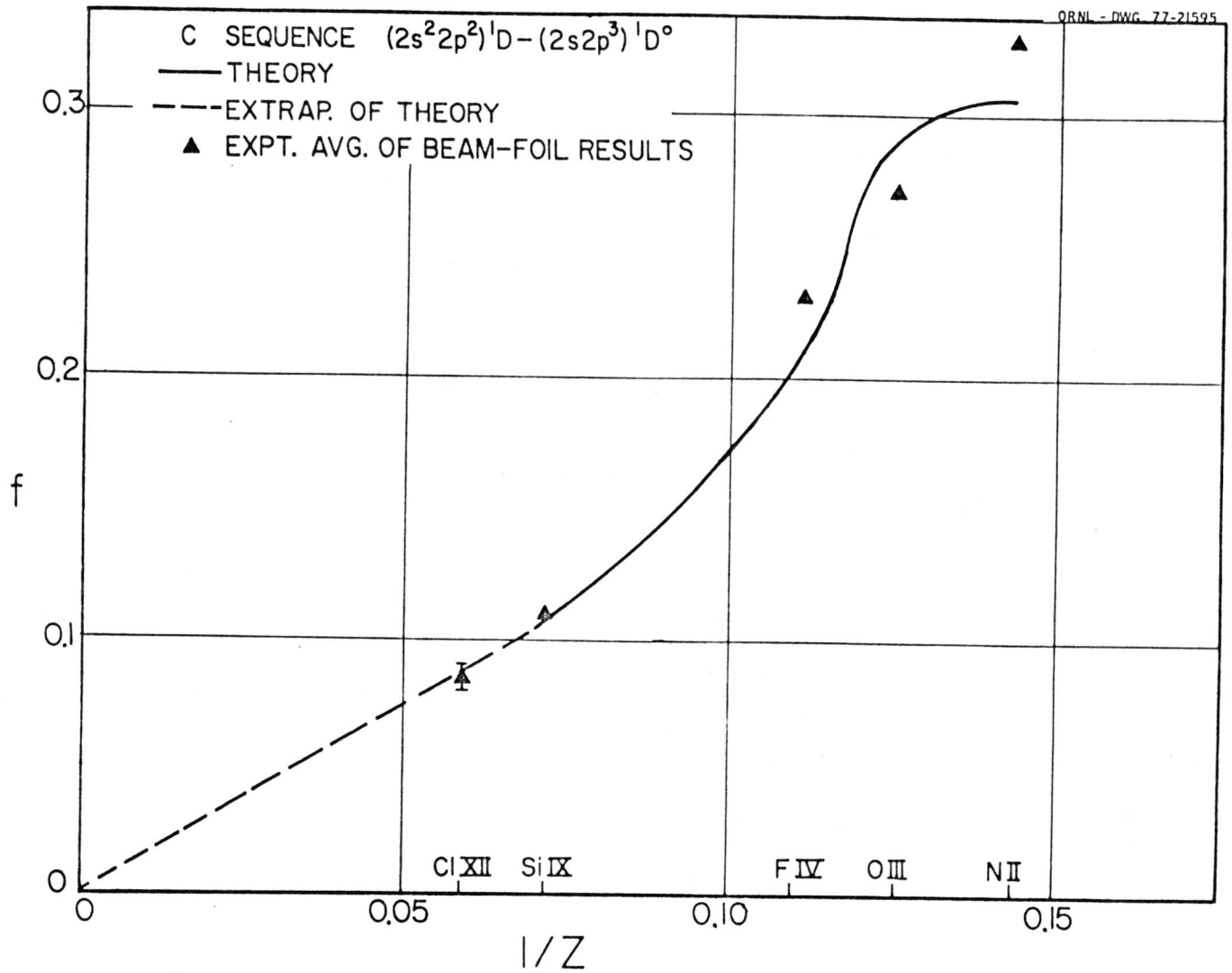


Figure 5.14. Isoelectronic sequence plot showing the multiplet f-value of the $(2s^22p^2)\,^1D - (2s2p^3)\,^1D^\circ$ transition versus inverse nuclear charge.

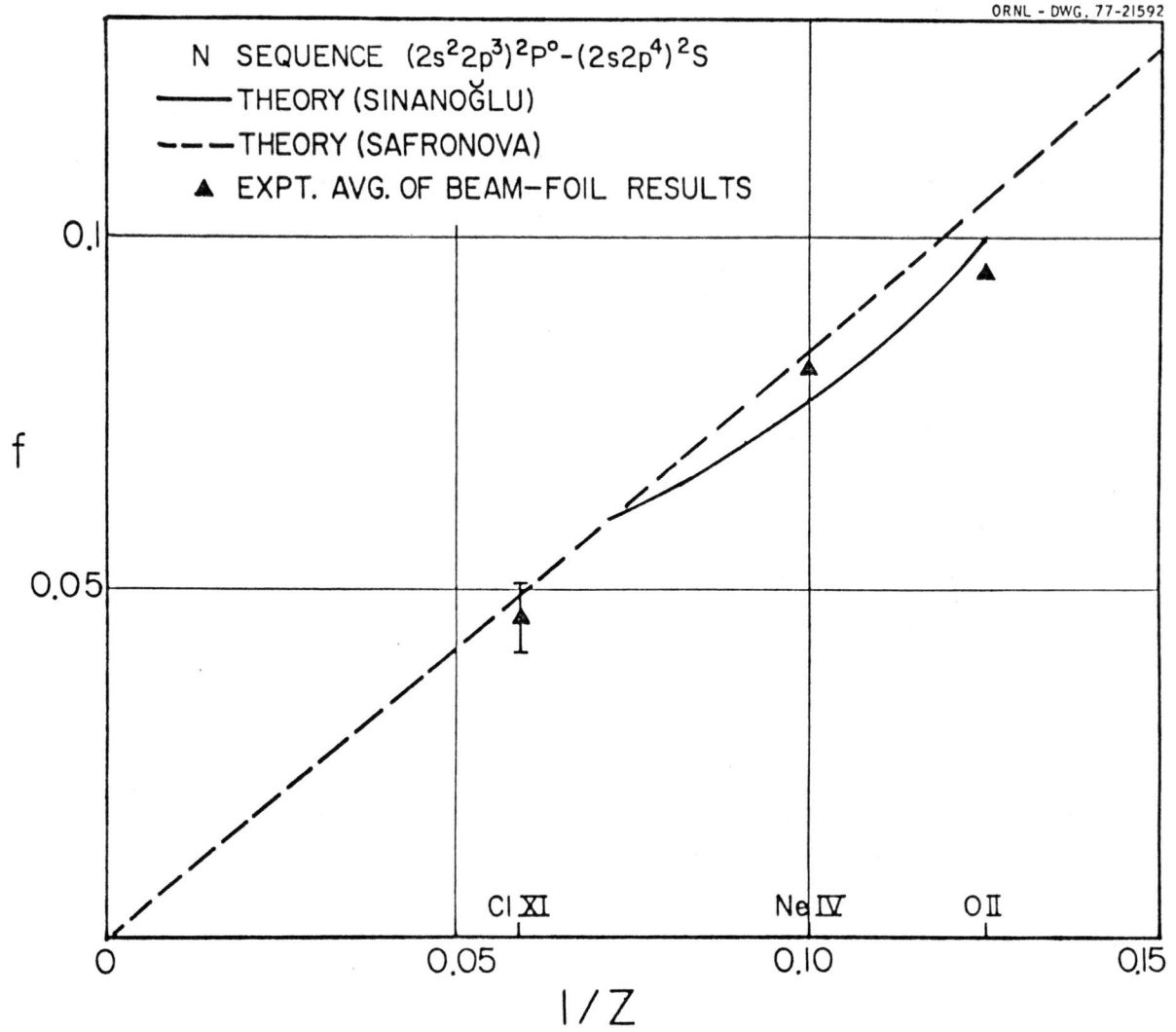


Figure 5.15. Isoelectronic sequence plot showing the multiplet f-value of the $(2s^2 2p^3)^2P^o$ - $(2s2p^4)^2S$ transition versus inverse nuclear charge.

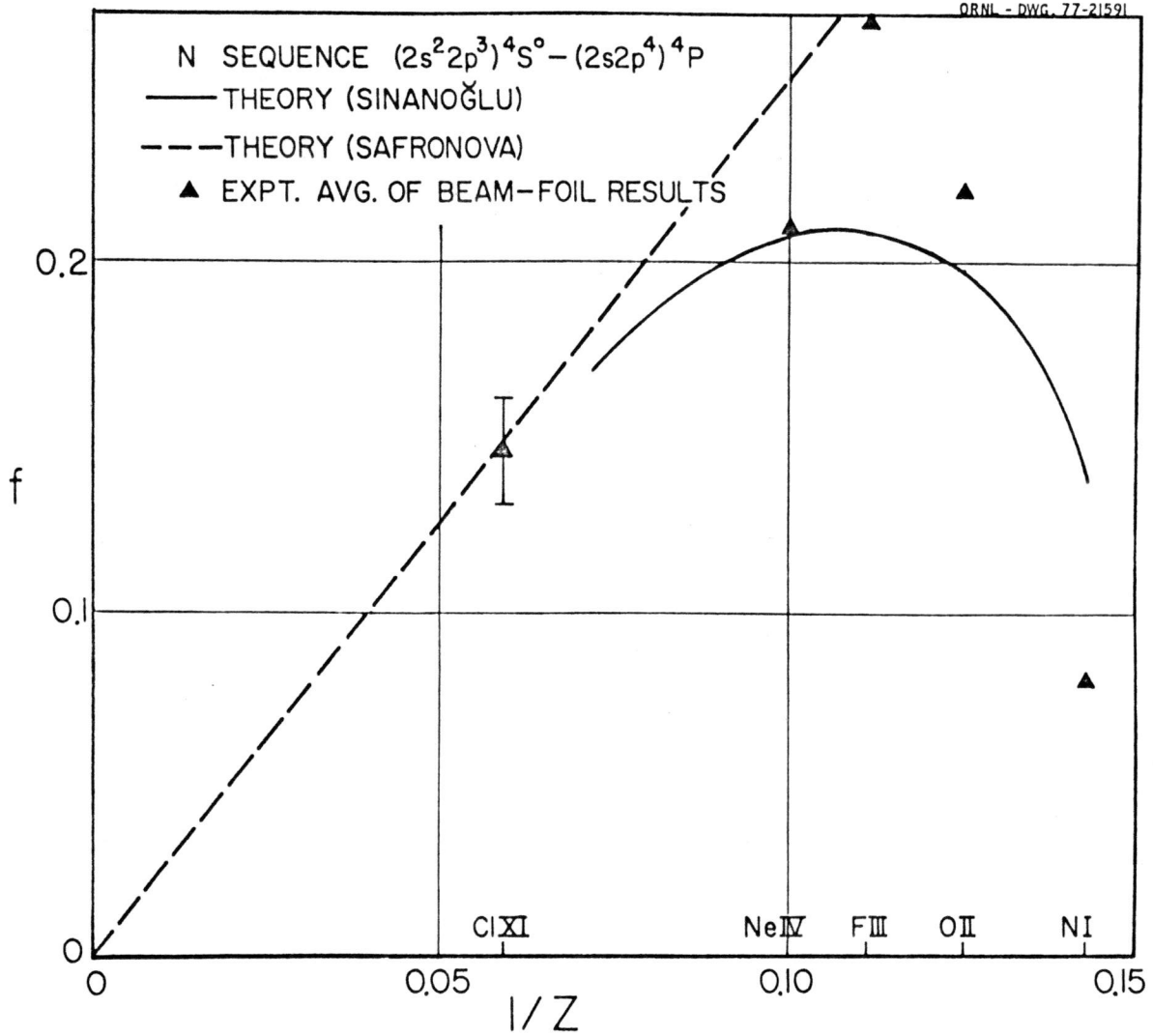


Figure 5.16. Isoelectronic sequence plot showing the multiplet f-value of the $(2s^2 2p^3)^4S^o$ - $(2s2p^4)^4P$ transition versus inverse nuclear charge.

Cl X (8-electron)

Two f-values were determined for transitions in the O-like chlorine ion, Cl X. Table 5.1 shows that experimental values are in reasonable, although not completely satisfactory, agreement with the theoretical predictions. Isoelectronic-sequence plots for the $(1s^2 2s 2p^5)\,^1P^o$ - $(1s^2 2p^6)\,^1S$ and the $(1s^2 2s^2 2p^4)\,^3P$ - $(1s^2 2s 2p^5)\,^3P^o$ transitions are shown in Figures 5.17 and 5.18 respectively. The smooth curve of Figure 5.17 represents the predictions of Safronova et al. There appears to be no other experimental results for these transitions for any other members of the O-sequence. Calculations become considerably more difficult for these relatively complex structures and this may account for some of the difference that exists between theory and the present results.

Cl IX (9-electron)

The f-value for the $(1s^2 2s^2 2p^5)\,^2P^o$ - $(1s^2 2s 2p^6)\,^2S$ transition listed in Table 5.1 is somewhat lower than theory predicts. The isoelectronic-sequence plot of f versus Z^{-1} for this transition is shown in Figure 5.19. The solid line represents the theoretical results of Sinanoglu and the broken line that of Safronova et al. Again there appear to be no other experimental results.

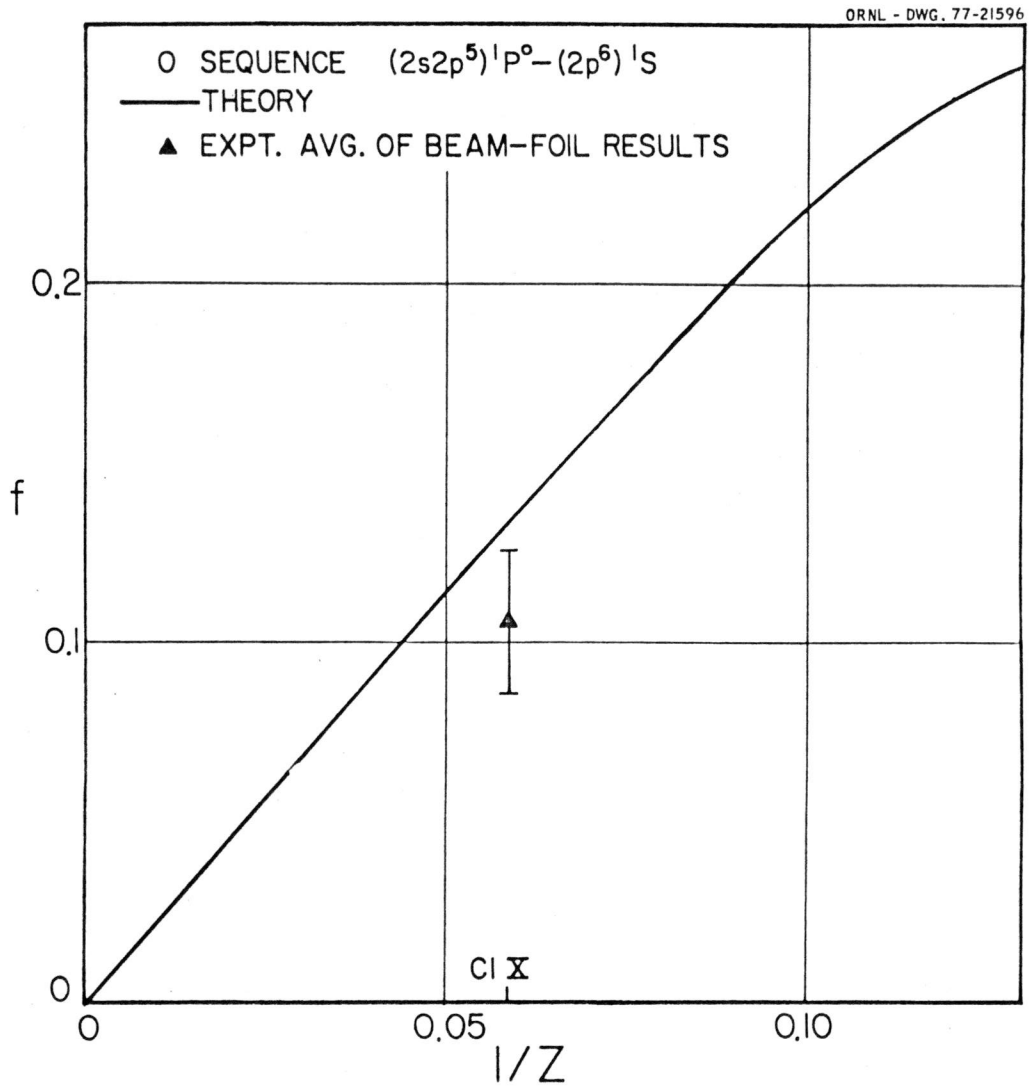


Figure 5.17. Isoelectronic sequence plot showing the multiplet f-value of the $(2s2p^5)^1P^o$ - $(2p^6)^1S$ transition versus inverse nuclear charge.

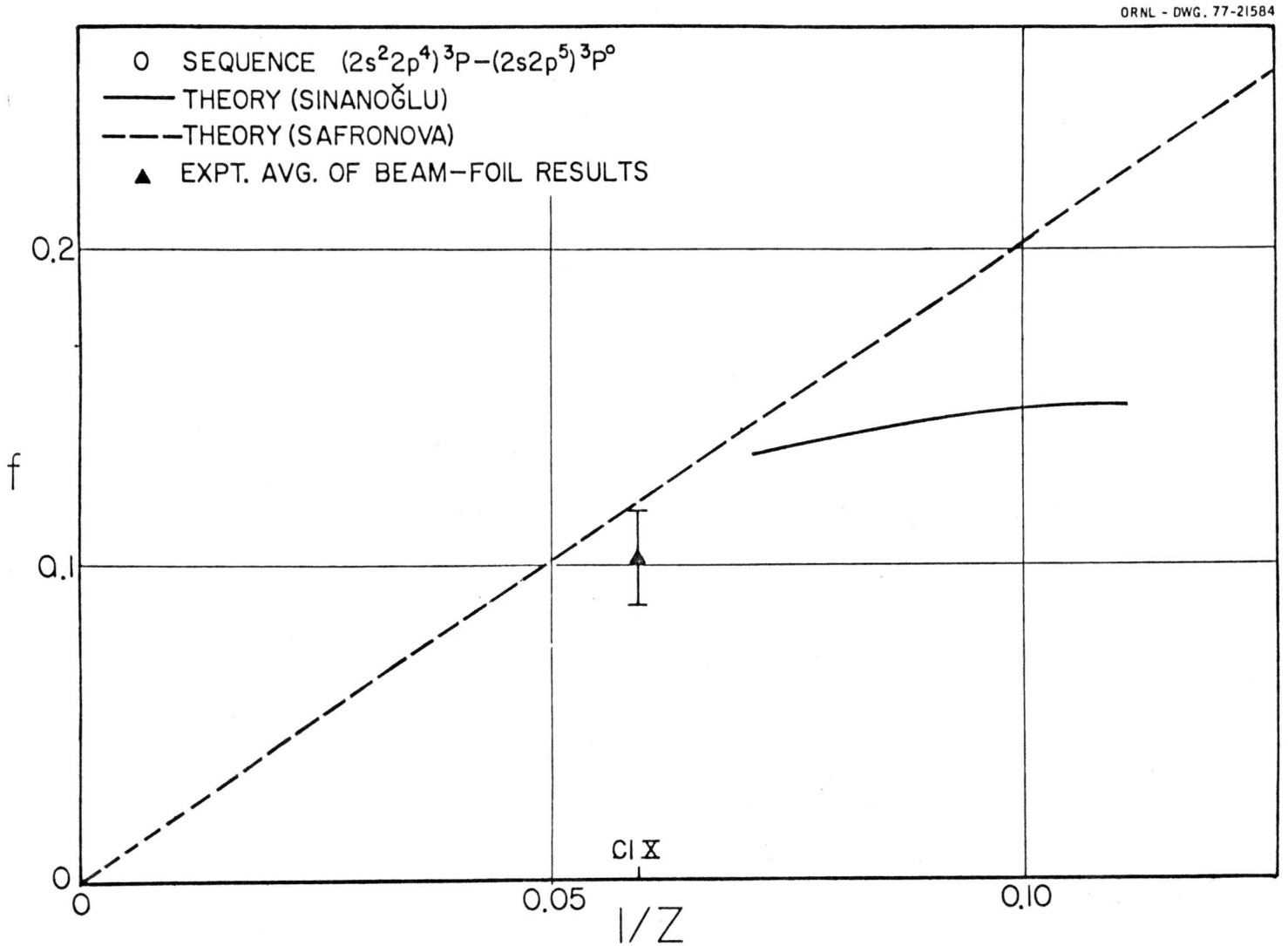


Figure 5.18. Isoelectronic sequence plot showing the multiplet f-value of the $(2s^2 2p^4)\,^3P$ - $(2s2p^5)\,^3P^o$ transition versus inverse nuclear charge.

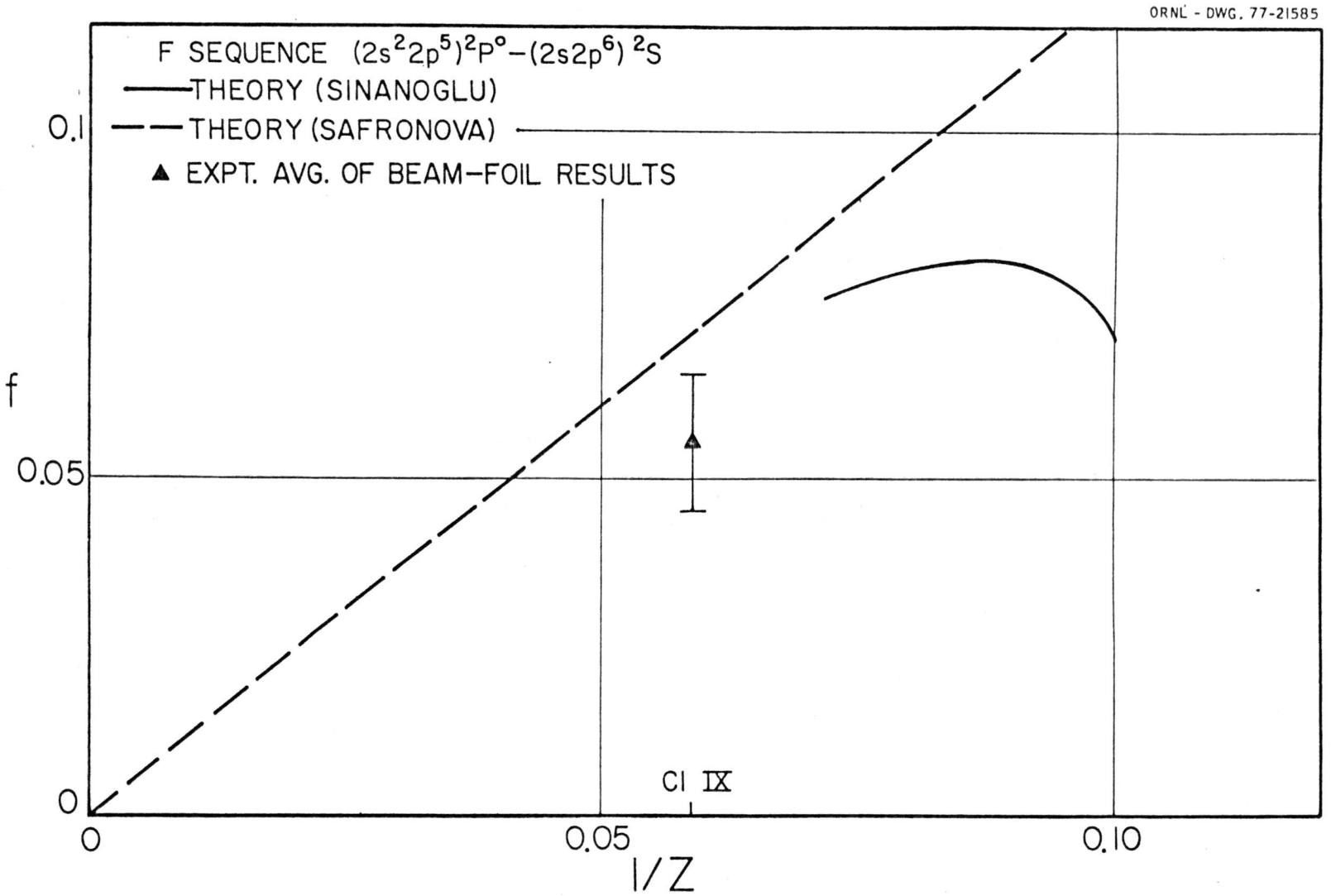


Figure 5.19. Isoelectronic sequence plot showing the multiplet f-value of the $(2s^2 2p^5)^2P^o$ - $(2s2p^6)^2S$ transition versus inverse nuclear charge.

LIST OF REFRENCES

LIST OF REFRENCES

Armstrong, L., W. R. Fielder, and D. L. Lin, Physical Review A14, 1114 (1970).

Bashkin, S., Nuclear Instruments and Methods 28, 88 (1964).

Bashkin, S., and A. B. Meinel, Astrophysical Journal 139, 413 (1964).

Bashkin, S., L. Heroux, and J. Shaw, Physics Letters 13, 229 (1964).

Donnally, B., W. W. Smith, D. J. Pegg, M. Brown, and I. A. Sellin, Physical Review A4, 122 (1971).

Fawcett, B. C., Atomic Data and Nuclear Data Tables 16, 135 (1975).

Irwin, D., and A. Livingston, Computer Physics Communication I, 95 (1974).

Kay, L., Physics Letters 5, 36 (1963).

Kelly, R. L., and L. J. Palumbo, Atomic and Ionic Emission Lines Below 2000Å, NRL Report 7599, Naval Research Laboratory, Washington, D.C.

Kim, Y. K., and J. P. Desclaux, Physical Review Letters 36, 139 (1976).

Larson, D., private communication.

Nagel, D. J., "Beam-Foil Spectroscopy" (I. A. Sellin and D. J. Pegg, eds.) Vol II, p 961. Plenum Press, New York, 1976.

Northcliffe, L. C., and R. F. Schilling: Nuclear Data Tables AI, No. 3-4, Academic Press, New York, 1970.

Safronova, U. I., A. N. Ivanova, and V. N. Kharitonova, Theoretical and Experimental Chemistry 5, 325 (1965).

Shamey, L. J., Journal of the Optical Society of America 61, 942 (1970).

Sinanoglu, O., and W. Luken, Journal of Chemical Physics 64, 4197 (1976)

Sinanoglu, O., Nuclear Instruments and Methods 110, 193 (1973).

Veje, E., Physical Review A14, 2077 (1976).

Wein, W., Annals der Physik 60, 597 (1919).

APPENDIX

APPENDIX

The line-strength factor for an electric-dipole transition between an initial state $|\phi_i\rangle$ and a final state $|\phi_j\rangle$ is defined as,

$$S = |\langle \Phi_j | \vec{D} | \Phi_i \rangle|^2 \quad , \tag{A-1}$$

where $\vec{D}$ represents the electric-dipole moment for the transition. The absorption oscillator strength (f-value) is related to the line strength in the following manner:

$$f = (2/3)\, \Delta E\, g^{-1}\, S \quad , \tag{A-2}$$

where ΔE is the energy separation (in atomic units) of the upper and lower levels of the transition and g is the statistical weight of the lower level.

The non-relativistic time-independent Schrödinger equation in atomic units can be written as;

$$\left[-\sum_i \left((1/2)\nabla_i^2(r_i) + Z r_i^{-1} \right) + \sum_{i>j} r_{ij}^{-1} \right] |\Phi = E\,|\Phi\rangle \, . \tag{A-3}$$

Dividing the equation by Z^2 (Z is the nuclear charge on an ion) and scaling all distance, r, by Z and all energies by Z^{-2} yields the following contribution in terms of the new distance variable, $\rho = Zr$:

$$\begin{aligned} \nabla_i^2(r) &= Z^2 \left[\tilde{\nabla}_i(\rho) \right] \\ Z\, r_i^{-1} &= Z^2\, (\rho_i^{-1}) \\ r_{ij}^{-1} &= Z^2 (Z^{-1} \rho_{ij}^{-1}) \quad . \end{aligned} \tag{A-4}$$

Substituting the relations of (A-4) into (A-3) yields,

$$-\sum_i \left[(1/2)\tilde{\nabla}_i^2(\rho_i) + \rho_i^{-1} \right] + Z^{-1} \sum_{i>j} \rho_{ij}^{-1} \, |\Phi\rangle = |\Phi\rangle, \tag{A-5}$$

with $\rho = Z\, r$ and $\epsilon = Z^{-2} E$.

This equation can be written as,

$$(\tilde{H}_o + Z^{-1}\tilde{H}_1)\,|\Phi\rangle = \epsilon\,|\Phi\rangle \quad , \tag{A-6}$$

where H_o is the zeroth-order Hamiltonean expressed in terms of ρ coordinates and H_1 represents the residual interelectronic repulsion perturbation in terms of the same coordinates. In this form Z^{-1}, the inverse nuclear charge, appears as a natural perturbation expansion parameter for the expansion of the eigenfunctions and eigenvalues, i.e.,

$$\begin{aligned} |\Phi\rangle &= |\Phi_o\rangle + Z^{-1}|\Phi_1\rangle + Z^{-2}|\Phi_2\rangle + \cdots \\ \epsilon &= \epsilon_o + Z^{-1}\epsilon_1 + \epsilon_2 + \cdots \end{aligned} \tag{A-7}$$

The energy expression can be rewritten since $E = Z^2\epsilon$ as,

$$E = Z^2\epsilon_o + Z^{-1}\epsilon_1 + \epsilon_2 + \cdots \tag{A-8}$$

where $\epsilon_o = (1/2)\sum_i \frac{1}{n_i^2}$ represents the independent-particle (hydrogenic) value in atomic units.

If the eigenfunction expansion (A-7) is substituted into equation (A-1) and the terms are grouped according to the power of Z, one gets the line strength as,

$$\begin{aligned} S = Z^{-2}\Big[&\langle\Phi_{oj}|\vec{D}(\rho)|\Phi_{oi}\rangle + Z^{-1}\left|\langle\Phi_{oj}|\vec{D}(\rho)|\Phi_{1i}\rangle + \langle\Phi_{1j}|\vec{D}(\rho)|\Phi_{oi}\rangle\right| \\ &+ Z^{-2}\left|\langle\Phi_{oj}|\vec{D}(\rho)|\Phi_{2i}\rangle + \langle\Phi_{1j}|\vec{D}(\rho)|\Phi_{1i}\rangle + \langle\Phi_{2j}|\vec{D}(\rho)|\Phi_{oi}\rangle\right| \\ &+ \cdots\Big]^2 \end{aligned} \tag{A-9}$$

Squaring the terms in the brackets and neglecting terms with powers of Z^{-2} or greater yields,

$$S = Z^{-2}\left|\left\langle \Phi_{oj}\left|\vec{D}(\rho)\right|\Phi_{oi}\right\rangle\right|^2 + 2Z^{-1}\left[\left\langle\Phi_{oj}\left|\vec{D}(\rho)\right|\Phi_{oi}\right\rangle\left\langle\Phi_{oj}\left|\vec{D}(\rho)\right|\Phi_{1j}\right\rangle + \left\langle\Phi_{1j}\left|\vec{D}(\rho)\right|\Phi_{oi}\right\rangle\right] + \cdots \qquad \text{(A-10)}$$

Defining,

$$S_o = \left|\left\langle \Phi_{oj}\left|\vec{D}(\rho)\right|\Phi_{oi}\right\rangle\right|^2 \qquad \text{and}$$

$$S_1 = 2\left\langle\Phi_{oj}\left|\vec{D}(\rho)\right|\Phi_{1i}\right\rangle\left[\left\langle\Phi_{oj}\left|\vec{D}(\rho)\right|\Phi_{1i}\right\rangle + \left\langle\Phi_{ij}\left|\vec{D}(\rho)\right|\Phi_{oi}\right\rangle\right]$$

one obtains,

$$S = Z^{-2}S_o + Z^{-3}S_1 + \cdots \qquad \text{(A-11)}$$

The transition energy, ΔE can be written, using the expansion of (A-7), as,

$$\Delta E = E_i - E_j = Z^2(\epsilon_{oi} - \epsilon_{oj}) + Z(\epsilon_{1i} - \epsilon_{1j}) \qquad \text{(A-12)}$$

Using (A-12) and (A-11) in (A-2) gives:

$$f = (2/3)g^{-1}\left[(\epsilon_{oi} - \epsilon_{oj})S_o + Z^{-1}(\epsilon_{1i} - \epsilon_{1j})S_1 + (\epsilon_{1i} - \epsilon_{1j})S_o\right] = f_o + Z^{-1}f_1 + \cdots$$

Thus in the non-relativistic approximation the f-value for an electric-dipole transition approaches the hydrogenic value, f_o, linearly as $Z \to \infty$. For $\Delta n=0$ transitions, $f_o=0$ due to the degeneracy of levels with the same n in the non-relativistic approximation. Relativistic corrections (e.g. terms of order $Z^4\alpha^2$) to the transition energy (and to a lesser extent the line strength) causes the f value to increase.

VITA

Johnny Page Forester was born in Morristown, Tennessee on March 17, 1945. He attended elementary schools in that city and was graduated from Morristown High School in June 1963. He then attended the University of Tennessee and in December 1967 received a Bachelor of Science degree in Engineering Physics.

Upon graduation he entered the United States Navy where he was a basic jet pilot instructor. When discharged he entered the Graduate School of the University of Tennessee, Knoxville, and received the Master of Science degree with a major in Physics in August 1972. Remaining enrolled in the graduate school he began working for the Doctor of Philosophy degree with a major in Physics. This degree was awarded in March 1978.

The author is a member of Sigma Pi Sigma and the American Physical Society. He presently holds the position of Assistant Professor of Physics at the University of Tennessee at Chattanooga.

He is married to the former Anita Jean Young also of Morristown. They have two children, Johnny Page age 7 and Matthew Arron age 5.